JARST

RMUTT

The Journal of Applied Research on Science and Technology (JARST) aims to disseminate and share knowledge and ideas in the form of high-quality articles to academia, professionals, industrialists, and an important forum for exchanging knowledge between researchers, academics, faculty members and students both national and international, which will bring benefits in building academic cooperation and network that will lead to sustainable use of research. The articles that will be published in this journal must not be ever presented and published or in the evaluation processes in any other journals. Any piracy occurred will be only under the responsibility of the authors. The journal will not be responsible for such consequences.

Aims and Scope

The scope of the journal includes the following areas of research: General Engineering, General Materials Science, General Agricultural and Biological Sciences, General Computer Science, and General Mathematics with particular emphasis on issues that deepen in the basic and applied research. The JARST includes full length original, novel research articles and review articles. Accepted articles are immediately available online and are freely accessible without any restrictions or any other obligations to researchers and scholarly people globally.

Review Process

1. Evaluation by the Editor-in-Chief

The Editor-in-Chief will see whether the topic and theme of the article are appropriate and congruent with the stipulated objectives and format of the Journal. Plagiarism and benefits relating to theory and business contribution will also be investigated. The submitted paper may be returned to the author for preliminary revising or, if the aforesaid criteria are not met, rejected.

2. Evaluation by Review

All submitted manuscripts must be reviewed by at least two expert reviewers in the related fields. Reviewers will evaluate the quality of submitted article for publication via the double-blinded review system.

3. Evaluates the Reviews

The Editor-in-Chief make decision for article publication based on the external readers' evaluation. The said decision is either accepting the article for publication, rejecting it, or resending it back to the author for further elaborating revision.

Period of Issued Journal

The Journal of Applied Research on Science and Technology (JARST) will be 3 issues/year, as follows:

1st issue: January - April
2nd issue: May - August
3rd issue: September - December

Advisory Board

Editorial Note

The Journal of Applied Research on Science and Technology (JARST) is an academic journal prepared by Institute of Research and Development, Rajamangala University of Technology Thanyaburi (RMUTT). The JARST aims to disseminate and share knowledge and ideas in the form of high-quality articles related General Engineering, General Materials Science, General Agricultural and Biological Sciences, General Computer Science, and General Mathematics to researchers, academics, faculty members and students both national and international.

This journal published eight research articles. Each of the research articles presented interesting concepts such as WO_3/Bi_2WO_6 photoanode enhancement for photoelectrocatalytic water oxidation; scan rate effect optimization in the cyclic voltammetry deposition method, Efficiency of wastewater treatment from environmental laboratory of science and technology, RMUTP using ozonation, Optimizing pick-place operations: Leveraging k-means for visual object localization and decision-making in collaborative robots, Improvement of heat-sealing strength of chitosan-based composite films and product costs analysis in the production process, Preparation of poly(methyl methacrylate)-zinc oxide hybrid nanoparticles via miniemulsion polymerization, The development of association rules for student performance analysis using FP-Growth algorithm as a guideline for multidisciplinary learning, Development of Samed mushroom (Boletus griseipurpureus Corner) crackers and quality study during storage, and Development of an innovative wireless power transmission model for marine applications. Therefore, this journal is a channel disseminating the knowledge areas of physical sciences and life sciences which related persons could apply it for further benefits.

Lastly, the editorial team would like to considerably thank you for supporting and pushing forward this journal to occur and well accomplish. We are hopeful of your good cooperation and continuing support in the future.

Editorial Team

Contents

WO₃/Bi₂WO₆ photoanode enhancement for photoelectrocatalytic water oxidation; scan rate effect optimization in the cyclic voltammetry deposition method

Titsucha Uttayanil[1] and Chatchai Ponchio[1,2]*

[1]Department of Chemistry, Faculty of Science and Technology, Rajamangala University of Technology Thanyaburi, Pathum Thani 12120, THAILAND

[2]Advanced Photochemical and Electrochemical Materials Research Unit (APEM) Research Unit, Faculty of Science and Technology, Rajamangala University of Technology Thanyaburi, Pathum Thani 12110, THAILAND

*Corresponding author: chatchai@rmutt.ac.th

ABSTRACT

The photoelectrocatalytic approach is a very efficient technology for eliminating microorganisms and organic contaminants. The development of photoanode is widely recognized as a crucial approach to enhancing the efficiency of photoelectrocatalytic cells. The key goal of this methodology is to enhance the efficacy of photoelectrocatalytic oxidation by optimizing composited photoanode fabrication. This research development focuses mainly on fabricating composite WO₃/Bi₂WO₆ semiconductor thin films with high water oxidation efficiency and favorable photoelectrocatalytic *E. coli* degradation applications. Cyclic voltammetry was utilized to create WO₃/Bi₂WO₆ thin coatings on conducting glass while optimizing the photoelectrocatalytic activity via the scan rate parameter. The characteristics of the developed electrode, including charge transfer resistance, optical properties, morphology, crystal structure, chemical composition, and oxidation numbers, were investigated to improve photoelectrocatalytic activity. It was observed that the scanning rate significantly influenced the characteristics of the WO₃/Bi₂WO₆ electrode and the photoelectrocatalytic activity on water oxidation. It was discovered that the WO₃/Bi₂WO₆ electrode prepared with a scan rate of 25 mV/s exhibited the greatest photoelectrocatalytic water oxidation as well as distinguishing characteristics from other conditions. The decision to utilize decreased scanning rates has been determined to optimize the reaction kinetics and improve the film-forming properties of WO₃/Bi₂WO₆. Significantly, the developed electrode can also be used to eliminate 87.5% of *E.coli* in 15 minutes via a photoelectrocatalytic catalytic mechanism. The photoanode composed of WO₃/Bi₂WO₆ has promising capabilities in removing microorganisms and organic pollutants, making it a viable candidate for future advancements in wastewater management applications.

Keywords: Photoelectrocatalytic, Cyclic voltammetry techniques, WO₃/Bi₂WO₆, *E.coli* degradation

INTRODUCTION

The issue of microbial contamination and toxic organic compounds is an additional aspect that impacts the quality of life and the broader ecosystem. Therefore, it is essential to create or offer efficient strategies to handle these issues [1]. One of the most effective advanced oxidation technologies usually developed for removing such pollutants is photoelectrocatalytic (PEC) technology [2-6]. The strategy or guiding principle for the development of such techniques is the selection of suitable semiconductors and the creation of a substrate-based semiconductor film fabrication process. WO₃ and Bi₂WO₆ are two attractive semiconductors extensively used as photoanodes for organic elimination [7-10]. Because of its adequate energy value, it can absorb visible light and has a high positive valence potential appropriate for oxidation processes in aqueous solutions [11]. Preparing the semiconductor

film on the substrate is regarded as a significant factor influencing the performance and durability of PEC cells in practical applications. The sol-gel method is a relatively simple and cost-effective technology for making WO₃ and Bi₂WO₆ films since it allows for perfect control over film thickness and composition and can be easily scaled up for large-scale production [12, 13]. However, to achieve the desired crystalline structure, the sol-gel approach may require high-temperature annealing, and film quality might be affected by processing conditions. The hydrothermal approach enables the formation of WO₃ and Bi₂WO₆ films at lower temperatures, increasing crystallinity and photocatalytic activity [8, 14]. However, a longer processing time and careful control of reaction parameters may be required to produce the necessary film qualities. Electrodeposition is a viable option for preparing WO₃ and Bi₂WO₆ films because it is a basic, cost-effective

technique that does not require expensive equipment or high temperatures. This investigation aims to develop an electrochemical technique for preparing composite WO_3 and Bi_2WO_6 films on conducting glass substrates using cyclic voltammetry (CV) [15, 16]. Cyclic voltammetry is a versatile and powerful technology for fabricating and characterizing semiconductor films, providing precise control, important insights, and scalability for a wide range of optoelectronics, photoelectrochemistry, and beyond applications. We developed the CV method for WO_3 and Bi_2WO_6 film formation by deciding the optimal PEC water oxidation properties, including precursor concentration, applied potential range, and scanning rate. We discovered that the scanning rate considerably impacted the WO_3/Bi_2WO_6 electrode characteristics and the PEC properties for water oxidation. Importantly, our system can also eliminate *E. coli* and is suitable for further development in treating effluent contaminated with microorganisms and toxic organic compounds.

MATERIALS AND METHODS

Chemical and materials

Throughout the experiment, deionized water was utilized to produce all solutions and compounds of the analytical grade. Diethylenetriamine pentaacetic acid; DTPA (Sigma Aldrich), Ammonium hydroxide; NH_4OH (J.T.Baker), Bismuth(III)oxide; Bi_2O_3 (Sigma Aldrich), Ammonium metatungstate hydrate; $(NH_4)_6H_2W_{12}O_{40}·H_2O$ (Sigma Aldrich), Nitric acid; HNO_3 (Univar), Hydrogen peroxide; H_2O_2 (Chem-supply), Ethanol; C_2H_5OH (Rcl Labscan), Sodium chorine; NaCl (Kemaus), Methylene Blue; $C_{16}H_{18}ClN_3S$ (KEMAUS) Sodium hydroxide; NaOH (Univar) were used as chemical precursor materials.

WO_3/Bi_2WO_6 precursor solution preparation

To prepare the WO_3/Bi_2WO_6 precursor solution, 0.83 g of diethylenetriamine pentaacetic acid (DTPA) was dissolved in 2.5 ml of 30% ammonia solution (NH_4OH), and 50 ml of distilled water was then added. The solution was stirred regularly at 80 °C with a mixture of 0.4 g of bismuth(III)oxide (Bi_2O_3) and 0.15 g of ammonium metatungstate hydrate (($NH_4)_6H_2W_{12}O_{40}.H_2O$). Hydrogen peroxide (77 µl) and nitric acid (1,190 µl) were added to the solution while it was stirred at 80 °C for 15 minutes.

Preparation of WO_3/Bi_2WO_6 electrode

The fluorine-doped tin oxide (FTO) electrode substrate was cleansed using sonication for 10 minutes with detergent, 3 M sodium hydroxide (NaOH), ethanol, and distilled water, respectively. The cleaned FTO was dried and connected with copper wire to serve as a working electrode for the subsequent WO_3/Bi_2WO_6 electrode preparation. Figure 1 displays a three-electrode system configuration for fabricating WO_3/Bi_2WO_6

films using cyclic voltammetry. We use an FTO working electrode and an Ag/AgCl reference electrode to apply a potential ranging from -0.6 V to 0.8 V. For monitoring the current of the CV electrodeposition procedure, and Pt was utilized as a counter electrode. This study emphasized the effect of scan rate in the range of 10-125 mV/s for 30 cycles while keeping the solution temperature at 80 °C. The developed WO_3/Bi_2WO_6 electrode was then sintered for 1 hour at 450 °C. Copper wire was utilized to connect the prepared electrode and epoxy glue was employed to control the working area of the photoanode. The water oxidation photocurrent was used to determine the optimum conditions and performance of the WO_3/Bi_2WO_6 photoanode.
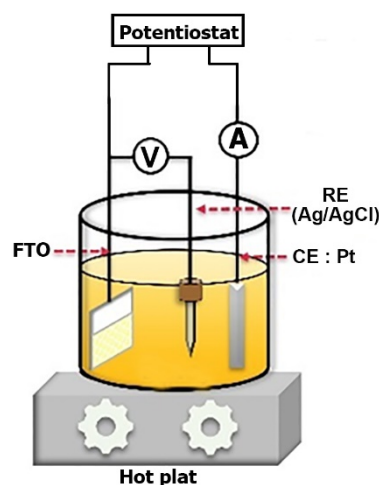
Figure 1 experimental set up for WO_3/Bi_2WO_6 photoanode fabrication using an CV electrodeposition technique.

Characterization and photoelectrocatalytic activity study

The PEC activity for water oxidation was determined using a voltammetry analyzer (Princeton Applied Research, Inc., VersaSTAT 3) in a 0.5 M NaCl electrolyte solution at an applied potential of 1.0 V vs. Ag/AgCl under visible light illumination. Electrochemical impedance spectroscopy (EIS) frequencies ranging from 100 kHz to 0.1 Hz were used to investigate the charge transfer resistance and capacitance at the interfacial electrode/electrolyte. The UV/Vis spectrophotometer (Shimadzu, UV-1601) was used to study the thin WO_3/Bi_2WO_6 film's optical characteristics. Scanning Electron Microscope (SEM, JEOL, JSM 6510) was employed to observe the morphology of the surfaces of thin films. X-ray Diffraction Analysis (XRD, Rigaku, RINT 200TH) was used to investigate the crystal structure. The Energy Dispersive X-ray System (EDX, OXFORD) and X-ray photoelectron spectroscopy (XPS, JEOL, JPS-9010TR) were utilized to confirm the chemical composition and oxidation state of the element at the electrode surface. The effectiveness of PEC *E. coli* degradation was investigated using a two-electrode

system composed of a WO$_3$/Bi$_2$WO$_6$ photoanode and a stainless-steel cathode electrode.

RESULTS AND DISCUSSIONS

WO$_3$/Bi$_2$WO$_6$ photoanode characterization

Figure 2 illustrates the cyclic voltammogram produced by the reduction reaction of WO$_3$/Bi$_2$WO$_6$ adhesion at the FTO substrate during the scan of a negative potential between 0.8 and -0.6 V. The reduction peak current in figure 2 increases with slower scan rates from 125 to 25 mV/s at approximately -0.2 V potential. When the scan rate was decreased to 10 mv/s, the reduction potential position was altered to -0.3 V. The findings indicate that the response mechanism exhibits variations while adjusting for extremely low scan rates. While oxidation currents would be produced in the region of 0.1 to 0.6 V when the scan rate was positively controlled between -0.6 and 0.8 V, shifting as the scan rate slowed down. This phenomenon may arise due to the release of certain precursor or interfering molecules, resulting in increased purity of the electrodes. This is a beneficial aspect of the cyclic voltammetry film preparation procedure.
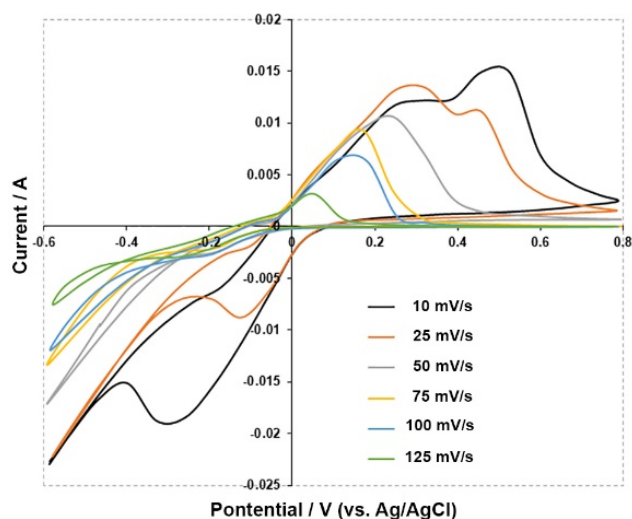
Figure 2 Effects of various scan rates on cyclic voltammograms during WO$_3$/Bi$_2$WO$_6$ deposition using the CV technique.

Figure 3 demonstrates the effect of the scan rate in the CV technique used to prepare WO$_3$/Bi$_2$WO$_6$ electrodes. We discovered that decreasing the scan rate from 125 to 25 mV/s increased the water oxidation photocurrent values of WO$_3$/Bi$_2$WO$_6$ photoanode. This finding elucidates that a decrease in scanning rate allows for increased migration time of the precursor in the solution towards the electrode surface, facilitating a more organized arrangement of the WO$_3$/Bi$_2$WO$_6$ film. Consequently, the resultant film exhibits enhanced efficiency. We discovered that the PEC WO$_3$/Bi$_2$WO$_6$ electrodes were the most effective for oxidizing water

at a scan rate of 25 mV/s. When the scan rate was reduced to 10 mV/s, it was seen that the electrode efficiency decreased dramatically. This decrease can be attributed to the scanning rate being too slow, leading to incomplete adhesion of the semiconductor layer.
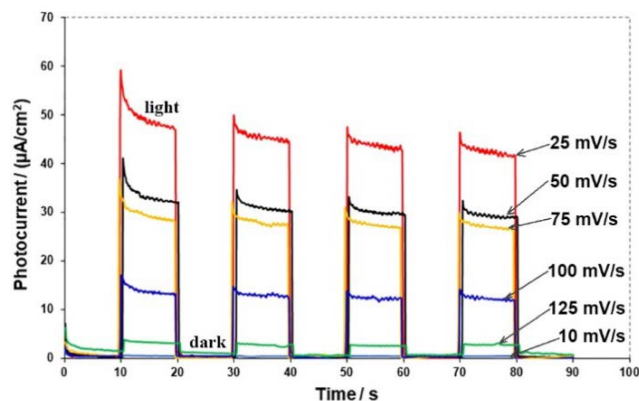
Figure 3 The photocurrent response from water oxidation of WO$_3$/Bi$_2$WO$_6$ photoanode prepared with different scan rates ranging from 10 to 125 mV/s.
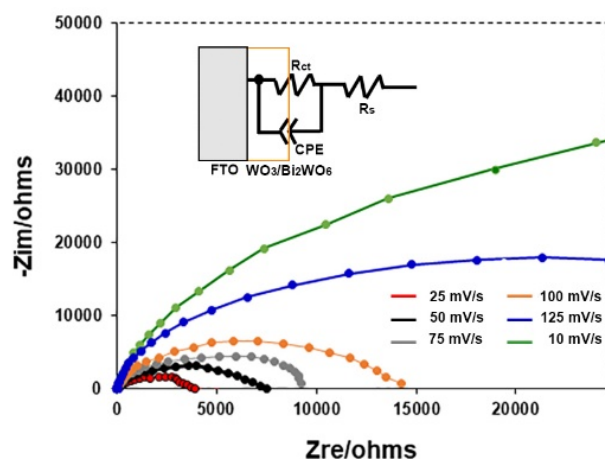
Figure 4 The Nyquist plot of WO$_3$/Bi$_2$WO$_6$ electrode for water oxidation under visible light.

Figure 4 displays the electrochemical impedance spectroscopy (EIS) data employed to examine charge transfer resistance characteristics inside the interfacial region of the WO$_3$/Bi$_2$WO$_6$ photoanode. The Inset of figure 4 depicts a circuit consisting of charge transfer resistance (Rct), solution resistivity (Rs), and electrical capacitance (CPE) that most closely reflects the reaction at the electrode-solution interface. The Nyquist plot in the provided figure depicts the characteristics of the WO$_3$/Bi$_2$WO$_6$ electrodes produced using a scan rate of 25 mV/s. The semicircle with the shortest radius on the plot indicates the lowest charge transfer resistance, which correlates with the maximum photocurrent observed in the previous findings. This relationship suggests that the high PEC properties of electrodes under optimal conditions result from their low charge transfer resistance, which is controlled by a slow

scanning rate when forming the film semiconductor with the desired properties.

Figure 5 displays X-ray diffraction patterns that illustrate the crystalline structure of the chemical composition of the FTO substrate and WO_3/Bi_2WO_6 electrode prepared at varied scan rates.
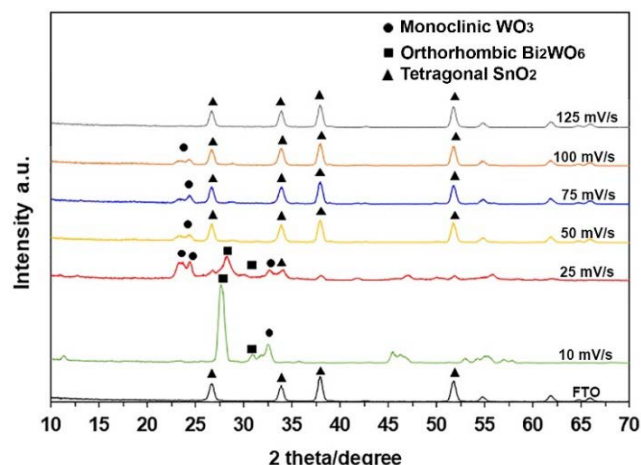
Figure 5 X-ray diffraction pattern of a bare FTO substrate compared to a WO_3/Bi_2WO_6 electrode produced with different scan rates conditions ranging from 10 to 125 mV/s.
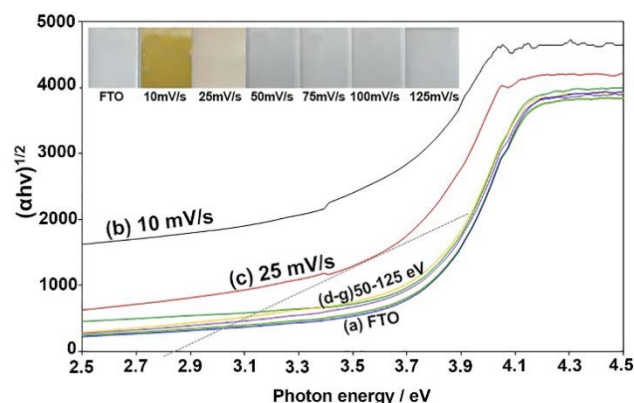
Figure 6 Correlation of absorbance coefficient and bandgap energy, inset of electrode photograph of (a) bare FTO substrate and FTO/WO_3/Bi_2WO_6 electrodes prepared with the different scan rates of (b) 10, (c) 25, (d) 50, (e) 75, (f) 100 and (g) 125 mV/s.

We discovered that the FTO substrate exhibited diffraction peaks at 26.7°, 34.1°, 38.02°, and 52.0°, which corresponded to tetragonal SnO_2 [17]. It was found that the prepared electrode at scan rates of 10 and 25 mV/s presented the main XRD peak at 2θ of 28.02°, 32.6°, which indicates the orthorhombic Bi_2WO_6 crystal structure on the FTO surface [18]. However, for the prepared electrode at a higher scan rate than 25 mV/s, a small amount of Bi_2WO_6 film is present.

It was observed that the produced electrode exhibits a small presence of Bi_2WO_6 semiconductor when applied to scan rates exceeding 25 mV/s. The X-ray diffraction (XRD) analysis reveals that the

composite WO_3/Bi_2WO_6 exhibits optimal formation. At the optimal scan rate of 25 mV/s, it can produce both a monoclinic WO_3 structure at 2θ of 23.6° and 24.4° and 32.5° [15] an orthorhombic Bi_2WO_6 structure, which results in excellent PEC properties.

Figure 6 exhibits the optical properties of the WO_3/Bi_2WO_6 electrode, including band energy and a photograph, as a result of the scan rate preparation procedure compared to the FTO substrate.

The WO_3/Bi_2WO_6 thin film prepared at a scan rate of 10 mV/s has the greatest thickness, the highest absorption properties, and the darkest yellow color, whereas increasing the scanning rate results in electrodes with softer colors and thinner films. The preceding results demonstrate that a slow scanning rate increases the bonding period of the semiconductor film to the electrode surface, resulting in a thick film, and the thickness decreases as the scan rate increases. The Tauc equation, shown in Equation 1, helped us confirm that the band gap energy (Eg) was 2.85 eV at the best scan rate of 25 mV/s for the electrode preparation conditions.

$$(\alpha h \upsilon)^{1/2} = \beta(h \upsilon - E_g) \qquad (1)$$

where β is a constant, α is the molar extinction coefficient, and Eg is the band gap energy. This Eg value was consistent with the optical absorption properties of the WO_3/Bi_2WO_6 semiconductor [19].

Figure 7 displays SEM images illustrating the morphology of composited WO_3/Bi_2WO_6 thin films on FTO substrates prepared at various scan rates with significantly different particle sizes and distributions. The particles of WO_3/Bi_2WO_6, which were prepared at a scan rate of 10 mV/s, exhibited a much larger particle size than those prepared under other conditions. This can be attributed to the extended accumulating period during the deposition process of the WO_3/Bi_2WO_6 thin films on the electrode substrate under the higher scan rate condition. The particles exhibited comparable size and dispersion. The samples prepared at a scan rate of 25 mV/s displayed increased porosity and greater surface roughness. The utilization of a scan rate of 25 mV/s in the preparation of the electrode has been found to significantly improve the morphologies of its surfaces. This improvement is characterized by an increased surface area and roughness, which enhances the effectiveness of solution contact and electron transport at the electrode surface. The obtained outcome provides robust evidence in favor of the PEC characteristics. Based on the investigation into the impact of scanning rate on the formation of WO_3/Bi_2WO_6 films using the CV technique, it can be inferred that a decreased scanning rate holds promise for augmenting the degree of precision in the deposition procedure. Consequently, this leads to the creation of films that demonstrate enhanced uniformity and distinct characteristics. Conversely, an increased

scanning rate may result in decreased control over the film's creation and a decline in quality. In summary, the scanning rate employed in cyclic voltammetry influences the kinetics of redox reactions, mass transport, film formation processes, and potential distribution within the electrochemical system. Slower scanning rates have been chosen to optimize reaction kinetics and increase the film-forming characteristics.
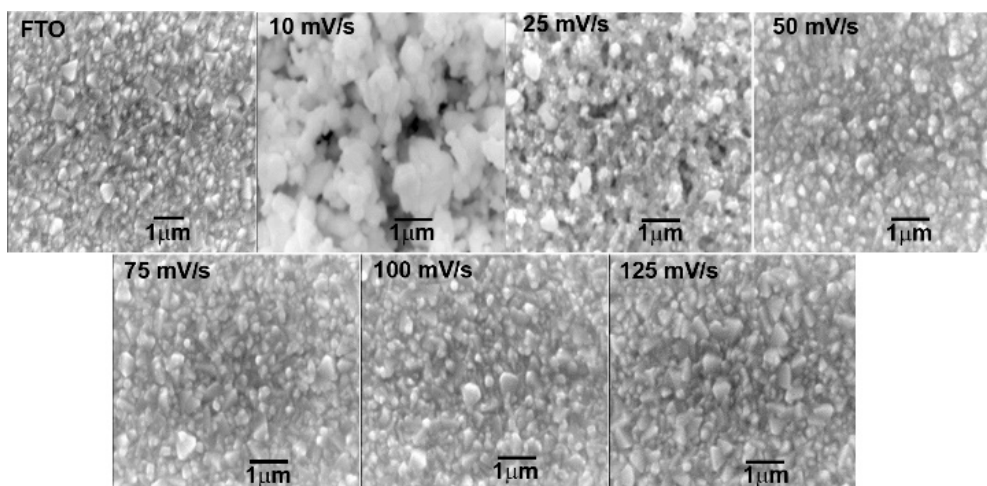
Figure 7 SEM images of a bare FTO substrate and an FTO/WO$_3$/Bi$_2$WO$_6$ electrode prepared with scan rates ranging between 10 and 125 mV/s.
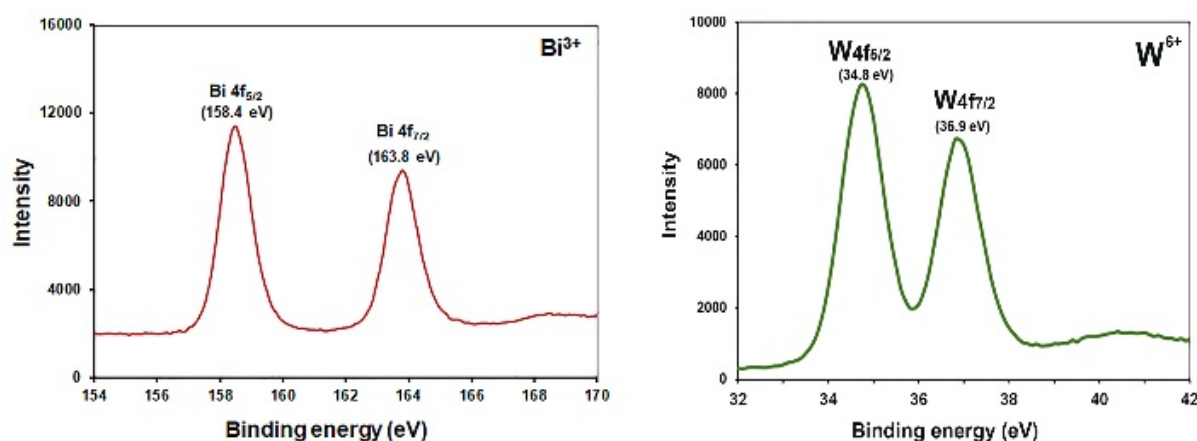
Figure 8 XPS spectra of Bi and W at FTO/WO$_3$/Bi$_2$WO$_6$ photoanode.

The composition of W, Bi, and O on the FTO/WO$_3$/Bi$_2$WO$_6$ electrodes was investigated by EDX analysis. Our findings unequivocally establish the presence of WO$_3$ and Bi$_2$WO$_6$ compounds on the FTO substrate. Furthermore, we investigate the chemical composition and oxidation state of all elements present in the composite WO$_3$/Bi$_2$WO$_6$ electrode utilizing the X-ray Photoelectron Spectroscopy (XPS) technique. The XPS spectra of all elements present in the WO$_3$/Bi$_2$WO$_6$ film were obtained by calibrating the binding energy using C1s (284.6 eV) as a reference. The experimental results indicate that the O1s orbital exhibits a binding energy of 530.8 eV. The XPS spectra of Bi4f$_{5/2}$ and Bi4f$_{7/2}$ orbitals exhibit binding energies of 163.8 eV and 158.4 eV, respectively, as shown in Figure 8. The energy levels of W$_{4f5/2}$ and W$_{4f7/2}$ were measured to be 34.8 eV and 36.9 eV, respectively. The findings validate the oxidation states of Bi^{3+} and W^{6+} seen at the WO$_3$/Bi$_2$WO$_6$ composite electrode [20]. The XPS and EDX findings offer significant insights that may be utilized to validate the chemical composition and chemical state of WO$_3$/Bi$_2$WO$_6$ present on the FTO substrate. The present study employed the optimum WO$_3$/Bi$_2$WO$_6$ photoanode to investigate the effectiveness of *E. coli* degradation under visible light irradiation and a bias potential of 1.5 V. Consequently, the PEC cell that was presented showed the capability to degrade 87.50 % of *E. coli* over a duration of 15 minutes. This finding confirms that the WO$_3$/Bi$_2$WO$_6$ electrodes that were produced are really effective in facilitating PEC oxidation, thereby enabling the elimination of *E. coli* in aqueous solutions. Moreover, these electrodes hold promise for potential application in removing microorganisms from wastewater.

CONCLUSIONS

We have successfully prepared the WO$_3$/Bi$_2$WO$_6$ photoanode using the CV method and applied it to the degradation of *E. coli* using the proposed PEC

cell. The scan rate in the CV method substantially impacts the characteristics and PEC activity of the composite WO_3/Bi_2WO_6 thin film fabrication. The optimal scanning rate condition is crucial for enhancing light absorption, surface morphology, and electron transport between the electrode and the electrolyte during the fabrication of WO_3/Bi_2WO_6 thin film electrodes. The optimal WO_3/Bi_2WO_6 photoanode fabrication condition for the highest PEC water oxidation properties was a scanning rate of 25 mV/s. We can conclude that the cyclic voltammetry scanning rate impacts the kinetics of redox reactions, mass transport, film formation processes, and potential distribution within the electrochemical system. The decision to take advantage of slower scanning rates has been made to optimize the kinetics of the reaction and enhance the film-forming characteristics of WO_3/Bi_2WO_6. The WO_3/Bi_2WO_6 composite material exhibits a notable capability for effectively eliminating *E.coli* in the photoelectrochemical (PEC) process. This finding suggests that the material holds promise for potential applications in eliminating other microorganisms present in wastewater.

ACKNOWLEDGEMENT

REFERENCES

1. Voumard M, Breider F, Von Gunten U. Effect of cetyltrimethylammonium chloride on various Escherichia coli strains and their inactivation kinetics by ozone and monochloramine. Water Res. 2022;216:118278.

2. He H, Sun S, Gao J, Huang B, Zhao T, Deng H, et al. Photoelectrocatalytic simultaneous removal of 17α-ethinylestradiol and *E. coli* using the anode of Ag and SnO_2-Sb 3D-loaded TiO_2 nanotube arrays. J Hazard Mater. 2020;398:122805.

3. Zheng Z, Lo IMC. Fabrication of MoS_2@BL-$BiVO_4$ photoanode with promoted charge separation for photoelectrochemical sewage treatment to simultaneously degrade PPCPs, disinfect *E. coli*, and produce H_2: Performance, mechanisms, and influence factors. Applied Catalysis B: Environmental. 2021;299:120636.

4. Srisawang N, Ngernchuklin P, Chaiyasat A, Chaiyasat P. Polymer microcapsules encapsulating photocatalyst nanoparticles for dye treatment in wastewater. J Appl Res Sci Tech. 2020;19(2):1-16.

5. Li G, Yang C, He Q, Liu J. Ag-based photocatalytic heterostructures: Construction and photocatalytic energy conversion application. Journal of Environmental Chemical Engineering. 2022;10(3): 107374.

6. Liu J, Ma N, Wu W, He Q. Recent progress on photocatalytic heterostructures with full solar spectral responses. Chem Eng J. 2020;393:124719.

7. Koutavarapu R, Babu B, Reddy CV, Reddy IN, Reddy KR, Rao MC, et al. ZnO nanosheets-decorated Bi_2WO_6 nanolayers as efficient photocatalysts for the removal of toxic environmental pollutants and photoelectrochemical solar water oxidation. J Environ Manage. 2020;265:110504.

8. Sadhasivam S, Anbarasan N, Gunasekaran A, Sadhasivam T, Jeganathan K, Oh TH. Highly efficient In_2S_3 nanosphere decorated WO_3/Bi_2WO_6 dual heterostructure nanoflake arrays for enhanced low bias watersplitting under visible light irradiation. Surfaces and Interfaces. 2023;39:102892.

9. Girish Kumar S, Koteswara Rao KSR. Tungsten-based nanomaterials (WO_3 & Bi_2WO_6): Modifications related to charge carrier transfer mechanisms and photocatalytic applications. Appl Surf Sci. 2015;355: 939-58.

10. Supanantin F, Ponchio C. WO_3/$BiVO_4$ photoanode electrode improvement for photoelectrocatalytic dye degradation. J Appl Res Sci Tech. 2020;19(1):16-26.

11. Ponchio C, Supanantin F, Petsaen N, Poowancum A. Photoelectrocatalytic oxygen production from water splitting using WO_3 photoanode fabricated by dip coating technique. J Appl Res Sci Tech. 2019; 18(1):52-9.

12. Zhang P, Teng X, Feng X, Ding S, Zhang G. Preparation of Bi_2WO_6 photocatalyst by high-energy ball milled Bi_2O_3-WO_3 mixture. Ceram Int. 2016;42(15):16749-57.

13. Juodkazytė J, Petrulevičienė M, Parvin M, šebeka B, Savickaja I, Pakštas V, et al. Activity of sol-gel derived nanocrystalline WO_3 films in photoelectro-chemical generation of reactive chlorine species. J Electroanal Chem. 2020;871:114277.

14. Su X, Liu C, Liu Y, Yang Y, Liu X, Chen S. Construction of $BiVO_4$ nanosheets@WO_3 arrays heterojunction photoanodes by versatile phase transformation strategy. T Nonferr Metal Soc. 2021;31(2):533-44.

15. Supanantin F, Ponchio C. Improvement ITO/WO_3 photo anode electrode fabrication using electrodeposition technique for highly efficient photoelectrocatalytic insecticide degradation. Mat Sci Semicon Proc. 2020;118:105212.

16. Orimolade BO, Idris AO, Feleni U, Mamba B. Peroxymonosulfate assisted photoelectrocatalytic

degradation of pharmaceuticals at a FTO-Bi$_2$WO$_6$ electrode: Mechanism and kinetics studies. Catal Commun. 2022;169:106481.

17. Suryakant, Kumar N, Tripathi H, Kumar S, Bhardwaj S. Sol-gel synthesis of Tin oxide nanoparticles and their characterizations. Materials Today: Proceedings. 2023.

18. Shkir M, AlAbdulaal TH, Ubaidullah M, Reddy Minnam Reddy V. Novel Bi$_2$WO$_6$/MWCNT nanohybrids synthesis for high-performance photocatalytic activity of ciprofloxacin degradation under simulated sunlight irradiation. Chemosphere. 2023;338:139432.

19. Zhu Z, Yan Y, Li J. One-step synthesis of flower-like WO$_3$/Bi$_2$WO$_6$ heterojunction with enhanced visible light photocatalytic activity. J Mater Sci. 2016;51(4):2112-20.

20. Peng Y, Chen Q, Wang D, Zhou H, Xu A. Synthesis of one-dimensional WO$_3$-Bi$_2$WO$_6$ heterojunctions with enhanced photocatalytic activity. Cryst Eng Comm. 2015;17(3):569-76.

Efficiency of wastewater treatment from environmental laboratory of science and technology, RMUTP using ozonation

Supachai Hirunsupachote[*], Woranuch Deelaman, Ronnapop Putrakulpattana, Krittikan Sarapirom and Palchat Wongkaew

Division of environmental Science and Technology, Faculty of Science and Technology, Rajamangala University of Technology Phra Nakhon, Bangkok 10800, THAILAND

[*]Corresponding author: supachai.h@rmutp.ac.th

ABSTRACT

Wastewater from the laboratory in the Division of Environmental Science and Technology, Faculty of Science and Technology, Rajamangala University of Technology Phra Nakhon is a source of pollution without any treatment. Researchers realized that it would become an environmental problem in the future. For this reason, wastewater treatment from water laboratory would be studied using ozonation process because the researchers want to use the existing equipment in the laboratory and a simple technique that the students can do. This aims to treat the wastewater until it passes the water standard. The laboratory's wastewater characteristics were unclear based on the study. The pH values measured were 8.15, 3.35, and 2.49, respectively. COD levels were monitored of 10,480, 2,400, and 3,040 mg/L, while the measured BOD values were 4,649, 1,683, and 2,200 mg/L, respectively. Additionally, the SS concentrations were 682, 788, and 548 mg/L, respectively. Because of these characteristics using only the biodegradation process didn't work. The ozonation techniques were a good option following the research objective. The results showed that the suitable condition for the ozonation process was pH6 and the optimal time was 40 minutes. Because after 40 minutes the COD removal increase only 5% but after 60 minutes the ozonation had no effect on COD removal. This condition was applied before using biological treatment via a sequence batch reactor (SBR). Using microorganisms and 8 hours of aeration via SBR, the efficiency of COD BOD and SS removal was only 41.66, 0 and 71.82 percent, respectively. Filling ozone in rate 0.25 gram/hour/liter wastewater with SBR reactor, the wastewater treatment efficiency increased. It can remove COD, BOD and SS of 63.15, 50.00 and 72.63 percent, respectively. The advantage of this research was that the ozone generator can be applied for wastewater treatment without additional costs.

Keywords: Ozonation, Wastewater treatment, COD removal efficiency, SBR, Oxidation process

INTRODUCTION

The wastewater activities is one important problem in many university in Thailand. Division of Environmental Science and Technology, Faculty of Science and Technology, Rajamangala University of Technology Phra Nakhon tried to solve this problem to be the pilot model for other universities. Because wastewater from laboratories can be almost drained to the sink without treatment process. However, this problem shouldn't be ignored because the wastewater without a treatment process that is released into our environment is dangerous to the environment and humans. Recently, the wastewater in the laboratory in the Division of Environmental Science and Technology, Faculty of Science and Technology, Rajamangala University of Technology Phra Nakhon has almost consisted of wastewater from experiments and washing. In the laboratory, wastewater in laboratory has a low or high pH and can corrode the pipe. Because

laboratory activities are involved in the different effluent characteristics. Not only was the resource of wastewater for study in the classroom from different area such as from resident areas, or industry but also from different activities in the classroom such as biochemical oxygen demand (BOD), chemical oxygen demand (COD), suspended solids (SS), nitrogen or heavy metal analysis. Each activity required a different chemical substance. Now, the wastewater is collected in the big tank. And when the wastewater was full, it was sent to the wastewater treatment company.

It can be good when we can save on this cost. And the ozone generator is a good option because it is a basic device used for studying in a student class. The ozonation process was widely used in wastewater treatment systems. In addition, ozone is a strongoxidizing agent for organic or chemical material removal in wastewater [1]. According to the water standard in Thai law, the pH of the wastewater released from the

building, the pH is in range [5-9]. The BOD is less than 20-40 mg/L, and the SS is less than 30-50 mg/L depending on the type of building [10]. The characteristics of wastewater, such as COD and BOD, that contact the ozone can be reduced in a short time [2]. Not only save the time, but also it can save the cost too. Moreover, it can be oxidized the hard bio-degradable or toxic substance by oxidation process in some cases [3].

In this research, we try to use the ozonation process to treat the wastewater in the classroom. The ozonation process is a good option because the equipment is easy to use. The study parameters in this research were pH, BOD, COD and SS. However, using only the ozonation process in the wastewater treatment wasn't enough [4]. In this research SBR (Sequencing Batch Reactor) was used after the ozonation process to remove BOD, COD and SS in the final to pass the law of wastewater standard in Thailand. The advantage of this work is that the ozone ozone generator that is available in the laboratory can treat the wastewater. It can be applied without additional cost. This practice will be the pilot model for other universities or some organizations because almost every wastewater laboratory has this ozone generator.

MATERIALS AND METHODS

Experimental setup

A schematic diagram in Figure 1 was helpful in comprehending the experimental setup. And the details were described below.

Wastewater characteristics

The wastewater was from a classroom in the wastewater pollution laboratory. It was almost from the Bang-Khen Canal near the university. And some wastewater was collected from the wastewater treatment plant at the palm oil factory in Chonburi. The wastewater was used for the study almost exclusively for the wastewater parameter analysis. After that, it was collected until it was full. It was sampled three times and measured the parameters such as pH, BOD, COD and SS.

Ozonation process

The ozonation process was studied. The ozone generator brand "incorporate ozonizer" model "FA1000" from Fisher Scientific company was used and adjusted at maximum level. Firstly, the ozone filling rate was investigated and secondly, the optimal conditions such as ozonation time and pH were investigated. The ozone was generated from the ozone generator shown in Figure 2. COD was studied as a parameter to investigate the optimal conditions for testing ozonation time between 0-120 min and pH between [4-10]. The COD was measured following the standard method 5220D [6].
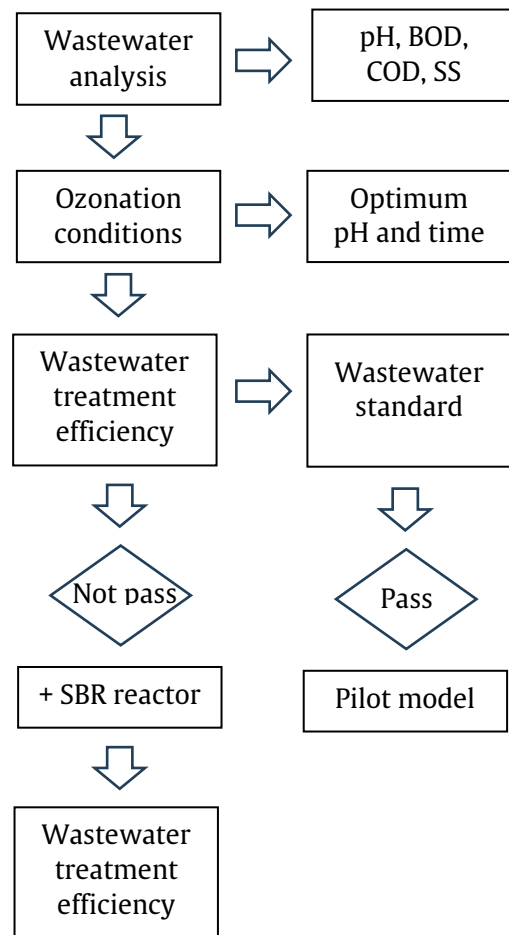
Figure 1 schematic diagram for the experiment setup.

Figure 2 Wastewater treatment using the ozonation process.

Wastewater treatment using ozonation and SBR

Firstly, the wastewater was treated with ozone at various times. In this experiment, the ozonation time of 10, 20, 30 and 40 minutes with an optimal pH at room temperature was tested. After that, the wastewater was left for 24 hours for ozone volatilization. The SBR (Sequencing Batch Reactor) was used after that. The aerobic process uses aeration and filling inoculum from a wastewater treatment plant for 8

hours and 48 hours for precipitation. The efficiency of COD, BOD and SS removal from ozonation and aerobic processes was investigated compared with a single SBR process. The COD, BOD and SS from the treatment process were compared with the wastewater standard.

RESULTS AND DISCUSSIONS

Wastewater characteristics from the laboratory

The results for wastewater characteristics are shown in Table 1. The result found that the COD was varied because the wastewater from the classroom in each period was different. The COD can be 2,400 - 10,480 mg/L while the BOD was in the range of 1,683 - 4,649 mg/L. It can be said that the oxidized matter in

wastewater was also various. However, the rage from easy-biodegradable substances wasn't significantly different from COD. From sample 1, the COD was 10,480 mg/L and the BOD was 4,649 mg/L. Although the wastewater was almost bio-degradable, it consisted of chemical substances from the experiment. The wastewater in the laboratory was also sometimes composed of hard biodegradable substances. The ozonation was also a good option for wastewater treatment. Using ozone is a chemical treatment. It can treat the chemical substance in wastewater better than biological treatment. Considering the SS parameter, it wasn't significantly different either. The wastewater from the classroom in the laboratory had a difference in oxidized substances. Thus, the ozonation process would be a good option for reducing COD in the beginning step.

Table 1 Wastewater characteristics in the laboratory classroom.

Parameter	Sample 1	Sample 2	Sample 3
pH	8.15 ± 0.01	3.35 ± 0.02	2.49 ± 0.01
BOD	4,649 ± 23.52	1,683 ± 8.64	2,200 ± 13.82
COD	10,480 ± 83.52	2,400 ± 13.52	3,040 ± 25.63
BOD/COD	0.44	0.70	0.65
SS	682 ± 13.52	788 ± 14.78	548 ± 9.66
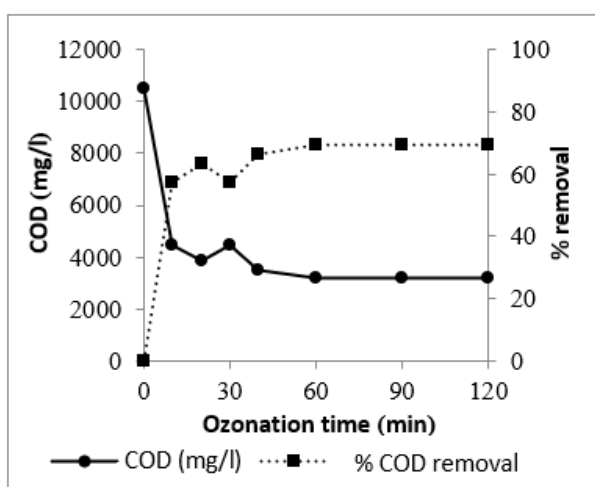
Figure 3 Ozonation time effects on COD.
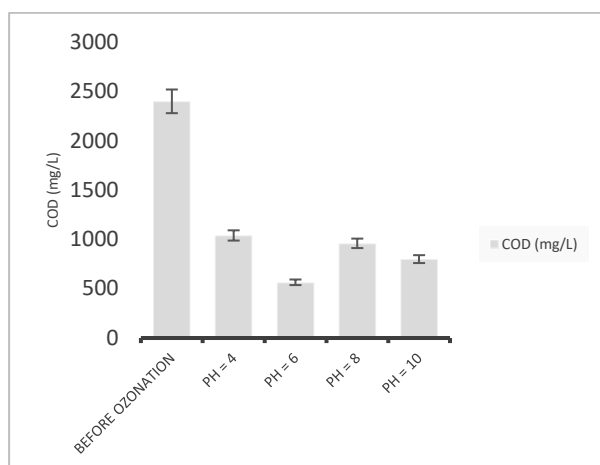
Figure 4 pH condition effecting on COD.

Optimal condition for the ozonation process

Ozone is a strong oxidizing agent. Not only organic matter but also inorganic matter such as chemical substances for wastewater parameter analysis Ozone can be used as the primary chemical process to improve the degradation efficiency of stable organic compounds in wastewater. The oxidizing agent has a high standard reduction potential (E^o) of +2.07 V. It measures the tendency of a chemical species to be reduced or its oxidizing capability. Also, it can be used to oxidize various recalcitrant organic pollutants to reduce these pollutants to smaller compounds that are less harmful to humans and aquatic environments. As a strong oxidizing agent, ozone can directly degrade pollutants in effluents or indirectly via the short-lived hydroxyl radicals (OH) (E^o +2.80 V). These free radicals will attack certain reactive groups in organic molecules to degrade them into smaller oxidation products [11].

Figure 3 and Figure 4 show the optimal conditions for the ozonation process. The result found that Ozonation process can remove COD rapidly in 40 minutes. After that, the COD removal didn't differ significantly. After 60 minutes, filling the ozone had no effect on COD removal. This result was confronted by the study of [5] that the ozonation in a long time over 1 hour hadn't influenced increasing COD and BOD removal efficiency.

The ozonation process had a cost for electricity and it took the time. Also, the ozonation time between 10 - 40 minutes was suitable. For a suitable pH, when the ozone was filled in 10 minutes, it was 6 (shown in

Figure 4). Cañizares et al., 2007 reported that the suitable pH for ozonation process was 6 too [7]. From Table 1, the pH of the wastewater in the laboratory experiment was various. Comparing the cost of chemical substances for pH adjustment and increasing COD removal efficiency. It was worth adjusting the pH.

Wastewater treatment efficiency using ozonation and SBR process

Table 2 shows the COD and BOD efficiency of the SBR reactor compared with Ozonation and SBR reactor. In the previous study, the suitable condition for the ozonation process was pH 6, and the optimal time was 40 minutes. Filling ozone in rate 0.25 gram/hour/liter. Filling ozone in rate 0.25 gram/hour/liter. The result found that COD and BOD removal from SBR reactor are very low. It can remove the COD and BOD maximums of only 41.66 and 13.33%, respectively. It can be said that the SBR, which is a biological process wasn't suitable for wastewater from laboratories because it almost consists of hard biodegradable substances. For sample 4, using the ozonation process for 40 minutes, the biological treatment wasn't suitable for this wastewater sample. Only biological processes can't treat wastewater samples in this case. That is a reason why we used ozonation process. But when the ozonation combined with the SBR reactor is used, it can increase COD and BOD removal significantly. [9] reported that the combination process of ozone and an aerobic reactor can increase the COD and BOD removal efficiency by 112%. Because the ozonation process can reduce the COD maximum to 82.2% [8]. For the SS removal, ozone can't increase SS removal efficiency. However, the aerobic process was necessary for SS removal because of the precipitation step [9].

The mechanism of biological wastewater treatment is different from chemical treatment such as the ozonation method. The treatment of wastewater subsequent to the removal of suspended solids by microorganisms such as algae, fungi, or bacteria under aerobic or anaerobic conditions during which organic matter in wastewater is oxidized or incorporated into cells that can be eliminated by the removal process or sedimentation is termed biological treatment. Also, biological treatment is almost always applied as a secondary treatment [12].

However, the microorganisms in wastewater treatment systems are sensitive to ozone. In this study, using SBR as a secondary treatment can't increase the efficiency significantly. Although the ozonation process can increase the COD and BOD removal efficiency, the wastewater treatment system should be improved in the future.

Table2 COD, BOD and SS removal using ozonation and SBR process.

Time (min)	COD (mg/L)	COD removal (%)		BOD (mg/L)	BOD removal (%)		BOD/COD	SS (mg/L)	SS removal (%)	
		SBR	Ozone + SBR		SBR	Ozone + SBR			SBR	Ozone + SBR
0	3,040	-	-	2,200	-	-	0.72	548	-	-
10	1,440	25.00	52.63	1,300	13.33	40.90	0.90	125	70.02	77.01
20	1,440	25.00	52.63	1,050	4.54	52.27	0.72	120	70.08	73.36
30	1,280	11.11	57.89	1,000	11.11	54.55	0.78	124	70.11	63.14
40	1,120	41.66	63.15	1,100	0	50.00	0.98	112	71.82	72.63

CONCLUSION

In this study, the wastewater treatment from the laboratory in the Division of Environmental Science and Technology, Faculty of Science and Technology, Rajamangala University of Technology Phra Nakhon using the ozonation process is suitable in this case. While the aerobic process wasn't suitable for wastewater from laboratories because the wastewater consisted of toxic or hard-degradable substances. The suitable condition for the ozonation process was pH 6, and the optimal time was 40 minutes. Filling ozone at a rate of 0.25 gram/hour/liter of wastewater can remove COD, BOD, and SS of 63.15, 50.00, and 72.63 percent, respectively. It can be concluded that the wastewater in the laboratory consisted of hard-digestible, biodegradable substances. Sometimes it consisted of an oxidized chemical substance. And ozone can be a good oxidizing agent.

ACKNOWLEDGEMENT

REFERENCES

1. Siyu C, Xiaomeng R, Gengbo R, Zizhang W, Zhimin W, Tiantong R, et al. Comparison of fenton and ozone oxidation for pretreatment of petrochemical wastewater: COD removal and biodegradability improvement mechanism. Separations. 2022;9(7):179.

2. Issaka E, Amu-Darko J, Yakubu S, Fapohunda FO, Ali N, Bilal M. Advanced catalytic ozonation for degradation of pharmaceutical pollutants-A review. Chemosphere. 2021;289:133208.

3. Jing Z, Shuo-Jing Z, Chun L, Jia-Ze S, Xiao-Xuan C, Lei Z, et al. Influence of industrial wastewater quality on advanced treatment of microbubble ozonation. Huan Jing Ke Xue. 2020;41(4):1752-60.

4. Jianlong W, Hai C. Catalytic ozonation for water and wastewater treatment: Recent advances and perspective. Sci Total Environ. 2020;704:135249.

5. Al-Khashman OA. Chemical evaluation of Ma'an sewage effluents and its reuse in irrigation purposes. Water Resour Manage. 2009;23:1041-53.

6. American Public Health Association (APHA). American Water Works Association, Water Environment Federation, Standard methods for examination of water and wastewater. 21st ed. Washington DC: USA; 2005.

7. Cañizares P, Lobato J, Paz R, Rodrigo MA, Sáez C. Advanced oxidation processes for the treatment of olive-oil mills wastewater. Chemosphere. 2007;67: 832-8.

8. Chun-du W, Jin-yu C, Ning L, Cheng-wu Y. Ozone oxidation of photographic processing wastewater in a batch reactor. Int J Plasma Environ Sci Technol. 2007;11(2):135-40.

9. Kishimoto N, Morita Y, Tsuno H, Yasuda Y. Characteristics of electrolysis, ozonation and their combination process on treatment of municipal wastewater. Water Environ Res. 2007;79(9):1033-42.

10. Announcement of the Ministry of Natural Resources and Environment on setting control standards Announcement of wastewater drainage from certain types and sizes of buildings, dated 7 November 2005, announced in the Royal Gazette, Volume 122, Section 125D.

11. Mohamed HA, Ahmad ZA. Mechanism and reaction kinetic of hybrid ozonation-ultrasonication treatment for intensified degradation of emerging organic contaminants in water: A critical review. Chemical Engineering and Processing-Process Intensification. 2020;154(19):108047.

12. Mohamed S, Biological and Chemical Wastewater Treatment Processes, Wastewater Treatment Engineering, Intech Open. 1st ed. Cairo: Egypt; 2015.

Optimizing pick-place operations: Leveraging k-means for visual object localization and decision-making in collaborative robots

Naphat Yenjai and Nattasit Dancholvichit[*]

Department of Mechatronics Engineering, Faculty of Engineering, Rajamangala University of Technology Rattanakosin, Nakhon Pathom 73170, THAILAND

[*]Corresponding author: nattasit.dan@rmutr.ac.th

ABSTRACT

This article presents an approach to object localization algorithms for pick-place operations in collaborative robots by utilizing conventional color segmentation in computer vision and k-means clustering. Adding the k-means clustering algorithm complements the color segmentation by distinguishing and grouping the sections of similar pixels; hence, object localization is more accurate. The order of pick-place operations of each cluster acquired from the proposed algorithm is prioritized based on L^2 norm. Integrating the proposed framework provides a well-structured depiction of the localized objects, which is fundamental for successful pick-place operations. The TCP/IP communication framework via socket communication is established to facilitate data transmission between the robot and the host computer. The objective is to ensure that the robot's end effector performs as directed by the host computer by obtaining information on the pick-and-place operation, including the localized coordinates, dimensions, the order of operations, and the pose of the objects of interest to the robot. In this experiment, a cobot arm is employed to autonomously pick and place objects with different shapes and colors in a workspace filled with diverse objects, requiring the robot to choose the closest objects to operate based on the data from the host computer. Our results demonstrate the effectiveness of this integration, showcasing the enhanced adaptability and efficiency of pick-place operations in collaborative robots. This study indicates 98% accuracy in pick-and-place operations with an average latency of 0.52 ± 0.1 s, indicating an improvement compared to the traditional algorithm without k-means clustering, which achieves an accuracy of 88%. Additional studies reveal that when incorporating pose estimation into the pick-place operations, the proposed algorithm's accuracy is 94%. The demonstration highlights the potential of leveraging machine learning algorithms and computer vision from the camera to perform flexible pick-place operations via socket communication.

Keywords: Cobots, Pick-place operations, K-means clustering, Object localization

INTRODUCTION

The emergence of Industry 4.0 and the intelligent factory concept has introduced a range of significant technological advancements with the potential to facilitate the development of intelligent products and services [1]. Creating a versatile and adaptable assembly system necessitates integrating various enabling resources and technologies. Collaborative robots, or cobots, are emerging as a technology that offers enhanced flexibility and quick adaptation in assembly processes. Unlike traditional industrial robots, cobots can work alongside individuals without fencing or enclosure [2]. Human-robot collaboration (HRC) involves humans and cobots working together in the same workspace to execute manufacturing processes, leveraging the strengths of both for task completion [3]. Designing a collaborative human-robot workplace poses challenges, requiring adherence to specific design guidelines [4]. These processes can include pick-and-place tasks [5], assembly [6], screwing [7], or inspection [8]. Although cobots demonstrate exceptional performance in collaborating on complex tasks with humans, their reliance on expensive industrial-grade cameras presents limitations in flexibility and adaptability to diverse industrial applications. The cost-intensive nature of implementing and reprogramming robots and their limited ability to effectively navigate dynamically changing environments pose a significant obstacle

for small companies seeking to integrate cobots into production lines.

By harnessing the potential of computer vision coupled with machine learning, cobots can potentially undertake more intricate tasks in collaboration with humans, thereby increasing the overall complexity of operations. Typically, engineers input basic commands or position controls in the native language of the robot to enhance ease of use, simplifying both operation and configuration [9, 10]. However, this also constrains their versatility, narrowing down the range of tasks they can effectively perform as these high-level languages are limited to a small number of applications [11, 12]. Compared to industrial-grade cameras, cost-effective cameras in the current market are widely adopted to assist with machine vision tasks. This solution enables cobots to effectively collaborate with humans, performing product quality control and component assembly inspection tasks. Cobots can perceive their surroundings, perform tasks, and make informed decisions through network communication, achieving comparable performance to high-end devices. By setting up a system where cameras are linked to a host computer and provide data to the cobot through TCP/IP (Transmission Control Protocol/Internet Protocol) [13], the computer can process the visual data captured by the webcams and transmit it to the cobot. With this cost-effective implementation, the cobot can effectively collaborate with the human operator and perform flexible tasks based on computer vision analysis.

Pick-place operations play a fundamental role in various robotic applications. While these operations have become well-established in structured scenarios, challenges arise when dealing with parts of high variability or in less structured environments, especially for HRC. In such cases, pick-place operations are limited to mostly laboratory settings and have not been widely adopted in the market due to inefficiency, lack of robustness, and limited flexibility in existing manipulation and perception technologies [14]. Numerous studies have addressed these challenges to enhance HRC by enhancing object recognition, localization, and pick-and-place operations. In [15], computer vision and image transformation are used to determine the location of the objects to perform pick-place operations. Support Vector Machines (SVM) have been employed to classify successful and failed scenarios [16], while the Point Distribution Model (PDM) has been used to compute generalized success models [17]. In recent studies, most of the work focuses on machine learning algorithms developed where multiple stages of object classification are implemented, including deep learning and point cloud processing [18]. Another recent study explores object detection and recognition in the context of a pick-and-place robot, focusing on edge detection and feature extraction utilizing an Artificial Neural Network (ANN) [19]. Multiple Reinforcement Learning (RL) techniques [20] are also explored to perform task-specific operations, such as pick-place operations without direct programming. These studies provide algorithms that yield high accuracy, providing the computational power is high and sufficient to operate such approaches. Meanwhile, the k-means algorithm has found application in various machine vision scenarios used with cobots, such as in pick-and-place and sorting operations, notably in handling cherry tomatoes. The algorithm uses a color patch-based visual tracking algorithm to precisely detect and pick ripe tomatoes [21]. Another relevant research area pertains to hand gesture recognition as an input command for the Bioroid Premium Robot, with studies exploring the use of k-means clustering and SVM techniques [22].

While computer vision has been extensively utilized in various applications, its reliance on complex image processing algorithms and manual tuning parameters can lead to challenges in achieving high accuracy and robustness. In specific scenarios, sophisticated approaches require substantial computational resources. By incorporating simpler machine learning algorithms into the vision system, it becomes feasible to optimize the framework. This involves decreasing reliance on intricate vision algorithms and harnessing the power of machine learning to enhance accuracy in object recognition, localization, and manipulation tasks. In this study, we propose an algorithm that enhances object localization accuracy by leveraging both machine vision and k-means clustering. This study employs an eye-on-hand approach, focusing on retrieving and performing pick-place operations on a specific object chosen by the user and placing it in a designated target location. A camera is used for capturing images, and the algorithm utilizes computer vision and k-means clustering for improved performance. The host computer employs OpenCV for color segmentation, and the k-means algorithm identifies pick-and-place locations in order. The algorithm also determines the location of the desired object from others and prioritizes the sequence of retrieval based on its L^2 norm. The implementation involves the targeted object's decision algorithm and pick-place operations, with predefined trajectories stored on the host computer. The coordinate and pose information is then transferred to the cobot to

manipulate the designated object precisely via socket communication.

This article first introduces the experimental setup, followed by a methodology section that describes the algorithms and communication techniques employed in the study. The results and discussion section are presented next. Finally, the conclusions are given.

MATERIALS AND METHODS

Experimental setup

In this experiment, a cobot arm is used to pick and place objects of different shapes and colors. The workspace contains multiple objects of varying shapes and sizes, and the robot must identify the objects of interest and prioritize them for picking and placing. The machine must be able to identify the objects of interest and prioritize the order of pick-place operations such that the closest objects are selected first. In this study, Gofa IRB 15000 Cobot, manufactured by ABB equipped with an OAK-D LITE camera [23], was used to capture images of objects in eye-on-hand configuration, as shown in Figure 1. The IRB 15000 is capable of a payload of 5 kg, a reach of 1.62 m, a speed of up to 2.2 m/s, and a resolution of 0.02 mm.

Figure 1 Cobot is equipped with an eye-on-hand camera to be used in this study of pick-place operations.

Once the experimental session starts, the algorithm, which incorporates computer vision techniques and the k-means clustering algorithm for object localization, is executed. The computer vision component analyzes the visual data captured by the camera, extracting relevant information about the objects present in the scene. This information includes object shapes, positions, and other features necessary for object recognition and localization. The number of pick-place operations the cobot performs throughout the experimental session is counted and recorded. This measurement serves as a metric to evaluate the efficiency and effectiveness of the algorithm and the system's overall performance. It helps assess the ability of the algorithm to locate objects accurately, determine appropriate pick-and-place sequences, and successfully execute the manipulations.

Methodology

The proposed methodology for this study is divided into three main parts, as shown in Figure 2. First, the PC host is where the computation of the picking location takes place. It consists of the preprocessing, the segmentation algorithm, and the k-means algorithm, respectively. Then, the host sends command data to the collaborative robot software via socket communication, which ensures efficient object manipulation and interaction. Finally, the cobot receives information about the objects of interest and commands related to picking. It then instructs the high-level controller to perform pick-place operations by calculating the inverse kinematics for each joint. The end effector in this study is a pneumatic actuator for the case that does not utilize pose estimation and a mechanical gripper for the case that introduces pose estimation, respectively.
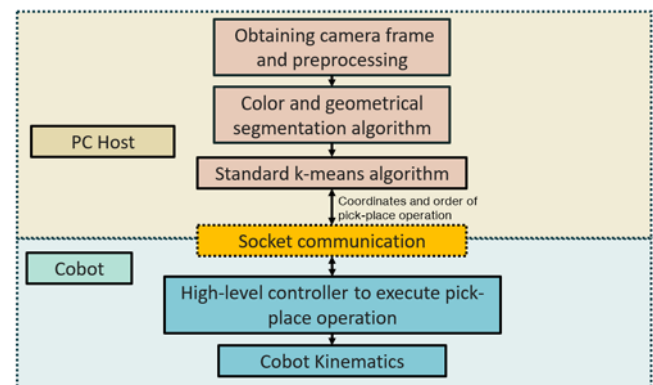
Figure 2 The proposed methodology and its associated diagram.

a. Computer vision: Preprocessing and segmentation algorithm

Before segmentation, denoising techniques aim to eliminate unwanted noise from images, enhancing the data quality and improving the accuracy of subsequent steps. In this study, noise reduction is performed to eliminate various types of noise, mainly Gaussian noise, ensuring that the input data is more reliable, leading to more precise and consistent segmentation results. Next, the image segmentation algorithm divides the input image into meaningful regions or segments, thereby identifying distinct objects or regions of interest. This initial segmentation step helps distinguish objects from the background and separate them for further analysis.

Here, the algorithm of the host computer primarily relies on OpenCV, a widely utilized computer vision library, for color segmentation to locate a specific-colored object captured by a camera. The filtered image is converted to the HSV color space, enabling the separation of color information from brightness. A mask is then created by setting lower and upper HSV thresholds, effectively isolating pixels with color of interest. The findContours function detects the contours of these specific pixels, focusing solely on the outer contours. The calculated value is compared to a predetermined threshold to assess if the object closely matches the desired shape to ensure further shape validation. For instance, one of the shape parameters is calculated using circularity, $C = 4\pi A/P^2$, where A is the contour area, and P is the contour perimeter, respectively. For the case of a spherical object, C is close to 1.

In addition, to detect the location and estimate the pose of non-circular, for instance, rectangular objects, the minAreaRect function in OpenCV is utilized. The minAreaRect function in OpenCV is used to find the minimum area rectangle that encloses a set of points. This methodological approach involves tracing a continuous and unbroken curve that precisely outlines the spatial boundaries of the square under examination. It can detect and localize non-circular objects, such as rectangles or bounding boxes of the objects in an image. The center, width, and height of the rectangular object can be identified, as well as the decision of the picking location of the objects. In terms of orientation, the object's rotation angle is also utilized. This is a particular case so that the 6th joint of the cobot can be adequately rotated prior to picking the objects according to the z-axis rotation (Rz). The Rz transformation benefits the robot arm that uses a gripper to pick up objects. Further, this can also perform pose estimation, determining the position and orientation of identified objects.

These two segmentation algorithms are used to identify the objects' types, shapes, locations, orientations, and poses. With slight tuning of parameters, the algorithm can identify the objects' properties. For instance, contours with circularity above the threshold can differentiate one object from another or the rectangular object with its associated pose. Those segmented images will then be used to split the data into small clusters of images. Subsequently, the objects are grouped into data clusters that will be sent as input to the k-means clustering algorithm.

b. K-means algorithm

The k-means algorithm is employed to perform clustering of the objects, deciding the order of operation into subtasks using the L-2 norm. Following the segmentation of the image, the k-means algorithm is subsequently employed. K-means is an unsupervised machine-learning algorithm commonly used for clustering tasks. The k-means clustering algorithm is notable for its simplicity, accessibility to implementation, and efficiency, as it can process large datasets that can also be scaled. In addition, it is incredibly versatile and can be used with varying scales and dimensions. However, k-means clustering has drawbacks as the algorithm is highly sensitive to the predefined k values, which is challenging to determine. Outliers also impact the results, which necessitate pre-processing before applying k-means clustering to maintain accuracy. One of the main disadvantages of the algorithm is that it is highly susceptible to converging to local minima, posing a challenge in cases where its data, especially for each complex cluster, is not well-separated. In object localization, the k-means algorithm helps in grouping similar pixels. By iteratively assigning pixels to different clusters and optimizing their centroids, the k-means algorithm is also applied to the data to find the characteristics of each object and perform clustering. The k-means algorithm is an algorithm that groups the given data into k clusters. When this algorithm receives n objects, it is divided into k groups that are less than or equal to n, and each group forms a cluster. Here, k is determined from image segmentation acquired from *Section a*.

Each cluster represents a centroid of potential pick-and-place location. The algorithm iteratively changes the location of the centroid, and it runs until the centroids converge. In other words, to achieve optimal clusters, the variance in the distance difference between each cluster and the data within that cluster must be minimized [24, 25]. The objective function of k-means is written as:

$$J = \sum_{j=1}^{k} \sum_{x_i \in C_j} |x_i - \mu_j|^2 \left\| x_i - \mu_j \right\|^2 \qquad (1)$$

where i iterates over the data points, j iterates over the clusters, x_i is a data point, and μ_j is the centroid of the j-th cluster. The $|x_i - \mu_j|$ represents the Euclidean distance between a data point and the centroid. k is number of clusters.

c. Combined algorithm to obtain order of operation

The combined algorithm is utilized to send the commands the cobot to decide the order of operation for picking and placing objects, streamlining its manipulation and placement tasks. Combining image segmentation and the k-means algorithm is essential to indicate precise object localization. First, the image segmentation algorithm identifies potential objects

or regions of interest in the scene. Then, the k-means algorithm refines this localization by grouping together pixels with similar characteristics and indicating the objects' location. Snippets of pictures are used in the k-means algorithm for segmentation to better highlight the features of the object by separating distinct clusters representing different features within the image frame. The proposed algorithm is designed to impose fewer restrictions on the color segmentation threshold. K-means clustering is less affected by specific color values, as it focuses on overall color distribution. Combining these two algorithms improves object segmentation accuracy, mainly when color segmentation falls short.

Finally, the L^2 or Euclidean norm is employed to measure the distance between the center of the robot gripper and the centroid of each cluster. The process determines the object that has the minimum norm based on the picking location and the gripper location. This prioritization of sequence allows the cobot to minimize travel time by optimizing the path to be the shortest distance of operation. This approach aims to improve the accuracy and reliability of object localization significantly, making subsequent tasks like object recognition, tracking, and pick-and-place operations much more efficient. The order of pick-and-place operations and coordinate and pose estimations are then transmitted to the cobot software using socket communication.
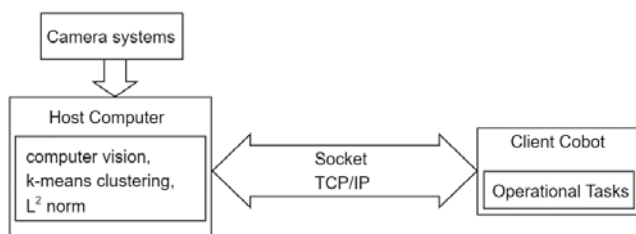

Figure 3 TCP/IP socket communication between host computer and client cobot (adapted from [26, 27]).

d. Socket communication to cobot

The communication process starts with establishing TCP/IP as a communication channel to transmit data between the host computer and the cobot, as illustrated in Figure 3, through a Local Area Network (LAN) to ensure the integrity and security of the data transmission. Specifically, TCP/IP socket communication is chosen due to its established reliability and broad compatibility across diverse devices [15, 26, 27]. The host is responsible for creating an endpoint that clients can connect to while the client component initiates the connection to the server. The TCP/IP socket connection facilitates the data exchange and instructions between the server computer and the

client cobot. The server processes visual information, generates commands, and transmits them to the client cobot, RobotStudio, enabling the cobot to execute tasks based on the computer vision analysis results obtained from the server.

The main objective of this communication setup is to enable the transfer of command information from the server computer, where computer vision and pick-place operation tasks are executed, to the cobot client for subsequent execution. Socket communication was selected as the communication mechanism in this study to facilitate information exchange between the host computer and the client IP ports. The client-server setup distinguishes a clear division of responsibilities: the client, or host computer in this case, initiates communication tasks and sends data, while the server, represented by the cobot, awaits incoming connections and processes the requests it receives.

The host computer initializes a socket communication to transmit the data in a binary socket package, including the location coordinates to perform pick place, pose, and object orientation to the Robot Studio. The send() and recv() functions transmit and receive data between devices. The Robot Studio, utilizing the RAPID programming language designed for ABB industrial robots and cobots, receives and interprets the control data, facilitating the command and regulation of cobots' positional adjustments and operation. The cobot then sends the signal back once the data is interpreted and performed as the data is sent accordingly. This coordinated control framework facilitates the cobot to navigate precisely to the specified location and execute the requisite actions to grasp the targeted object successfully.

e. High-level controller to execute pick-place operations and cobot kinematics.

To perform precise and accurate manipulation of the designated object, the high-level controller within a cobot framework functions as the processing task. It receives and interprets commands from the host via TCP/IP. These commands serve as precise target coordinates within the operational workspace of the cobot. The high-level controller's primary responsibility entails the formulation and execution of a trajectory plan constrained by kinematic limitations and spatial considerations. The trajectory planning focuses on devising efficient and obstacle-avoidant trajectories for the end-effectors of the cobots, enabling it to reach specified target positions within its workspace. In low-level operation, inverse kinematics entails the mathematical computation of joint angles required to position the end-effector of the cobot precisely at a designated location and orientation. It serves as the

connection between high-level task objectives and the joint space of the cobot, facilitating precise control of its movements. Subsequently, the controller activates the end-effector system to complete the pick-place operations.

During this stage, the controller monitors sensory feedback, particularly force-related data, to ensure objects' secure and accurate manipulation. In addition, collision detection is pivotal in ensuring safety by continuously monitoring the environment, identifying potential collisions with obstacles or other objects, and adjusting the trajectory or stopping its motion to prevent accidents and equipment damage. After a sequence of pick-place operations is completed, the information is sent back to the host and waits for the subsequent tasks.

The proposed methodology of this study is summarized as follows:

1. Obtain camera frame and perform preprocessing.
2. Perform image segmentation, which includes:
   a. Color thresholding, clustering of contours using a geometrical approach.
   b. K-means clustering based on a.
   c. combining a and b to identify each cluster.
3. Determine the order of pick-place operations of the cluster based on L^2 norm.
4. Transmit the localized data to the cobot to perform pick-place operations.
5. Execute pick-place operations and wait for confirmation of the operation from the cobot before repeating the process from step 1.

RESULTS AND DISCUSSIONS

This study randomly positions various objects with different colors (blue, grey, red, black) and shapes (stars, rectangles, cylinders, spheres, hexagons) within the workspace. This study specifically focuses on demonstrating the accuracy of identifying red spherical and rectangle objects to assess the proposed algorithm. The host computer, equipped with a proposed algorithm, successfully determines the correct positions of the indicated objects and can locate the closest one concerning the location of the pneumatic suction. A validation process is conducted to evaluate the precision of the pick-and-place operations by assessing the performance of picking up the designated red spheres. A total of 500 pick-and-place operations with a speed of 100 mm/s are performed, and each operation is categorized as either a correct or incorrect pick-up. The computer vision algorithm is initially applied

without k-means clustering, resulting in an observed accuracy of 87.4%.

After that, the proposed algorithm is implemented to detect the positions of the targeted red spheres during the validation procedure. Changes have significantly influenced the system's accuracy in lighting conditions and pick-place operating speed. Additionally, through further analysis, the sensitivity of the proposed algorithm can be fine-tuned by adjusting the threshold of location information within each frame window of capture. In this study, the algorithm was applied to every 15 consecutive frames from the camera to identify the optimal location of pick-and-place operations, resulting in an average response time of 0.52 ± 0.1 seconds for each pick-place operation. The cobot successfully executes the pick-and-place tasks with high accuracy, picking up the red spheres based on the identified coordinates and achieving an accuracy rate of 98.2% (See Figure 4). Image segmentation and clustering can accurately identify the number and location of clusters. The proposed algorithm performs better than the one without incorporating k-means clustering. The pick-place operation is illustrated in Figure 5. All the errors were associated with the proposed localized algorithm, which sometimes could not identify the objects from the captured images.

(a) (b)
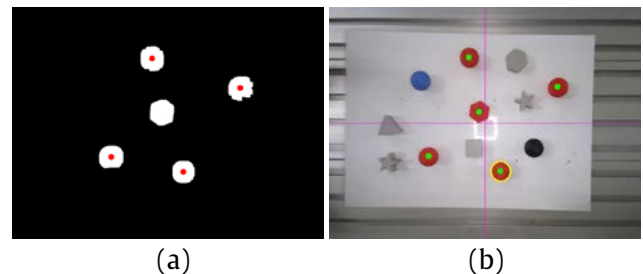
Figure 4 A snippet frame from the algorithm (a) after image segmentation and clustering of k-means algorithm and (b) resulting location of the picking operation.
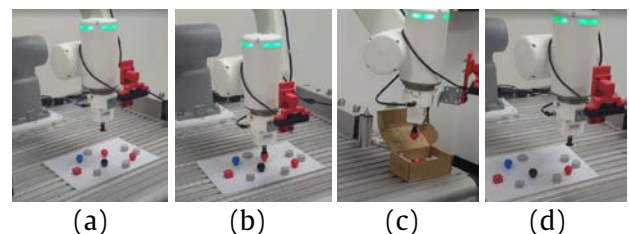

(a) (b) (c) (d)

Figure 5 A pick-place operation process (a,b,c,d) with pneumatic suction on specified objects of interest.

Variations in lighting conditions, occlusions, or challenging shapes may also have contributed to this source of error. In conditions with reduced

lighting, specifically at 1/3 of the standard lighting power, the accuracy of the pick-place operation is reduced to 67.1%. The primary factor contributing to the reduced accuracy is the inaccuracy of the color segmentation, accounting for 35.2% of the errors. Under diminished lighting conditions, the pick-and-place operation struggled to accurately identify the correct color range, leading to a decline in overall performance. Despite this limitation, the k-means clustering portion of the algorithm proved to be extremely helpful in object localization, enabling the cobot to successfully grasp objects even though they may possess the incorrect color or shape from error in segmentation. Another error occurs when the operating speed of the cobot is increased. The average response time in this study can be reduced through further optimization of the framework, thereby mitigating errors at higher jogging speeds of the cobot arms.

Another study involves object detection and pose estimation used along with machine vision to extract relevant information, such as key points for the end effector to grasp the specific part of the object precisely. Here, the pick-place operation of the rectangular object with a mechanical gripper is demonstrated. Once the cobot receives the coordinate data and performs inverse kinematics of the joint angles, the resulting angle of the object pose is sent to the cobot. The rotation of the mechanical gripper is performed to precisely place the cobot on the specific location and orientations concerning the workpiece. This demonstration is performed with the pick-place operations of the rectangular object, as seen in Figure 6 (a). The accuracy of this study is found to be 94% from a total of 200 operations at a speed of 100 mm/s, slightly lower than the study without pose estimation. This application creates a framework for precise object detection, which is crucial in applications like manufacturing and automation. Further applications of this study can be applied to critical points and image localization across a broad spectrum of industries. For instance, object detection instead of image segmentation can be computationally intensive to obtain the preliminary position of the objects of interest. K-means clustering is then applied to the image frame to obtain a more refined feature and segment the object boundaries for the pick-place operations. In this preliminary study, it is found that using You Only Look Once (YOLO) v8 [28], which is a well-known efficient convolutional neural net object detection along with k-means clustering of the image frame, could be used to obtain the exact position and pose of the object of interest for grasping accordingly. Figure

6 (b) shows that the proposed implementation starts with object detection to identify the local coordinates of the object of interest. The algorithm is then passed on to the k-means clustering, where the segmentation occurs, resulting in feature extraction and pose estimation for pick-place operations.
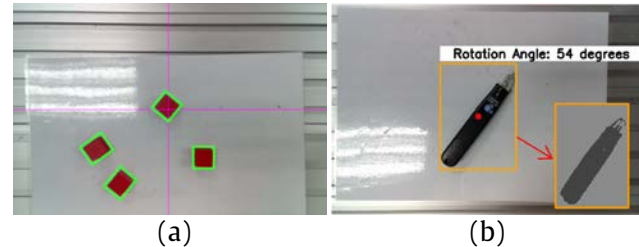
Figure 6 A snippet frame from the algorithm with pose estimation for the mechanical gripper.

CONCLUSIONS

This study proposes an approach to pick-and-place operations using computer vision. Integrating the computer vision algorithm allows the cobot to perceive and understand its surroundings by extracting relevant visual information. Utilizing the k-means clustering algorithm complements the computer vision component by offering a structured depiction of the localized objects, which are fundamental for accurate pick-and-place operations. The host computer then establishes a TCP/IP communication channel and transmits data to a cobot through a socket connection, enabling real-time command data exchange. The experimental results demonstrate the effectiveness of this integration, showcasing the enhanced adaptability and efficiency of pick-and-place operations in cobots. This research performs pick-and-place operations with 98.2% accuracy, achieving an average response time of 0.52 ± 0.1 seconds, compared to the original algorithm of 87.4% accuracy. Further study that includes pose estimation in pick-and-place operations demonstrates 94% accuracy. The study emphasizes the viability of employing a k-means algorithm in addition to image segmentation to execute pick-and-place operations by utilizing socket communication, enabling seamless data transfer between the cobot and the software, thereby enhancing overall efficiency.

ACKNOWLEDGEMENTS

REFERENCES

1. Preuveneers D, Ilie-Zudor E. The intelligent industry of the future: A survey on emerging trends,

research challenges and opportunities in Industry 4.0. J Amb Intel Smart En. 2017;9(3):287-98.

2. Kadir BA, Broberg O, Souza da Conceição C. Designing human-robot collaborations in industry 4.0: explorative case studies. In: *DS* 92: Proceedings of the DESIGN 2018 15th International Design Conference. 2018 May 21-24; Dubrovnik, Croatia. Dubrovnik: Design Society; 2018. p. 601-10.

3. Krüger M, Wiebel CB, Wersing H. From Tools Towards Cooperative Assistants. In: Proceedings of the 5th International Conference on Human Agent Interaction; 2017 Oct 17-20; Bielefeld, Germany. ACM; 2017. p. 287-94.

4. Li A, Gurocak H. Modified Bug Algorithm with Proximity Sensors to Reduce Human-Cobot Collisions. In: 2023 9th International Conference on Automation, Robotics and Applications (ICARA). 2023 Feb 10-12; Abu Dhabi, United Arab Emirates. Abu Dhabi: NYU Abu Dhabi; 2023. p. 80-5.

5. Syyrilä T. Development of a Collaborative Robot Manufacturing Workstation. [Master's Thesis]. Mechatronic System Design: Lahti University of Technology LUT; 2022.

6. Zhu Z, Hu H. Robot learning from demonstration in robotic assembly: A survey. Robotics. 2018; 7(2):17.

7. Peternel L, Petrič T, Babič J. Robotic assembly solution by human-in-the-loop teaching method based on real-time stiffness modulation. Autonomous Robots. 2018;42:1-17.

8. Borboni A, Reddy KVV, Elamvazuthi I, AL-Quraishi MS, Natarajan E, Azhar Ali SS. The expanding role of artificial intelligence in collaborative robots for industrial applications: A systematic review of recent works. Machines. 2023;11:111.

9. Biggs G, MacDonald B. A survey of robot programming systems. In: Proceedings of the Australasian conference on robotics and automation. 2003. p. 1-3.

10. Hughes C, Hughes T. Robot programming: a guide to controlling autonomous robots. Vol. 1. Indianapolis, Indiana:Que; 2016.

11. Rossano GF, Martínez C, Hedelind M, Murphy S, Fuhlbrigge T. Easy robot programming concepts: An industrial perspective. In: 2013 IEEE International Conference on Automation Science and Engineering (CASE). 2013 Aug 17-20; Wisconsin, USA. IEEE; 2013. p. 1119-26.

12. Pedersen MR, Nalpantidis L, Andersen RS, Schou C, Bøgh S, Krüger V, et al. Robot skills for manufacturing: From concept to industrial deployment. Robotics and Computer-Integrated Manufacturing. 2016;37:282-91.

13. Manoharan M, Thilak KSS, Kumaraguru S. Collaborative motion synchronization for affordable open-source cobots. In: 2022 IEEE 6th Conference on Information and Communication Technology (CICT); 2022 Nov 18-20; Gwalior, India. IEEE; 2022. p.1-5.

14. Iriondo A, Lazkano E, Susperregi L, Urain J, Fernandez A, Molina J. Pick and place operations in logistics using a mobile manipulator controlled with deep reinforcement learning. Appl Sci. 2019; 9(2):348.

15. Andhare P, Rawat S. Pick and place industrial robot controller with computer vision. In: 2016 International Conference on Computing Communication Control and automation (ICCUBEA). 2016 Aug 12-13; Pune, India. IEEE; 2016. p. 1-4.

16. Migimatsu T, Bohg J. Object-centric task and motion planning in dynamic environments. IEEE Robotics and Automation Letters. 2020;5:844-51.

17. Stulp F, Fedrizzi A, Beetz M. Learning and performing place-based mobile manipulation. In: 2009 IEEE 8th International Conference on Development and Learning; 2009 Jun 5-7; Shanghai, China. IEEE; 2009. p. 1-7.

18. Soltan S, Oleinikov A, Demirci MF, Shintemirov A. Deep learning-based object classification and position estimation pipeline for potential use in robotized pick-and-place operations. Robotics. 2020;9(3):63.

19. Kumar R, Kumar S, Lal S, Chand P. Object Detection and Recognition for a Pick and Place Robot. In: Asia-Pacific World Congress on Computer Science and Engineering; 2014 Nov 4-5; Nadi, Fiji. IEEE; 2015.

20. Lobbezoo A, Qian Y, Kwon HJ. Reinforcement learning for pick and place operations in robotics: A survey. Robotics. 2021;10(3):105.

21. Zhou W, Meng F, Li K. A cherry tomato classification-picking robot based on the K-means algorithm. J Phys: Conf Ser. 2020;1651:012126.

22. Anggi Maharani D, Fakhrurroja H, Riyanto R, Machbub C. Hand gesture recognition using K-means clustering and Support Vector Machine. In: 2018 IEEE Symposium on Computer Applications & Industrial Electronics (ISCAIE); 2018 Apr 28-29; Penang, Malaysia. IEEE; 2018. p. 1-6.

23. Wakayama T, Garcia Ricardez GA, Hafi LE, Takamatsu J. 6D-Pose Estimation for Manipulation in Retail Robotics using the Inference-embedded

OAK-D Camera. In: 2022 IEEE/SICE International Symposium on System Integration (SII). 2022 Jan 9-12; Narvik, Norway. IEEE; 2022. p. 1046-51.

24. Abernathy A, Celebi ME. The incremental online k-means clustering algorithm and its application to color quantization. Expert Systems with Applications. 2022;207:117927.

25. Ezugwu AE, Ikotun AM, Oyelade OO, Abualigah L, Agushaka JO, Eke CI, et al. A comprehensive survey of clustering algorithms: State-of-the-art machine learning applications, taxonomy, challenges, and future research prospects. Engineering Applications of Artificial Intelligence. 2022;110: 104743.

26. Hui-ping L, Dai-min C, Miao Y. Communication of multi-robot system on the TCP/IP. In: 2011 International Conference on Mechatronic Science, Electric Engineering and Computer (MEC). 2011 Aug 19-22; Jilin, China. IEEE; 2011. p. 1432-35.

27. Shin S, Yoon D, Song H, Kim B, Han J. Communication system of a segmented rescue robot utilizing socket programming and ROS. In: 2017 14th International Conference on Ubiquitous Robots and Ambient Intelligence (URAI). 2017 Jun 28-Jul 01; Jeju, Korea (South). IEEE; 2017. p. 565-9.

28. Jocher G, Chaurasia A, Qiu J. YOLO by Ultralytics (Version 8.0.0) [Computer software] [Internet]. GitHub, Inc, 2023. [cited 2023 Sep 10]. Available From: https://github.com/ultralytics/ultralytics/blob/main/CITATION.cff

Improvement of heat-sealing strength of chitosan-based composite films and product costs analysis in the production process

Yuthanarong Jongjun[1], Peema Pornprasert[3] and Sarinya Prateepchanachai[2*]

[1]Department of Industrial Technology, Faculty of Industrial Technology, Rajabhat Rajanagarindra University, Chachoengsao 24000, THAILAND

[2]Department of Industrial Management Engineering, Faculty of Industrial Technology, Rajabhat Rajanagarindra University, Chachoengsao 24000, THAILAND

[3]Department of Logistics Management, Faculty of Industrial Technology, Ubon Ratchatani Rajabhat University, Ubon Ratchatani 34000, THAILAND

[*]Corresponding author: sarinya@techno.rru.ac.th

ABSTRACT

The primary objective of this study was to enhance the heat-sealing strength of composite films made from chitosan and analyze the associated product costs. The approach adopted involved formulating chitosan-based composite films by incorporating gelatin and green seaweed extract. This strategic combination resulted in a notable improvement in heat-sealing strength. The ensuing attributes underwent meticulous examination, encompassing seal strength, FTIR spectroscopy, FE-SEM surface morphology analysis, and DSC thermal properties determination. Data analysis was rigorously conducted using the SPSS program, with outcomes presented as mean values accompanied by standard deviations. Disparities were discerned at a 95% confidence level, ensuring statistical robustness. The findings unveiled that the incorporation of 10% gelatin and 1% green seaweed extract substantially enhanced the seal strength of the chitosan-based composite films. Notably, the introduction of green seaweed extracts disrupted interactions between chitosan's structure and various molecular vibrations. This disruption, coupled with increased ionic interactions and hydrogen bonding, led to improved molecular interdiffusion, ultimately resulting in modified heat sealability. The study identified the optimized conditions as 10% gelatin and 1% green seaweed extract concentrations, which produced the highest seal strength at 19.4 N/m. Further evidence from scanning electron microscopy demonstrated improved interfacial adhesion, attributed to the adjusted surface morphology. The film surface did not contain small scattered particles and presented a smooth phase. This suggests that the chitosan-based composite achieved good interfacial adhesion between the two components in these films. As an essential aspect for practical application, the total production cost of the films was determined to be 606.84 baht. This information renders the data collection from the study valuable for companies seeking to enhance production efficiency and overall profitability.

Keywords: Chitosan, Composite films, Product costs, Seal strength, Thermal analysis

INTRODUCTION

Polymeric biomaterials are one of the cornerstones of biomedical engineering and across various scientific disciplines. Many of these polymers, including chitosan, are employed as viable replacements for synthetic polymers when compared to other biomaterials such as polysaccharides, lipids, and proteins. They are used to produce edible films due to their easy biodegradability, abundance, and sustainability. Chitosan, known for its high potential in terms of non-toxicity, biodegradability, and biocompatibility, possesses excellent characteristics for film formation and stability. These qualities make chitosan an attractive material for food packaging [1]. Chitosan,

primarily derived from the exoskeletons of crustaceans, is the second most prevalent polysaccharide in nature and contains inherent bioactive qualities, such as antibacterial and antioxidant activities. These attributes are crucial for developing active food packaging materials [2, 3]. On the other hand, despite chitosan's immense potential, its lack of heat sealability limits its application as a packaging material, requiring its combination with a thermoplastic polymer [4-7]. Creating a chitosan-based polymer by combining a suitable co-polymer with chitosan is an effective choice to improve thermal sealing properties. This process entails bonding two layers of films by pressing them between two heated plates for a specified duration. Several parameters,

including thickness, composition, molecular structure of the surface and the film's evaporation temperature are crucial factors influencing heat sealability. The ultimate seal strength is also impacted by the seal treatment circumstances, such as jaw pressure and dwell duration, serving as indicators of seal quality [8]. Blending chitosan powder with a copolymer offers a simple and cost-effective method to enhance the heat-sealing capabilities of films produced by solvent casting. However, the impact of different chitosan and copolymer ratios on the heat sealability of blended films remains unknown.

Recently, one possible method for overcoming the limitation of heat sealability is to modify the surface chemistry and molecular structure of chitosan molecules. Prateepchanachai et al. [7], previously employed an approach using glycerol and gelatin as copolymers to modify the surface for adhesive bonding of chitosan-based films. This involved incorporating both glycerol and gelatin into the film-forming solution preparation process. A solution consisting of 25% (w/w) glycerol and 10% (w/v) gelatin was utilized to create a film with superior heat-sealing properties compared to a chitosan solution. This film demonstrated enhanced sealability attributed to increased hydrogen bonding between the chains, facilitating molecular interdiffusion, thereby improving melting and sealing behavior.

An intriguing avenue to achieve the aforementioned goal involves the utilization of phenolic chemicals derived from plant extracts to facilitate uniform cross-linking of gelatin into polymeric chains. This process aids in controlling the functional properties in composite films. During heat sealing, gelatin promotes molecular inter-diffusion, stabilizing hydrogen and covalent bonds within the base polymer and resulting in enhanced sealability of the films. Additionally, gelatin contributes to the formation of thermo-reversible gels, which, in turn, assist in the creation of sealed joints [9]. The green seaweed extract emerges as a promising renewable resource in the marine environment, garnering significant interest and attention in energy, food, and tissue engineering applications. This is attributed to the highly exploitable, easily accessible, and cost-effective source of polysaccharides it provides. In previous studies, Prateepchanachai et al. [8], utilized green seaweed extracts at concentrations of 1% (v/v) or higher to prepare chitosan-based films. Furthermore, studies did not report any improvement in the sealing qualities of the films when red seaweed extract and brown seaweed extract were added at concentrations ranging from 0 to 15% (v/v), in contrast to the results observed with the addition of green seaweed extract. As a result, the properties of a functional group in the gelatin molecule were enhanced through the addition of seaweed. This discovery suggests that green seaweed extract could serve as a novel cross-linker in gelatin molecules for film preparation, providing a viable means to achieve this objective. Despite some

research into the combined impacts of gelatin and seaweed on the thermal properties of biopolymers, no studies have been conducted to manufacture and test chitosan-based composite films incorporating gelatin and green seaweed, along with examining the drying process of the resultant film-forming solutions. To date, no study has reported on the influence of modifying chitosan-based composites in the preparation of film solutions on surface microstructure properties. Additionally, there is a lack of research examining the adhesion of sealability, along with the calculation of product costs. This encompasses data collection on material costs, equipment costs, tooling costs, labor costs, energy costs, and overhead costs of the chitosan film production process. These represent the initial research studies on product cost calculation, a crucial metric for identifying and measuring the productivity and profitability of industries.

The objective of this research was to enhance the combined impact of gelatin and green seaweed extract in creating a composite chitosan-based film. The films underwent Fourier transform infrared spectroscopy (FTIR) analysis to examine their surface morphologies, which were further scrutinized by Field Emission Scanning Electron Microscopy (FE-SEM) for excellent resolution. Additionally, the thermal properties of the films were determined using Differential Scanning Calorimetry (DSC), elucidating the mechanisms contributing to their heat-sealing characteristics. The analysis of product costs was also conducted, providing valuable insights for manufacturers to determine the selling price.

MATERIALS AND METHODS

1. Materials

S.K. Profishery Co., Ltd. provided chitosan powder with a molecular weight of 900 kDa and a deacetylation degree of 90.2%. (Samut Sakhon, Thailand). Ruam Chemical 1986 Co., Ltd. provided analytical quality glacial acetic acid and green seaweed extract (Bangkok, Thailand). Top supermarkets sell porcine gelatin powder (Chachoengsao, Thailand). Tropicalife Co., Ltd. supplied the deionized water (Bangkok, Thailand)

2. Creating film-forming solutions

The techniques developed by Prateepchanachai et al. [8], were employed with appropriate modifications, to create a chitosan film-forming solution. In figure 1.

The first step involved dissolving 1.5% (w/v) chitosan powder in a 1% (v/v) acetic acid solution for 6 hours at room temperature, utilizing a magnetic stirrer machine (Framo Gerätetechnik, model M21/1, Eisenbach, Germany). The chemical reaction between chitosan and acetic acid in the aqueous solution, illustrating the film preparation process, is depicted in figure 2.

Glycerol was then added to the solution at a concentration of 25% (w/w chitosan). Following that, a 10% (w/v) gelatin solution was prepared by dissolving 10 g of gelatin powder in 100 mL of deionized water, achieved by heating at 70 °C for 30 minutes. After preparing the chitosan-glycerol mixture, the gelatin solution was added at concentrations of either 0% or 10% (w/v) to obtain the chitosan-glycerol-gelatin film-forming solutions. Green seaweed extract was then added at either 0 or 1% (v/v), which was the result of preliminary experiments with adding green seaweed extract. Concentrations greater than 1% (v/v) produced films with poorer heat sealing than the target value of chitosan control film. After another hour of stirring at 500 rpm at room temperature, the solution was centrifuged at 19,414 g for 15 minutes to remove undissolved contaminants before hot air drying using a chilled centrifuge equipment.
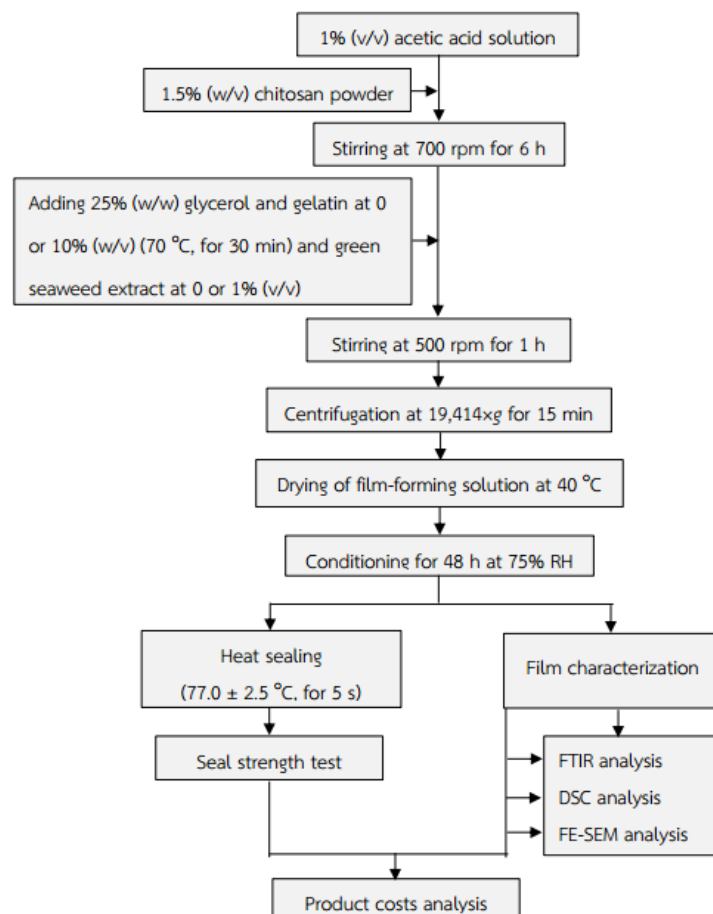
Figure 1 Designing overall experimental steps.
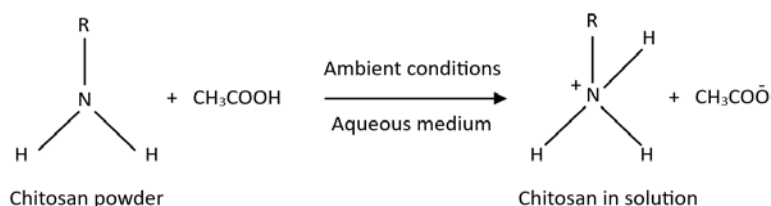
Figure 2 Illustrates the chemical reaction between chitosan and acetic acid in an aqueous solution, showcasing the film preparation process.

3. Preparation of chitosan films

To cast a film, each prepared film-forming solution (16 g) was applied onto an acrylic plate with dimensions of 13 × 10 cm. Drying was conducted at a hot air temperature of 40 °C and an air velocity of 0.25 m/s until the film reached a moisture content of around 14% (dry basis). Following this, the film was stored in a desiccator containing a saturated solution of sodium chloride, creating a relative humidity of 75%, for at least 48 hours before undergoing further characterization (This relative humidity level represents the average conditions in Thailand).

4. Characterization of chitosan film

4.1 Seal strength evaluation
As depicted in figure 3, the film sample was cut into a 10 × 2.5 cm strip, placed on top of another

10×2.5 cm film strip, and heat-sealed with a 1 cm width at 77.0 ± 2.5 °C. This temperature represents the upper limit of the heat-sealing capability of the automatic sealing machine, which does not allow for adjustments to different temperatures. The sealing was performed for 5 minutes using an automatic heat sealer (AUTOMATIC EXTERNAL PACKING MACHINE, DZ-400T, Bangkok, Thailand). The heat-sealed film's sealing strength was assessed using an analysis comparable to a texture analyzer and the ASTM Standard Test Method F88 [9], with minor adjustments. The texture analyzer clamped each leg of the sealed film and suspended it perpendicular to the test direction. The seal strength in N/m is indicated as the force required for sealing damage, measured as the needed maximum forces:

$$\text{Seal strength} = \text{Peak force/Film width} \qquad (1)$$

(a)   (b)
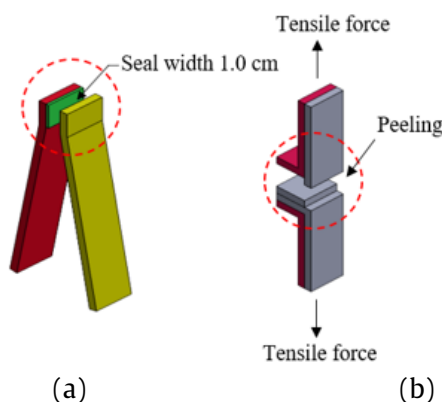
Figure 3 Simplified depiction of test specimen measurements and directions for peel test (a) film sample with bar sealing with 1.0 cm width (b) direction of pull is 90° to the seal in peeling test.

4.2 Determination of film FTIR Spectra

A film sample was spectroscopically examined using FTIR (ATR-FTIR) with modifications based on the methods of Prateepchanachai et al. [8], employing an FTIR spectrometer (Nicolet iS50, Thermo Scientific, Waltham, USA). The FTIR spectra were studied using a DTGS detector with a resolution of 4 cm^{-1} and a wavelength range of 4,000 to 400 cm^{-1}. The FTIR spectra had a wavelength accuracy of 0.1 cm^{-1} at 1,600 cm^{-1}.

4.3 Field emission scanning electron microscope (FE-SEM) analysis

The surface morphology of the microstructure films was assessed using a field emission scanning electron microscope (FE-SEM) (JEOL, JSM7800F model, Japan) in conjunction with the PCSEM software, employing an accelerating voltage of 15 kV. The samples were coated using a sputtering technique (QUORUM, Q150R ES model, UK) with a layer of gold (Au). The sputter conditions included a sputter current of 23 mA and a sputter time of 45 seconds.

4.4 Determination of thermal properties by differential scanning calorimetry (DSC)

Differential Scanning Calorimetry (DSC) (DSC 3+, Mettler Toledo model, Switzerland) was utilized to assess the thermal characteristics of composite chitosan films. Films (1 mg) were placed in an aluminum pan containing 20 μL of light. The nitrogen flux was maintained at 50 milliliters per minute. The analysis involved heating the films from 20 to 130 °C at a rate of 10 °C/min, followed by a 5-minute isotherm. Subsequently, the films were cooled from 130 to 5 °C at a rate of 20 °C/min, followed by another 5-minute isotherm in nitrogen. Finally, the glass transition temperatures were determined by heating the films to 300 °C at a rate of 10 °C/min (T_g) [8].

5. Statistical investigation

All data were analyzed using the SPSS® program (version 17; SPSS Inc., Chicago, IL) and are presented as mean values with standard deviations. To identify differences between mean values at a 95% confidence level, Duncan's novel multiple range tests were employed. Every experiment was conducted in triplicate.
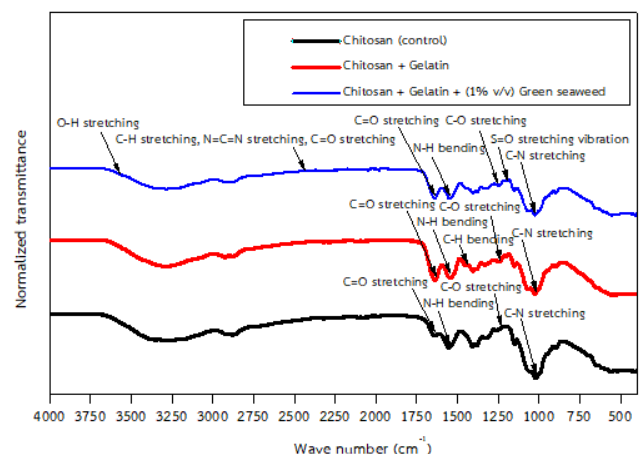
RESULTS AND DISCUSSIONS

1. FTIR spectra

Figure 4 FTIR spectra of film samples prepared at various concentrations of 10% (w/v) gelatin and 1% (v/v) green seaweed.
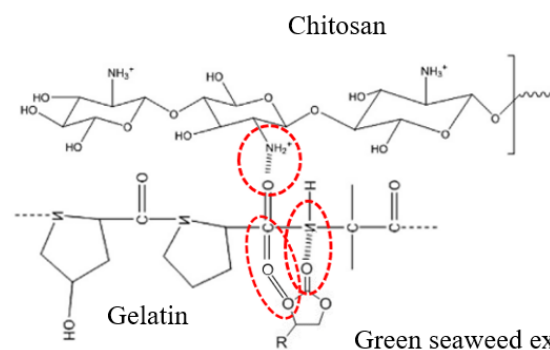

Figure 5 A tendency diagrammatic representation of intermolecular between chitosan, gelatin, and green seaweed molecule.

FTIR spectroscopy was employed for the functional groups analysis of the chitosan-based composite film, as illustrated in figure 4. The addition of gelatin and green seaweed to the film resulted in increased peak intensities at 4,000-3,450 cm^{-1} (O-H stretching), indicating intermolecular interactions between amino acids of gelatin and phenolic compounds in green seaweed. Hydrogen bonds formed to engage with the chitosan structure. Additionally, higher peak absorptions were observed in the wavenumber regions of 3,130-1,700 cm^{-1}, associated with aldehyde (C-H stretching), carbodiimide (N=C=N stretching), and carboxylic acid (C=O stretching). These peaks indicated electrostatic interactions between gelatin peptide hydrogen bonds and green seaweed phenolic compounds, enhancing intermolecular interactions within the chitosan chains. This increased adhesion strength between the films, influencing the seal strength of the films. A schematic representation of the strong intermolecular interaction, mainly between chitosan, gelatin, and green seaweed extract composite film, is depicted in figure 5. Therefore, chitosan-based composite films were selected for this study due to their unique properties, versatility, and ability to interact with other components, aligning with the study's objectives of enhancing film properties and analyzing associated costs.

2. Heat seal strength

When sealing was conducted at a temperature significantly lower than the melting point of the sealant material, all samples failed in the peeling mode, as depicted in figure 3 (b). This outcome is anticipated since a decrease in the sealing strength of the composite film leads to the disentanglement of polymer molecules, resulting in the bond pulling apart.

Table 1 presents the maximum heat seal strength values for the film samples, calculated using equation 1. Films sealed at 77.0 ± 2.5 °C with a dwell length of 5 seconds exhibited peeling mode failure of the seal, indicating optimal seal strength. Sealing the control film proved challenging due to its rigid crystalline structure and the presence of strong intermolecular or intramolecular hydrogen bonding. The limited mobility of chitosan chains during thermal breakdown resulted in poor molecular penetration at the film surface and, consequently, poor sealability.

The addition of gelatin and green seaweed extract to the film-forming solution enhanced the film's seal strength. This enhancement is likely due to the ionic interaction and hydrogen bond between the -COOH groups of gelatin and the -NH$_2$ group of chitosan, leading to electrostatic interactions and intermolecular hydrogen bonds between opposite charges. This, in turn, enhanced molecular interdiffusion between chains. The addition of green seaweed extract resulted in the maximum seal strength at 19.4 ± 1.0 N/m. This could be attributed to the increased

repulsion force between gelatin and green seaweed molecules, leading to increased partial denaturation and crystallization. As a result, they transformed into a more orderly structure, reflecting the lower rigid structure of the film network, and increasing thermal stability.

The addition of green seaweed at a concentration of 1% (v/v) resulted in the highest sealing strength compared to the control film. However, further increases in green seaweed concentration (above 5% (v/v)) did not significantly increase the seal strength. This value is lower than the heat-sealed chitosan reported by Prateepchanachai et al. [7] due to the use of an impulse heat-sealing machine with a very high heat-sealing temperature. Therefore, in future research, experimental conditions should be set as close as possible to the previous study.

Table 1 Heat seal strength and glass transition temperature of different films.

Film type	Heat seal strength (N/m)	Glass transition temperature (°C)
Chitosan (control)	4.5±1.3^A	110.1±1.9^C
Chitosan + Gelatin	14.2±1.0^B	100.5±2.5^B
Chitosan + Gelatin + 1% (v/v) Green seaweed extract	19.4±1.0^C	94.8±1.4^A

3. Thermal characteristics

The Differential Scanning Calorimetry (DSC) technique investigated the thermal transition temperatures affecting the sealing temperatures of polymers. Table 1 also presents the glass transition temperatures (T_g) of chitosan-based composite films with gelatin and green seaweed extract. The chitosan film (control) exhibited the highest T_g value of 110.1 ± 1.9 °C due to the N-H bending and O-H stretching, leading to the development of intramolecular hydrogen bonding and constrained mobility of the chitosan chains. This behavior was reflected in the difficulty of adhesion and heat seal strength. The addition of gelatin and green seaweed resulted in the lowest T_g value at 94.8 ± 1.4 °C, which is lower than that of the control film. The decrease in T_g value may be attributed to the plasticizing effect of the composite chitosan film with gelatin and green seaweed, increasing the free volume and intermolecular distance in the films due to the repulsion force between the chitosan chains. This led to a reduction in the transition temperature of the resulting film. Therefore, the composite chitosan film with gelatin and green seaweed exhibited different thermal transition characteristics compared to the pure chitosan film.

Several studies assessing biopolymer films have utilized SEM to establish correlations between film attributes and morphological structures, as demonstrated in the research by Souza et al. (2010) [10] and Castello et al. [11]. Figure 6 presents the results of FE-SEM images comparing the chitosan

(control) film (figure 6a) with the combined addition of gelatin and 1% (v/v) green seaweed extract film (figure 6b). The FE-SEM images of the chitosan film exhibited a characteristic pattern on the film surface, appearing as a smooth phase with a nonporous, homogeneous, and continuous matrix displaying high structural integrity [12]. The surface was flat and compact, with extremely sparsely scattered tiny particles and no phase separation. The combined addition of gelatin with 1% (v/v) green seaweed extract significantly altered the chemical structure of the pure chitosan film, resulting in a more regular structure, which is likely reflected in the observed changes in the film's surface morphology. Notably, the film surface did not contain small scattered particles and presented a smooth phase. This suggests that the chitosan-based composite achieved good interfacial adhesion between the two components in these films.
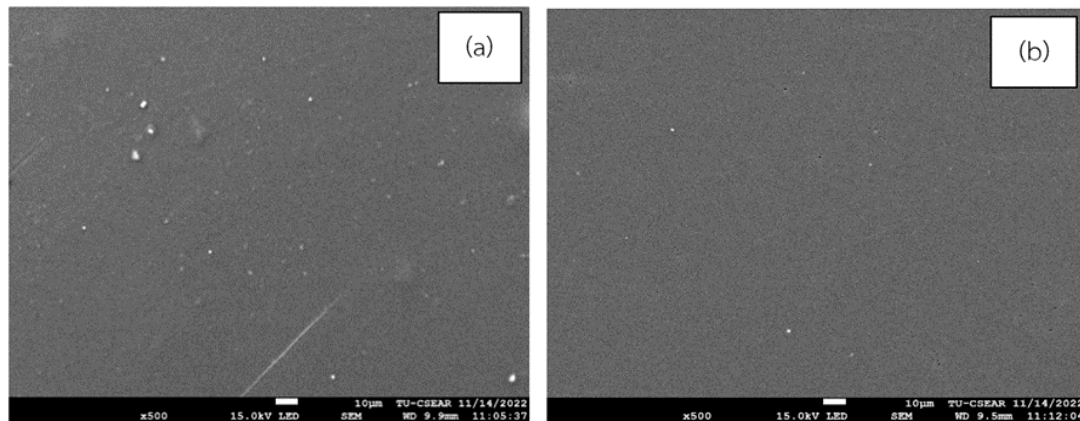

Figure 6 FE-SEM micrographs of difference films condition to (a) pure chitosan (regulate) film, and (b) combined addition of chitosan and gelatin with 1% (v/v) green seaweed extract film.

4. Product costs analysis

The product costs analysis pertains to the expenses incurred in creating packaging films intended for sale to customers. In industrial settings, the scale of production is akin to a system processing inputs to generate outputs, encompassing raw material costs, equipment costs, tooling costs, labor costs, energy costs, and overhead costs. To ascertain whether a firm is making a profit or incurring a loss, a thorough assessment of product costs or production expenses incurred throughout the manufacturing process is necessary, utilizing established accounting standards. The cost of goods becomes a primary reference point for determining the selling price of the final products [13].

Given that the film prepared from chitosan with gelatin and green seaweed extract exhibits superior heat-sealing properties compared to a pure chitosan solution, this research focuses on calculating costs under these conditions. The calculation of raw materials is defined by the amount of material utilized at the material's cost. Specifics regarding raw material usage during the production process in October 2022 are summarized in Table 2. The total raw material cost for using chitosan-based composite films in the production process is 15.40 baht/ml. Tooling costs amount to 80 baht/L. Direct labor costs involved in the production process are 400 baht/day. Total electricity costs are 92.09 baht/day. Total overhead costs cover all manufacturing expenses not included in direct materials and direct labor, calculated from actual costs incurred during a specific period, amounting to 19.35 baht/pcs. Equipment costs total 51,149 baht.

Table 2 Production cost of chitosan-based composite film.

Cost type	Quality (per unit)	Cost (baht/unit)
Raw material costs	Chitosan 1,800.00 baht/kg	0.027 baht/ml
	Green seaweed 2,369.00 baht /kg	2.37 baht/ml
	Glycerol 120.00 baht/kg	3.00 baht/ml
	Gelatin powder 930.00 baht/kg	1.00 baht/ ml
	acetic acid 89.00 baht/kg	9.00 baht/ml
	Total raw material costs	15.40 baht/ml
Tooling costs	Deionized water 80.00 baht/L	80.00 baht/L
Labor costs	Wage 0.83 baht/min	400.00 baht/day
Energy costs	Hot air oven 3,300.00 watts, 8 hrs.	89.69 baht/day
	Impulse heat sealer PS450 600 watts/hr.	2.40 baht/day
	Total energy costs	92.09 baht/day
Overhead costs	Grove 255.00 baht/100 pcs.	2.55 baht/pcs.
	Mask carbon 373.00 baht/50 pcs.	7.50 baht/pcs.
	Tissue paper 89.00 baht/6 pcs.	7.00 baht/pcs.
	Foil bag 115.00 baht/50 pcs.	2.30 baht/pcs.
	Total overhead costs	19.35 baht/pcs.
Total production cost (a)		606.84 baht
Number of films that produce (b)		7 pcs.
Production cost of films (13×10 cm) per package (a/b)		86.69 baht/pcs.
Equipment costs	Hot air oven 37,900.00 baht	
	Beaker glass 1,000 ml 1,430.00 baht	
	Spatula stainless 220.00 baht	
	Digital weighing 2,874.00 baht	
	Measuring pipette 340.00 baht	
	Pipette rubber 75.00 baht	
	Plate casting 10.00 baht/pcs.	
	Impulse heat sealer PS450 8,000.00 baht	
	Maintenance 300.00 baht/year	
	Total equipment costs	51,149.00 baht

Table 2 further illustrates that the total production cost during October 2022 is 606.84 baht. This indicates that the film, while demonstrating excellent heat-sealing properties, tends to be relatively expensive for packaging polymer use. Assuming the manufacturing is completed in one day, disregarding the presence of commodities in the process, and considering that 7 pcs of chitosan-based composite films can be produced, the production cost per film (with dimensions of 13 × 10 cm, suitable for packaging or wrapping) is calculated by dividing the total production cost by the number of films produced, resulting in 86.69 baht/pcs. Based on these findings, companies and researchers can utilize the data collection of total production cost components as a foundation for determining the cost of products sold and assessing profitabily.

CONCLUSION

The combined addition of 10% (w/v) gelatin and 1% (v/v) green seaweed extract significantly improved the seal strength of composite chitosan-based films. This enhancement was accompanied by a detailed product cost analysis. The introduction of green seaweed extract is believed to disrupt interactions within the chitosan structure. Consequently, the addition of green seaweed extract enhances the film's seal strength by increasing ionic interactions and hydrogen bonding between the -COOH groups of gelatin and the $-NH_2$ group of chitosan. This reaction leads to electrostatic interactions and intermolecular hydrogen bonds between opposite charges, ultimately improving molecular interdiffusion between the chains and modifying heat sealability. This improvement is further evidenced by a significant reduction in the glass transition temperature, lowered by 94.8 ± 1.4 °C compared to films made from pure chitosan. Optimal conditions were identified at a concentration of 10% (w/v) gelatin and 1% (v/v) green seaweed extract, resulting in the highest seal strength of 19.4 N/m. Surface inspection using FE-SEM revealed changes in the smooth surface morphology, indicating reasonably high interfacial adhesion between the two components. While the total production cost of the films amounted to 606.84 baht, this dataset offers valuable insights for companies engaged in the production of goods, potentially influencing overall profitability.

ACKNOWLEDGEMENT

REFERENCES

1. Agarwal C, Koczan Z, Borcsok Z, Halasz K, Pasztory Z. Valorization of Larix decidua Mill bark by functionalizing bioextract onto chitosan films for sustainable active food packaging. Carbohyd Polym. 2021;271:1-11.

2. Haghighi H, Licciardello F, Fava P, Siesler HW, Pulvirenti A. Recent advances on chitosan-based films for sustainable food packaging applications. Food Packaging and Shelf Life. 2020;6:1-16.

3. Wang W, Xue C, Mao X. Chitosan: Structural modification, biological activity and application. Int J Biol Macromol. 2020;164:4532-46.

4. Ren L, Yan X, Zhou J, Tong J, Su X. Influence of chitosan concentration on mechanical and barrier properties of corn starch/chitosan films. Int J Biol Macromol. 2017;105:1636-43.

5. Zheng K, Xiao S, Li W, Wang W, Chen H, Yang F, et al. Chitosan acorn starch-eugenol edible film: Physico-chemical, barrier, antimicrobial, antioxidant and structural properties. Int J Biol Macromol. 2019; 135:344-52.

6. Alves Z, Ferreira NM, Ferreira P, Nunes C. Design of heat sealable starch-chitosan bioplastics reinforced with reduced graphene oxide for active food packaging. Carbohyd Polym. 2022;291:1-11.

7. Prateepchanachai S, Thakhiew W, Devahastin S, Soponronnarit S. Improvement of mechanical and heat-sealing properties of edible chitosan films via addition of gelatin and CO_2 treatment of film-forming solutions. Int J Biol Macromol. 2019;131: 589-600.

8. Prateepchanachai S. Improvement of heat-sealing properties of composite chitosan films via the use of gelatin and green seaweed blends in film-forming solutions. UBU Engineering Journal. 2021;14(4): 150-60.

9. American society for testing and materials (ASTM). Standard test method for seal strength of flexible barrier materials (F88). Annual Book of ASTM Standards. Philadelphia PA; 2005.

10. Souza BWS, Cerqueira MA, Martins JT, Casariego A, Teixeira JA, Vicente AA. Influence of electric fields on the structure of chitosan edible coatings. Food Hydrocolloids. 2010;24:330-35.

11. Castello ME, Anbinder PS, Amalvy JI, Peruzzo PJ. Production and characterization of chitosan and glycerol-chitosan films. Materials Research Society. 2018;3:3601-10.

12. Tripathi S, Mehrotra GK, Dutta PK. Physicochemical and bioactivity of cross-linked chitosan-PVA film for food packaging applications. Int J Biol Macromol. 2009;45:372-76.

13. Putri RL. Analysis of production of calculations using process costing method in SULI TAFU factory. Jurnal Online Universitas 45 Surabaya [Internet]. 2017 [cited 2022 Dec 31]; 6-13. Available From: https://core.ac.uk/download/pdf/235584423.pdf.

Preparation of poly(methyl methacrylate)-zinc oxide hybrid nanoparticles via miniemulsion polymerization

Tanapak Metanawin[1], Maneerat Charoenchan[2] and Siripan Metanawin[2,3]*

[1]Department of Materials and Production Technology Engineering, Faculty of Engineering, King Mongkut's University of Technology North Bangkok, Bangkok 10800, THAILAND

[2]Department of Textile Engineering, Faculty of Engineering, Rajamangala University of Technology Thanyaburi, Pathum Thani 12120, THAILAND

[3]Materials Design and Development (AMDD) Research Unit, Faculty of Engineering, Rajamangala University of Technology Thanyaburi, Pathum Thani 12120, THAILAND

*Corresponding author: siripan.m@en.rmutt.ac.th

ABSTRACT

The encapsulation of zinc oxide (ZnO) nanoparticles with poly(methyl methacrylate) in the presence of triethylene glycol dimethacrylate (TEGDMA) as a crosslinking agent was synthesized by the miniemulsion polymerization technique. The ZnO as a catalyze was varied from 1 wt% - 7 wt%. Several techniques were used to analyze the PMMA/TEGDMA/ZnO hybrid. The morphology and particle size distribution of the PMMA hybrid was observed using a field emission scanning electron microscope (FE-SEM). The diameter of the PMMA/TEGDMA/ZnO hybrid was in the range of 57 nm to 115 nm. The morphology of the PMMA/ZnO hybrids was sphere-shaped with a narrow particle size distribution and no agglomeration of the hybrids occurred. The encapsulation and crystalline structure of the PMMA ZnO hybrid were determined using a high-resolution transmission electron microscope (HR-TEM). The HR-TEM image demonstrated that the ZnO was encapsulated in the PMMA hybrid. In addition, the high magnification of the TEM image demonstrated the lattice spacing of ZnO and the diffraction mode image presented the crystalline structure of ZnO. Therefore, the photocatalytic properties of the PMMA/ZnO hybrid were examined via the degradation of methylene blue (MB) solution under dark and UV-A irradiation. It was found that the photocatalytic activities of the PMMA/ZnO hybrid increased when the ZnO content increased up to 7 wt%. The maximum MB degradation for PMMA/TEGDMA/ZnO 7 wt% and PMMA/ZnO 7 wt% were 80.1 % and 77.6 %, respectively. Thus, the photocatalytic efficiency of the PMMA/ZnO increased in the presence of TEGDMA as a crosslinking agent.

Keywords: Hybrid, Miniemulsion polymerization, Titanium dioxide, Poly(methyl methacrylate)

INTRODUCTION

Hybrid materials have been widely studied because hybrid materials present the properties of both organic polymers and inorganic materials, with new properties [1, 2]. Hybrid materials comprise two or more materials on the molecular scale and nanoscale levels. The hybrid materials can design and synthesize novel materials in different techniques for sample use materials chemistry, inorganic chemistry, and polymer chemistry to make a new product such as electronic materials, efficient catalysts, magnetic materials, and optical material [1, 3, 4]. Various types of material combinations and synthesis strategies have been developed for the hybrid materials, using the sol-gel method, miniemulsion polymerization technique, or other solution processes [5-10].

Miniemulsion polymerization is a unique oil-in-water emulsion type with distinct advantages over conventional emulsion polymerization. Miniemulsion polymerization has several advantages: low reaction temperatures, high polymerization rate, high monomer conversion, and the ability to produce high molecular weight polymers [11-13]. Miniemulsion polymerization, consisting of tiny stable droplets within a size range of 50 nm to 500 nm, is usually prepared by shearing a mixture of monomer, surfactant, co-stabilizer, and initiator dispersed in an aqueous phase [9, 12, 14]. The most inorganic materials of photocatalysts and antibacterial are metal oxides such as zinc oxide (ZnO) and titanium dioxide (TiO_2) [15, 16]. However, zinc oxide (ZnO) is one of the most popular photocatalysts and antibacterial agents because of its low cost and good stability. It has been widely used in a variety of

applications in the environment, including cosmetics, pigment, and air purification systems [17-20].

Several studies have focused on investigating the antibacterial and photocatalytic properties of ZnO. In previous studies, the PS/TEGDMA/TiO$_2$ hybrid demonstrated that the TEGDMA enhanced the photocatalytic properties and stability of the PS hybrid. Up to date, there are only a few studies on the encapsulation of ZnO via miniemulsion polymerization [21]. Furthermore, there is no research on PMMA/ZnO hybrid with TEGDMA via miniemulsion polymerization. Therefore, in this study, we synthesized the PMMA/ZnO hybrid via miniemulsion polymerization, and TEGDMA was added to the system as a crosslinking agent. The photocatalytic performance and the morphology of the hybrid were also studied.

MATERIALS AND METHODS

Materials

MMA monomer (99%, Sigma-Aldrich) was purified by passthrough basic aluminum oxide prior to use. Zinc oxide (ZnO, 99%, 10-30 nm, US Research Nanomaterials), aluminum oxide (basic Al$_2$O$_3$, Sigma-Aldrich), hexadecane (HD, 99%, Sigma-Aldrich), sodium dodecyl sulfate (SDS, 99%, Sigma-Aldrich), potassium persulfate (KPS, 99%, Sigma-Aldrich), triethylene glycol dimethacrylate (TEGDMA, 95%, Sigma-Aldrich), and methylene blue (MB, >95%, Ajax Finechem) were used as received. Deionized water (DI water) was purified by ELGA LabWater model Micra.

Table 1 The experimental details of the syntheses of PMMA/ZnO and PMMA/TEGDMA/ZnO.

Sample name	TEGDMA (% wt)	ZnO (% wt)
PMMA	-	-
PMMA/ZnO 1%	-	1
PMMA/ZnO 3%	-	3
PMMA/ZnO 7%	-	7
PMMA/TEGDMA	0.2	-
PMMA/TEGDMA/ZnO 1%	0.2	1
PMMA/TEGDMA/ZnO 3%	0.2	3
PMMA/TEGDMA/ZnO 7%	0.2	7

Preparation of PMMA and PMMA/ZnO hybrid

In general, miniemulsion polymerization, 5.00 g of MMA, 0.20 g of hexadecane, and with/without 0.20 g of TEGDMA were mixed. 0.06 g of SDS was dissolved with 20.0 cm^3 of water in a flask. Then, the monomer mixture was added to the flask. It was stirred under nitrogen gas for 15 min. This flask was subjected

to ultrasound (130W and 60% amplitude) in an ice bath for 15 min to obtain miniemulsion. The reactor was heated to 70 °C and then, 0.083 g of KPS was added to the flask. After 4 h of reaction time, the miniemulsion was obtained by cooling it in an ice bath. The experimental details of the syntheses of PMMA/ZnO and PMMA/TEGDMA/ZnO using the miniemulsion technique are given in Table 1.

Characterization

The structural analysis of the PMMA hybrid was measured using a PerkinElmer Frontier instrument (USA) spectrometer. The IR spectra were scanned between 4000-400 cm^{-1}.

Field Emission Scanning Electron Microscope (FE-SEM)

The PMMA hybrid morphology was discovered using a JSM-7600F (Jeol, Japan). The particle size distribution (average particle size) was measured from 20 samples using ImageJ software version 1.53e with Java 1.8.0_172.

High-resolution Transmission Electron Microscope (TEM)

The morphology and crystalline structure of the PMMA hybrid were performed on JEM-3100F (Jeol, Japan) operated at 300 kV.

Photocatalytic activities

The photocatalytic activities were explored by detecting the degradation of MB under UV-A at 365 nm wavelength (TL-K 40W/10-R, Philips, The Netherlands). 1 mL of PMMA hybrids was placed in 10 ppm of MB. The light intensity was 6.0 mW/cm^2. The samples were used directly without purification. The MB degradation was measured at a wavelength range of 660 nm using an UltraScan Pro Color dual-beam spectrophotometer with a 512-element diode array (HunterLab, USA).

RESULTS AND DISCUSSION

Effect of ZnO on morphology and structure of PMMA hybrid

The PMMA/ZnO and PMMA/TEGDMA/ZnO hybrids were synthesized by miniemulsion polymerization in the presence of TEGDMA as a crosslinking agent. The PMMA polymer was employed as a shell, whereas the ZnO was encapsulated in the core of the hybrid. Figure 1 shows the FE-SEM images and particle size distribution of the PMMA/TEGDMA/ZnO with various ZnO from 0, 1, 3, and 7 wt%. The result shows that the average diameter of PMMA/TEGDMA without ZnO was 57 nm, as seen in figures 1a and 1b while PMMA/TEGDMA/ZnO

1 wt% was 71 nm which the particle size increased by 24 %, as presented in Figure 1c and 1d. As seen in Figure 1e and 1f, moreover, the particle size of PMMA/TEGDMA/ZnO 3 wt% was 87 nm which increased by 52%. Therefore, the addition of ZnO 7 wt% to the PMMA hybrid increased the particle size to the maximum of 115 nm which increased 221%, as presented in Figure 1g and 1h. Figures 1b, 1d, 1f, and 1h presented the narrow size distribution of PMMA/TEGDMA/ZnO with various ZnO. From SEM images, the miniemulsion polymerization method exhibited an excellent particle size distribution without aggregation of ZnO nanoparticles. The addition of TEGDMA increased the stability of the PMMA hybrid resulting in no particle breakdown [22, 23]. It was noticed that the particle size of the PMMA hybrids increased with the amount of ZnO. This particle size increased due to a rise in the contents of ZnO in the PMMA hybrid TiO_2 [24].
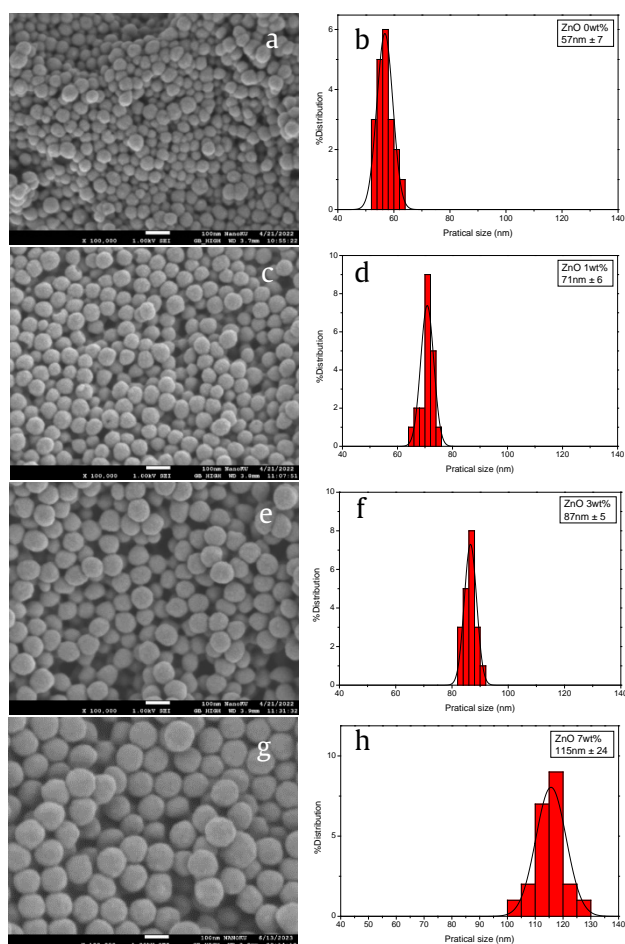

Figure 1 FE-SEM image of PMMA/TEGDMA/ZnO 0, 1, 3, and 7 wt% at 100,000x magnifications. The scale bar was 100 nm.

Effect of ZnO on the structure of PMMA hybrid

Figure 2 presented the HR-TEM image, lattice image, and diffraction pattern of the PMMA/TEGDMA/

ZnO 7wt%. Figure 2a demonstrates the encapsulation of ZnO in the PMMA/TEGDMA nanoparticles. Figure 2b shows the lattice of ZnO at a magnification of 500,000x. Inset demonstrated the diffraction mode, which was the crystalline structure of ZnO. It proved that the ZnO was successfully encapsulated in the PMMA hybrid.
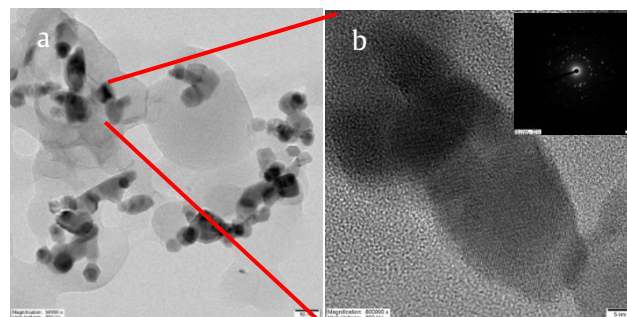

Figure 2 HR-TEM images of (a) PMMA/TEGDMA/ZnO 7 wt% at 100,000x magnifications and scale bar was 50 nm. (b) ZnO nanoparticle and the diffraction mode of ZnO nanoparticle at 500,000x magnifications and scale bar was 5 nm.
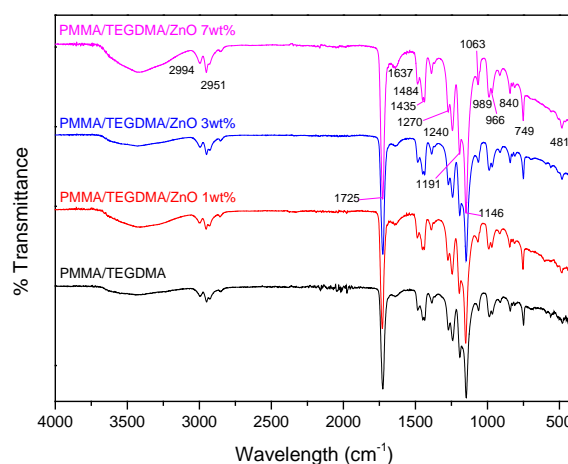
Figure 3 The FT-IR spectra of the PMMA/TEGDMA/ZnO 0, 1, 3 and 7 wt%.

Effect of ZnO on the functional of the hybrids

The function group of the PMMA/TEGDMA/ZnO was discovered by FT-IR spectroscopy. Figure 3 shows the absorption bands at 1063 cm^{-1} corresponding to -C-O-C-. The peaks observed at 1146 cm^{-1} and 1181 cm^{-1} were ascribed to ether carbon (C-O) bond stretching vibrations. The peaks observed at 1725 cm^{-1} and 1146 cm^{-1} were related to the stretching of the carbonyl group (C=O) and C=C groups, respectively [25]. The absorption bands appearing in the range of 1488-1270 cm^{-1} are associated with CH_3 and CH_2 vibrational modes [25]. Furthermore, absorption bands at 2951 cm^{-1} and 2994 cm^{-1} corresponded to the asymmetric -CH_2 stretching mode of PMMA [25]. The absorption band at 1637 cm^{-1} is attributed to

the C=C stretching of the TEGDMA crosslinking agent [26, 27]. The vibration band at 481 cm^{-1} was assigned to the stretching mode of the Zn-O bond [28]. The encapsulation of ZnO in the PMMA hybrid did not change the functional group of the PMMA due to the physical interaction of PMMA and ZnO. It is clearly seen that ZnO was presented in the PMMA hybrid miniemuslion.
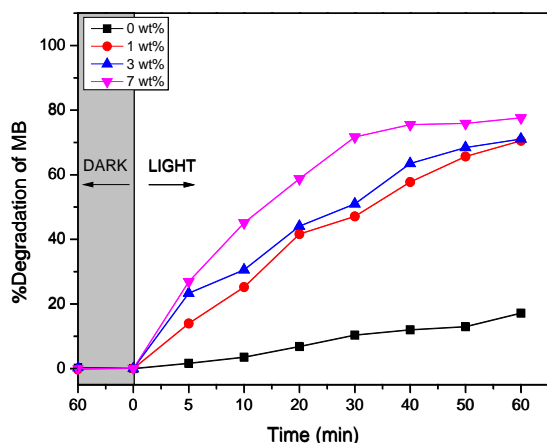

Figure 4 The % degradation of the MB under dark and UV light conditions of PMMA/ZnO with ZnO 0, 1, 3, and 7 wt%.
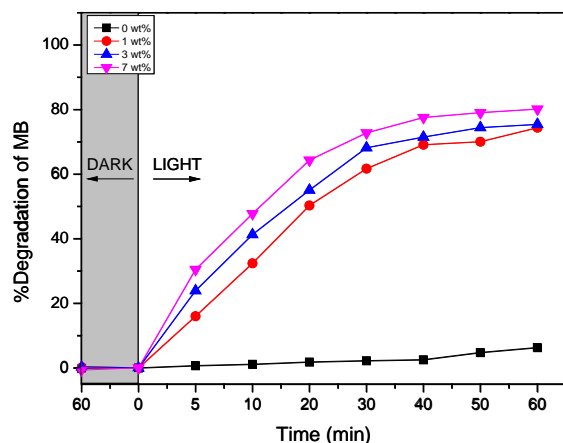

Figure 5 The % degradation of the MB under dark and UV light conditions of PMMA/TEGDMA/ZnO with ZnO 0, 1, 3, and 7 wt%.

Effect of ZnO on the photocatalytic of the hybrids

The photocatalytic was investigated by monitoring the degradation of MB under UV illumination. The % degradation of PMMA/ZnO and PMMA/TEGDMA/ZnO with 0, 1, 3, and 7 wt% of ZnO contents were demonstrated in Figure 4 and Figure 5, respectively. The result shows that there was no MB absorption under dark conditions. Under UV illumination, the % degradation at 3 wt% (Figure 5) reached 55 % in 20 min, while the PMMA/

ZnO at 3% (Figure 4) spent 30 min to reach 51 % MB degradation. Therefore, the maximum MB degradation for PMMA/TEGDMA/ZnO 7 wt% and PMMA/ZnO 7 wt% were 80.1% and 77.6%, respectively. The TEGDMA increased the stability of the PMMA/ZnO hybrid by reducing particle breakage. This results in improved photocatalytic properties [22]. It is noticeable that the TEGDMA increased the photocatalytic capacity of the PMMA hybrid ZnO.

CONCLUSION

The encapsulation of zinc oxide (ZnO) nanoparticles with poly(methyl methacrylate) by miniemulsion polymerization technique was successfully investigated. Triethylene glycol dimethacrylate (TEGDMA) was added to the system as a crosslinking agent in the presence of ZnO from 1 wt% - 7 wt%. The diameter and morphology of the PMMA/ZnO hybrid was in the range of 57 nm - 115 nm by using a field emission scanning electron microscope (FE-SEM). It was found that the diameter was slightly increased with the loading amount of ZnO from 1 wt% - 7 wt%. The HR-TEM images of the PMMA/TEGDMA/ZnO 0, 1, 3, and 7 wt% were studied to confirm the encapsulation of ZnO particles in the hybrid. It proved that the ZnO was successfully encapsulated in the PMMA hybrid. The functional group of the PMMA/ZnO hybrid was analyzed by Fourier Transform Infrared Spectroscopy (FTIR). It is clearly seen that the ZnO encapsulation PMMA/TEGDMA was successfully synthesized via the miniemulsion polymerization method. The photocatalytic properties of the PMMA/ZnO hybrid were also tested via the degradation of methylene blue (MB) solution under UV-A irradiation, and the photocatalytic activities increased when increasing ZnO contents up to 7 wt%.

ACKNOWLEDGEMENT

REFERENCES

1. John Ł, Ejfler J. A brief review on selected applications of hybrid materials based on functionalized cage-like silsesquioxanes. Polymers. 2023;15(6):1452.

2. Young G, Tallia F, Clark JN, Chellappan M, Gavalda-Diaz O, Alcocer EJ, et al. Hybrid materials with continuous mechanical property gradients that can be 3D printed. Mater Today Adv. 2023;17:100344.

3. Zhang M, Gao G, Li C-Q, Liu F-Q. Titania-coated polystyrene hybrid microballs prepared with miniemulsion polymerization. Langmuir. 2004;20(4):1420-4.

4. Katagiri K. Chapter 5 - Organic-Inorganic Hybrid Nanoarchitecture at Mesoscale. In: Ariga K, Aono M, editors. Supra-Materials Nanoarchitectonics: William Andrew Publishing; 2017. p. 117-33.

5. Jahanzad F, Karatas E, Saha B, Brooks BW. Hybrid polymer particles by miniemulsion polymerisation. Colloids Surf A: Physicochem Eng. 2007;302(1-3):424-9.

6. Metanawin S, Metanawin T. Fabrication of hybrid polystyrene-titanium dioxide with enhanced dye degradation and antimicrobial properties: investigation of the effect of triethylene glycol dimethacrylate on photocatalytic activity. Polym Int. 2022;71(7):777-89.

7. Metanawin S, Sornsuwit N, Metanawin T. Miniemulsion polymerization technique enhancement: the photocatalysis of commercial rutile-TiO_2 hybrids with nano poly(methyl methacrylate). Polym-Plast Technol Mater. 2022;61(1):56-68.

8. Metanawin T, Panutumrong P, Metanawin S. Synthesis of polyurethane/TiO_2 hybrid with high encapsulation efficiency using one-step miniemulsion polymerization for methylene blue degradation and its antibacterial applications. ChemistrySelect. 2023;8(11):e202204522.

9. Teo BM, Prescott SW, Ashokkumar M, Grieser F. Ultrasound initiated miniemulsion polymerization of methacrylate monomers. Ultrason Sonochem. 2008;15(1):89-94.

10. Livage J. Sol-gel synthesis of hybrid materials. Bull Mater Sci. 1999;22(3):201-5.

11. Landfester K. Synthesis of colloidal particles in miniemulsions. Annu Rev Mater Res. 2006;36(1):231-79.

12. Rao JP, Geckeler KE. Polymer nanoparticles: Preparation techniques and size-control parameters. Prog Polym Sci. 2011;36(7):887-913.

13. Antonietti M, Landfester K. Polyreactions in miniemulsions. Prog Polym Sci. 2002;27(4):689-757.

14. Zhou J, Cui Y, Yao H, Ma J, Ren H. Nanocapsules containing binary phase change material obtained via miniemulsion polymerization with reactive emulsifier: Synthesis, characterization, and application in fabric finishing. Polym Eng Sci. 2019;59(s2):E42-51.

15. Khan MM, Adil SF, Al-Mayouf A. Metal oxides as photocatalysts. J Saudi Chem Soc. 2015;19(5):462-4.

16. Disha KM. Metal oxide nanomaterials for photocatalytic degradation of antibiotics. Mater Today: Proc. 2023.

17. Yemmireddy VK, Hung YC. Using Photocatalyst metal oxides as antimicrobial surface coatings to ensure food safety-opportunities and challenges. Compr Rev Food Sci F. 2017;16(4):617-31.

18. Lu PJ, Huang SC, Chen YP, Chiueh LC, Shih DYC. Analysis of titanium dioxide and zinc oxide nanoparticles in cosmetics. J Food Drug Anal. 2015;23(3):587-94.

19. Agarwal H, Venkat Kumar S, Rajeshkumar S. A review on green synthesis of zinc oxide nanoparticles - An eco-friendly approach. Resource-Efficient Technologies. 2017;3(4):406-13.

20. Zhou XQ, Hayat Z, Zhang DD, Li MY, Hu S, Wu Q, et al. Zinc Oxide Nanoparticles: Synthesis, Characterization, Modification, and Applications in Food and Agriculture. Processes. 2023;11(4):1193.

21. Fogaça LA, Feuser PE, Ricci-Júnior E, Hermes de Araújo PH, Sayer C, Costa C. ZnO and quercetin encapsulated nanoparticles for sun protection obtained by miniemulsion polymerization using alternative co-stabilizers. Mater Res Express. 2020;7(1):015096.

22. Al-Shannaq R, Farid M, Al-Muhtaseb S, Kurdi J. Emulsion stability and cross-linking of PMMA microcapsules containing phase change materials. Sol Energ Mat Sol C. 2015;132:311-8.

23. Liang K, Liu Q, Peng M. Monodisperse cross-linked polystyrene nanospheres by emulsifier-free miniemulsion polymerization. e-Polym. 2015;15(4):263-70.

24. Erdem B, Sudol ED, Dimonie VL, El-Aasser MS. Encapsulation of inorganic particles via miniemulsion polymerization. Macromol Symp. 2000;155(1):181-98.

25. Singh S, Arora N, Paul K, Kumar R, Kumar R. FTIR and rheological studies of PMMA-based nano-dispersed gel polymer electrolytes incorporated with $LiBF_4$ and SiO_2. Ionics. 2019;25(4):1495-503.

26. Ahangaran F, Navarchian AH. Towards the development of self-healing and antibacterial dental nanocomposites via incorporation of novel acrylic microcapsules. Dent Mater J. 2022;38(5):858-73.

27. Hodásová Ľ, Alemán C, del Valle LJ, Llanes L, Fargas G, Armelin E. 3D-Printed polymer-infiltrated ceramic network with biocompatible adhesive to potentiate dental implant applications. Mater. 2021;14(19):5513.

28. Nagaraju G, Udayabhanu, Shivaraj, Prashanth SA, Shastri M, Yathish KV, et al. Electrochemical heavy metal detection, photocatalytic, photoluminescence, biodiesel production and antibacterial activities of Ag-ZnO nanomaterial. Mater Res Bull. 2017;94:54-63.

The development of association rules for student performance analysis using FP-Growth algorithm as a guideline for multidisciplinary learning

Wongkot Sriurai[1*] and Sumitra Nuanmeesri[2]

[1]Department of Mathematics Statistics and Computer, Faculty of Science, Ubon Ratchathani University, Ubon Ratchathani 34190, THAILAND
[2]Department of Information Technology, Faculty of Science and Technology, Suan Sunandha Rajabhat University, Bangkok 10300, THAILAND
*Corresponding author: wongkot.s@ubu.ac.th

ABSTRACT

This study aims to develop association rules for student performance analysis using the FP-Growth algorithm. The data used for developing the association rules comprised 107 student reports. The reports, voluntarily provided by 107 junior high school students, consisted of student achievement results across 8 subject areas: Thai Language, Mathematics, Science, Social Studies, English Language, Computing Science, Visual Arts, and Home Economics. The data was applied to developing association rules using the FP-Growth algorithm towards WEKA, a machine learning software. The research team designed the process consisting of the following 5 stages: data collection, data preparation, model formulation, model evaluation, and model application. After achieving the association rules, the research team applied them to the prototype development of a student performance analysis system for promoting students' academic excellence. The system could be operated by Android mobile phones. According to the research results, the association rules developed by the algorithm provided a confidence level of 92%, and a rule of 7 rules will be generated. The findings indicated the correlations between the subject areas, which shared similar individual students' academic achievements (≥ 80 scores). The association rules could be applied to the multidisciplinary curriculum planning, which benefited students and promoted academic excellence. For example, by applying Rule, it could be assumed that students who earned 80 scores or higher in the English subject would likely earn identical scores from their Thai Language class. Therefore, they could effectively learn to integrate English and Thai languages. To illustrate, students may be asked to translate song lyrics from English to Thai, serve as tourist guides or translators, or even give welcome speeches to foreign guests.

Keywords: Association rules, FP-Growth, Multidisciplinary learning

INTRODUCTION

Education is a foundation of human beings' development process, which supports the maturation of their physics, emotions, intelligence, morality, and ethics. It also facilitates personal adaptation and a peaceful way of living. Thailand has paid attention to providing educational opportunities, human capital investment, and lifelong learning. This conforms to the National Education Act of B.E. 2542 (1999) and its second amendment, the National Education Act of B.E. 2545 (2002), [1]. Moral, ethical, and cultural intelligence allow individuals to live with each other happily. Therefore, today's educational management must focus on these qualities, especially during the COVID-19 pandemic.

Schools are educational institutions responsible for educational management. They are obliged to maintain academic standards in agreement with the demands of society as well as students' interests, talents, and capabilities. Each school attempts to enhance students' knowledge and skills for their future careers. In Thailand, opportunity expansion schools have provided 3-year education to countless junior high school students. A huge number of 6th graders who had graduated from different elementary schools entered these opportunity expansion schools. Some of them were students from other districts or provinces, creating diversities in talents and skills among the young learners. At the stage of lower secondary education, students can choose to study academic or vocational subjects based on their preferences. This helps the students to obtain academic and vocational knowledge appropriate for their age, market demand, and individual interests. Ultimately, these students will achieve their own personal ambitions and the society's common goals.

At present, association rules have been applied to discover the rules in large data sets. For example, Dharmaraajan and Dorairangaswamy investigated the

correlation patterns of a weblog's data using FP-Growth and Apriori algorithms to classify user behavior when accessing the weblog's data. They compared the effectiveness of the two algorithms in data correlation analysis with the Rapid Miner program. Their research findings showed that both algorithms could analyze the weblog's usage patterns as well as characteristics of user behavior. The data could be used to improve the web design or offer services to-the users more productively. After comparing the effectiveness of both algorithms in terms of data size and time spent on data processing, FP-Growth spent less time on data processing and provided higher productivity than Apriori [2]. Gashaw and Liu assessed the performance of popular data mining algorithms, including Eclat, Apriori, and FP-Growth. They employed three sets of weblog data to analyze association rules by comparing the effectiveness of the algorithms in two aspects: 1) the amount of time spent on data processing and 2) memory usage. They found that Apriori performed relatively better when the support value was high regarding the amount of time spent on big data processing. However, if the support value decreased, all three algorithms spent more time processing data. Only FP-Growth could create a new dataset within the expected duration, while Eclat required the most significant amount of time in all cases. Regarding memory usage, FP-Growth demanded the smallest number of memory units compared to other algorithms when the support value was high. Eclat and Apriori required more memory units when the support value was low. Meanwhile, FP-Growth constantly uses the same number of memory units [3]. Faza et al. investigated the association rules of graduate student data gained from an Indonesian university. They applied the FP-growth algorithm by which the data used for constructing association rules consisted of types of schools, types of admission, grade point average (GPA), and duration of study. Their research results demonstrated that attributes correlating with graduation were public high schools outside Medan City, regular admission, GPA between 3.00-3.49, and study duration. According to the findings, the research team could identify which schools were suitable for encouraging students to enroll at this university and graduate within the regular timeframe [4]. Jongkasikit applied a data mining technique to explore factors affecting higher education enrollment at the Faculty of Industrial Technology, Lampang Rajabhat University. She accumulated data from 334 students from Years 1-3 at the faculty and then reduced the dimensionality of the data by employing the Evolutionary Selection technique. The dimensionally reduced data was accordingly used to find association rules for applying FP-Growth. Their findings disclosed 36 factors affecting higher education enrollment of these students. 35 association rules were constructed based on the discovered factors [5]. According to the previously

mentioned studies, each research applied the association rules to find correlations between different item sets. Overall, it can be assumed that association rules can be practically used for investigating hidden data correlations.

Thailand has constantly modified its educational management patterns and techniques to equip young learners with knowledge and skills in Thai language, mathematics, science, social studies, English language, computing science, visual arts, and home economics. These subjects are compulsory for every student. Thus, the research team aims to explore students' aptitudes by analyzing the student's past academic performance through association rule mining [6]. The association rules can signify the relationships between subject areas where students share similar achievements. Once the association rules have been formed, they are applied to the multidisciplinary curriculum planning. The newly developed curriculum is expected to benefit the students and promote their academic excellence to the greatest extent. This research aims to develop association rules for student performance analysis by using the FP-Growth algorithm and to develop the information system by using the FP-Growth algorithm for designing a multidisciplinary curriculum.

The paper is organized as follows. The next section describes the research methodology. Subsequently, we report on the association rules for student performance analysis created by the FP-Growth algorithm via the WEKA. We conclude by summarizing our contributions.

MATERIALS AND METHODS

Research methodology

After reviewing relevant theories and previous studies, the research team designed the process consisting of the following 5 stages: data collection, data preparation, model formulation (using FP-Growth Algorithm), model evaluation, and model application (See Figure 1).
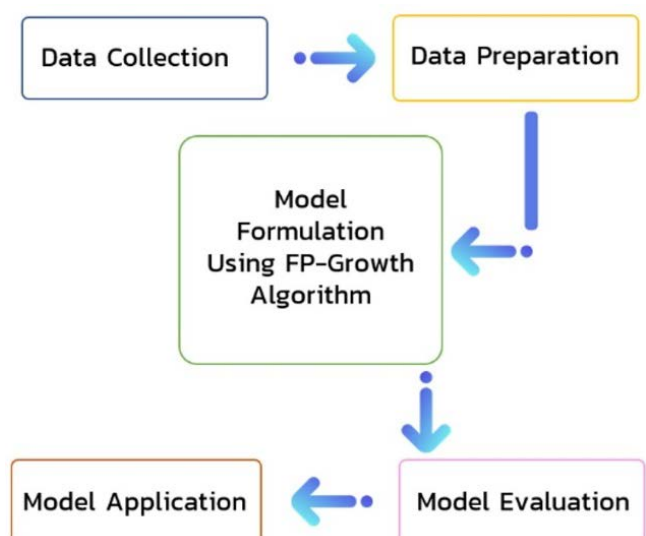

Figure 1 Research process.
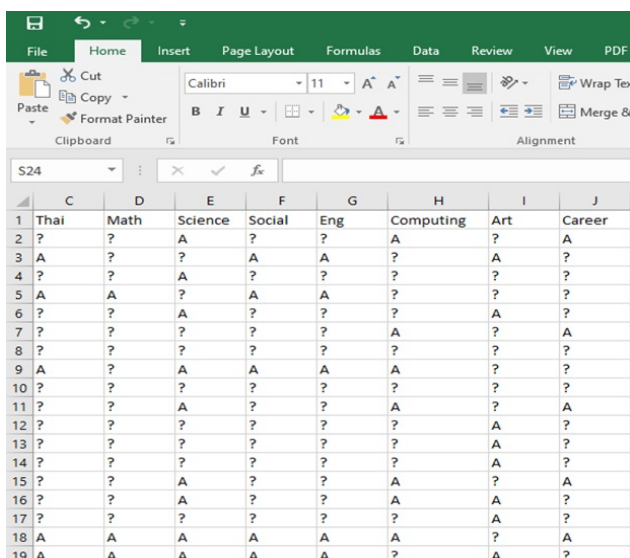
1. Data collection

The data used for developing the model consisted of school reports voluntarily provided by 107 students from a junior high school. Ethics approval for the conduct of this study was obtained. The data comprised student grades of 80% or higher across 8 subject areas, including Thai language, mathematics, science, social studies, English language, computing science, visual arts, and home economics. These subjects were represented by the variables shown in Table 1.

Table 1 Examples of variables indicating each subject.

Variables	Descriptions
Thai	Thai Language
Math	Mathematics
Science	Science
Social	Social Studies
Eng	English Language
Computing	Computing Science
Art	Visual Arts
Career	Home Economics

2. Data preparation

Following data collection, the data cleaning process was operated. At this stage, the incomplete datasets were eliminated. In this case, the student grades lower than 80% were excluded. Once the data cleaning process had been completed, the data was converted into a .csv file, as illustrated in Figure 2. Subsequently, the converted data was applied to the model development process.
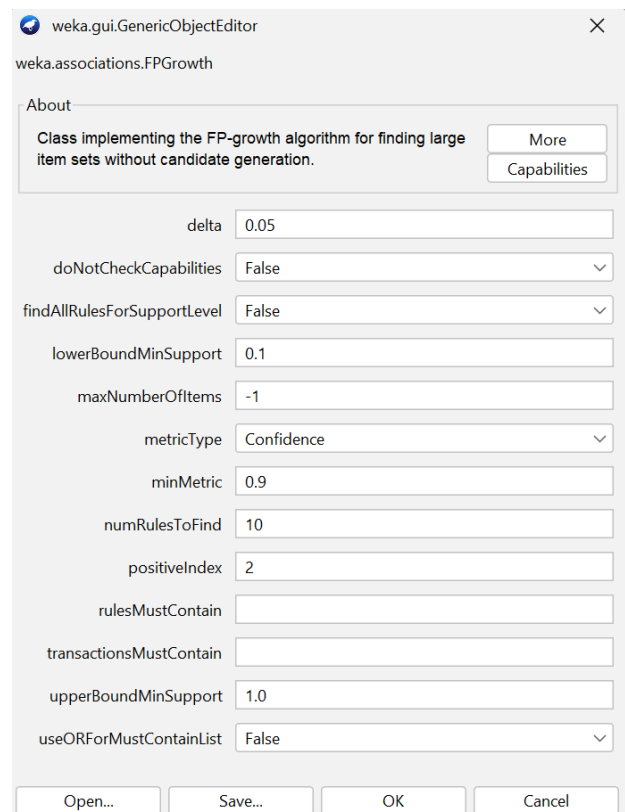

Figure 2 Examples of data used for model development.

Figure 2 displays examples of data used for model development. The developed model was expected to investigate the association rules for student academic performance analysis effectively. 'A' represents 'Grade 4' (scores ≥ 80%) in each subject.

3. Model formulation using FP-Growth algorithm

The model representing the correlations between subject areas that shared similar individual student achievements (scores ≥ 80%) was formulated at this stage. It was constructed using the FP-Growth algorithm via WEKA, a machine learning software. The following parameters were identified to create association rules: lowerBoundMinSupport = 0.1, minMetric = 0.9, and numRulesToFind = 10.

Figure 3 Association rules parameters in WEKA.

The FP-Growth algorithm searches for frequently co-occurring itemsets. FP-Growth algorithm was used to find the interesting rules from education data. Its pattern growth consists of the following steps [7, 8].:

1. First data scanning: The frequency of each dataset in the database is counted. Then, the itemsets with a minimum support value higher than or equal to the identified target are ordered based on the frequency from high to low to formulate the Header table.

2. Second data scanning: A FP-Tree is created by scanning each data list in the database. The item sets disappearing in the Header table are excluded. The remaining datasets are re-ordered in the Header table. These datasets are used to create node trees added to the FP tree. The nodes with the same itemsets are connected and then added to the Header table.

3. Conditional pattern base formulation: Each dataset's FP-Tree conditions are created to find frequently co-occurring itemsets. A conditional pattern base is a sub-database comprising sets of frequently co-occurring itemsets in each path. Each itemset is set with the

same frequency as the itemset currently determined by the FP-tree. Afterwards, the FP-tree is formulated in the conditional pattern base, so-called a 'conditional FP-tree'. It is derived from the total sum of frequencies of each item set from all paths. Only the itemsets with the acceptable minimum support value are selected for creating frequently co-occurring itemsets further.

4. Finalization: The frequently co-occurring itemsets are searched by constructing the conditional pattern base and the conditional FP-tree of each dataset towards the 'divide and conquer' technique.

4. Model evaluation

After obtaining the association rules, the reliability of the outputs was evaluated. The evaluation considered the support, confidence, and lift values of the association rules before applying them to curriculum planning for the development of academic excellence. If the consistency index is less than 1, it means there is an inconsistent correlation. On the other hand, if the consistency index is equal to or greater than 1, it means there is a consistent correlation. The values of support are calculated with Formula 1. The confidence calculation of the association rule A=>B is shown in the following formula 2 [7, 8].

$$support(A => B) = support(A \cup B)/P(AB) \quad (1)$$

$$confidence(A => B) = support(A \cup B)/support(A) \quad (2)$$

5. Model application

Once the association rules of students' academic achievements (at a grade of 80% or above) had been obtained through the model developed by the FP-Growth algorithm, they were applied to developing an information system for designing a multidisciplinary curriculum. The curriculum was aimed to promote students' academic excellence based on their preferences and talents.

RESULTS AND DISCUSSIONS

The association rules of students' academic achievements were discovered by constructing the aforementioned model towards the use of FP-Growth via WEKA. According to the investigation of association rules across the subject areas, the association rules simultaneously emerged and passed the determined minimum support value. Even if their order was rearranged, similar association rules were subsequently obtained.

These association rules were found to have a confidence level of 92% or higher, meaning they were statistically reliable. As a result, the acquired association rules could be applied to curriculum planning for promoting students' academic excellence. Figure 4 illustrates the association rules for student performance analysis created by the FP-Growth algorithm.
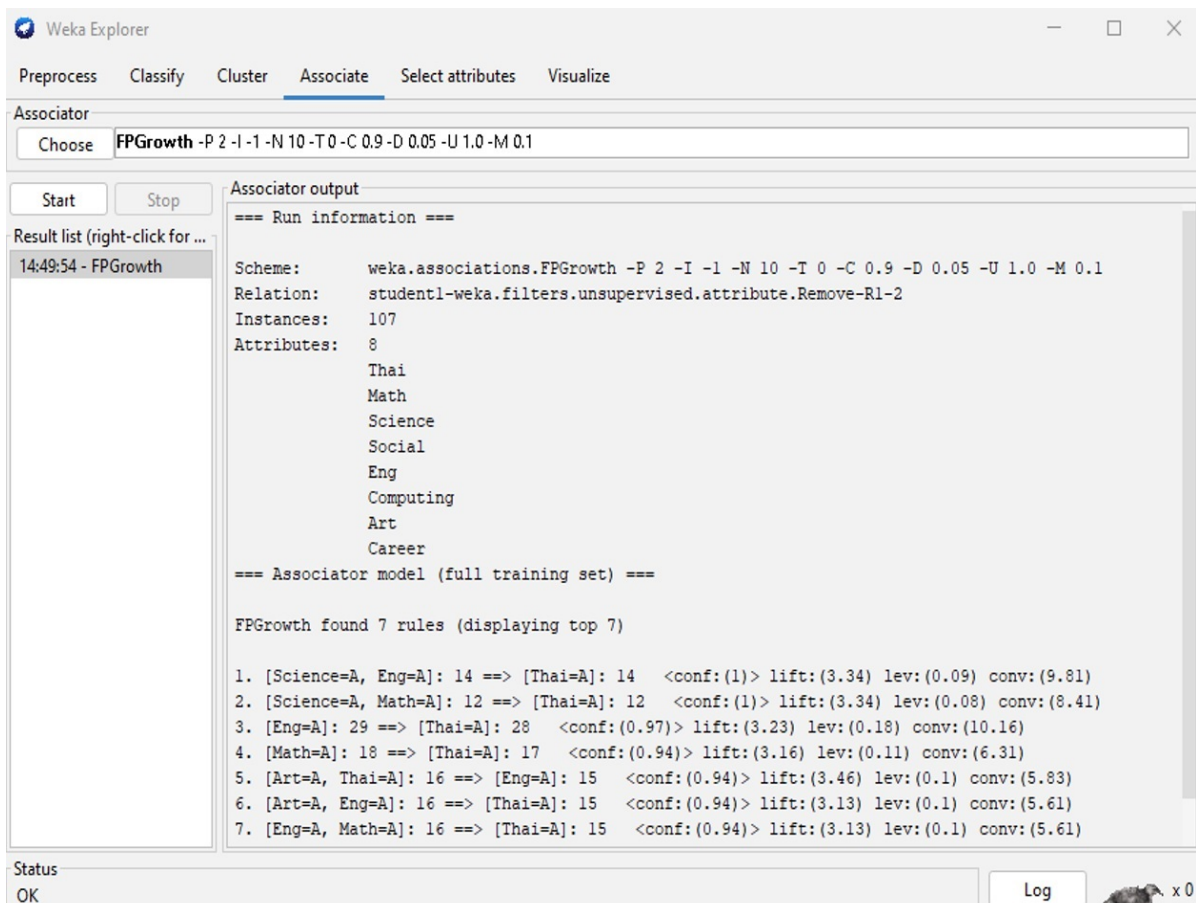

Figure 4 Association rules gained from the analysis of student's academic achievements.

According to Figure 4, there were 7 association rules of students' academic achievements as follows.

Rule 1: Students who received A grades in Science and English Language were more likely to receive an A grade in the Thai Language subject (at a confidence level of 100%).

Rule 2: Students who received A grades in Science and Mathematics were more likely to receive an A grade in the Thai Language subject (at a confidence level of 100%).

Rule 3: Students who received an A in English were more likely to receive an A in the Thai language subject (at a confidence level of 97%).

Rule 4: Students who received an A in Mathematics were more likely to receive an A in the Thai Language subject (at a confidence level of 94%).

Rule 5: Students who received A grades in Visual Arts and the Thai Language were more likely to receive an A grade in the English Language subject (at a confidence level of 94%).

Rule 6: Students who received A grades in Visual Arts and English Language were more likely to receive an A grade from the Thai Language subject (at a confidence level of 94%).

Rule 7: Students who received A grades in English Language and Mathematics were more likely to receive an A grade in the Thai Language subject (at a confidence level of 94%).

As the association mentioned above rules demonstrated, multidisciplinary curriculum planning could be achieved. For instance, by applying Rule 3, it could be assumed that students who earned 80 or higher scores in the English subject were likely to earn the same scores from their Thai language class. Therefore, they could effectively learn to integrate English and Thai languages. To illustrate, students may be asked to translate song lyrics from English to Thai, serve as tourist guides or translators, or even give welcome speeches to foreign guests. Another example is the application of Rule 4 (Mathematics scores ≥ 80% = Thai scores ≥ 80%). Interactively, students may be asked to summarize and evaluate media reliability while learning about statistical data collection (the combination of Chapter 4, Statistics in the Mathematics subject and Module 1, Creative Communication in the Thai language subject).

After achieving the association rules, the research team applied them to the prototype development of a student performance analysis system for promoting students' academic excellence. The system could be operated by Android mobile phones, as shown in Figure 5.
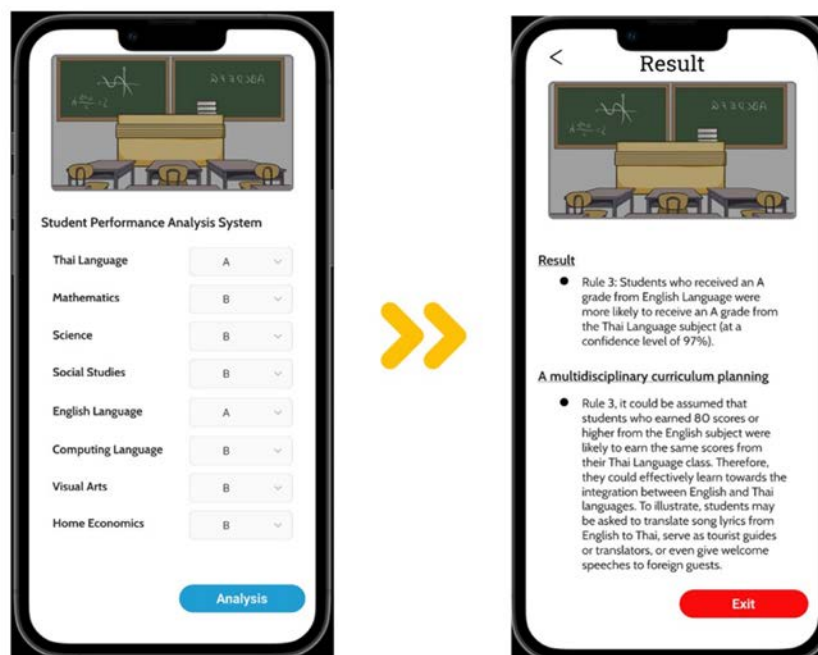
Figure 5 Example of student performance analysis system.

CONCLUSION

Educational management based on individual talents and preferences can contribute to students' higher education and job opportunities. Particularly for students at opportunity expansion schools with high talent diversity, instructors should analyze and determine the best ways to teach each student effectively and appropriately. This study formulated the association rules of students' academic achievements using the FP-Growth algorithm via the WEKA data mining software. The research findings revealed that the association rules developed by FP-Growth could achieve a confidence level of 92% and higher. This implies that these association rules could be applied to multidisciplinary curriculum planning aimed at

academic excellence. For instance, students who earned 80 or higher in the English subject were likely to earn identical scores in their Thai Language class. Therefore, they could effectively learn to integrate English and Thai. The findings indicated the correlations between the subject areas, which shared similar individual students' academic achievements (≥ 80 scores). Therefore, teachers can design teaching and learning using shared activities between subjects. Our research results are consistent with a study conducted by Gashaw and Liu [3] as well as research carried out by Jongkasikit [5] and Ashika et al [6]. These previous studies applied the association rules to the examination of data correlations. They also discovered that the FP-Growth algorithm could explain the data correlations.

ACKNOWLEDGEMENT

REFFERRENCES

1. Ministry of Education. National Education Act of B.E. 2542 and the Second and Third Amendments (B.E. 2545 and B.E. 2553), Relevant Laws, and Compulsory Education Act B.E. 2545. Bangkok: Office of the National Education Commission; 2007.

2. Dharmaraajan K, Dorairangaswamy MA. Analysis of FP-Growth and Apriori Algorithms on Pattern Discovery from Weblog Data. 2016 IEEE International Conference on Advances in Computer Applications (ICACA); 2016 Oct 24; Coimbatore, India: IEEE; 2017.

3. Gashaw Y, Liu F. Performance Evaluation of Frequent Pattern Mining Algorithms using Web Log Data for Web Usage Mining. 2017 10th International Congress on Image and Signal Processing, BioMedical Engineering and Informatics (CISP-BMEI); 2017 Oct 14-16; Shanghai, China: IEEE; 2018.

4. Faza S, Rahmat RF, Nababan EB, Arisandi D, Effendi S. The association rules search of Indonesian university graduate's data using FP-growth algorithm. 10th International Conference Numerical Analysis in Engineering, Banda Aceh, Indonesia; 2017 Aug 24-25; Banda Aceh, Indonesia: IOP Conference Series: Materials Science and Engineering; 2018.

5. Jongkasikit NN. An Application of FP-Growth Algorithm to Find Factors in Choosing to Study in the Faculty of Industrial Technology Lampang Rajabhat University. Industrial Technology Lampang Rajabhat University Journal. 2018;11(2):29-39.

6. Ashika KJ, Jagruthi MN, Nikhil N, Pooja S. Educational data analytics using association rule mining for student job prediction. International Research Journal of Engineering and Technology (IRJET). 2020;7(6): 3979-84.

7. Han J, Kamber M, Pei J. Data Mining: Concepts and Techniques (The Morgan Kaufmann Series in Data Management Systems). 3rd ed. Morgan Kaufmann; 2011.

8. Sinsomboonthong S. An efficiency comparison in prediction of Khao Dok Mali 105 paddy rice classification with data mining techniques. Thai Science and Technology Journal (TSTJ). 2020;28(3): 394-402.

Development of Samed mushroom (*Boletus griseipurpureus* Corner) crackers and quality study during storage

Chompunooch Somalee[1]*, Natta Kachenpukdee[1] and Amornrat Angajchariya[2]

[1]Department of Aquaculture and Fishery Product, Faculty of Science and Fishery Technology, Rajamangala University of Technology Srivijaya, Trang 92150, THAILAND

[2]General education, Faculty of Science and Fishery Technology, Rajamangala University of Technology Srivijaya, Trang 92150, THAILAND

*Corresponding author: chompunooch.s@rmutsv.ac.th

ABSTRACT

The objectives of this research were to develop cracker products using pre-treated Samed mushrooms in three variations (boiling water, brining, and soaking in herbal water), assess the proximate composition, evaluate their chemical and physical properties, and assess the quality of Samed mushroom crackers during storage. The proximate composition of fresh Samed mushrooms (per 100 g) revealed moisture of 92.08 g, carbohydrates of 2.60 g, protein of 3.37 g, ash of 0.81 g, fat of 0.23 g, and fiber content of 0.91g. The energy content was 29.59 kcal/100 g. The proximate composition of Samed mushroom crackers per 100 g indicated the following: carbohydrates 69.25 g, crude fat 24.08 g, protein 4.36 g, ash 1.82 g, and moisture 0.49 g. Additionally, the energy content was 511.6 kcal/100 g, with sugar and sodium contents measuring at 0.91 g and 552.3 mg/100 g, respectively. The study on the different types of pre-treatment solutions for Samed mushrooms demonstrated that pre-treatment by soaking in herbal water received the highest acceptance from consumers, with an overall liking score of 8.97. In the development of Samed mushroom crackers, the appropriate ratio of Samed mushroom to fish was 15 to 85. Regarding the microbiological quality changes during a 30-day storage period, the study revealed that the total viable count was <10 CFU/g, yeast count was 7.0 CFU/g, *Bacillus cereus* count was <100 CFU/g, *Staphylococcus aureus* count was <10 CFU/g, *Clostridium perfringens* count was <100 CFU/g, and *Escherichia coli* count was 3.0 CFU/g. In terms of chemical quality, the peroxide value was 0.57 meq/kg which is consistent with the Thai Community Product Standard (Cracker 107/2011). Storage for 30 days found that the condition of adding nitrogen gas resulted in the finding of less microorganisms than in a normal atmosphere, along with conditions for adding oxygen absorbers together with desiccant.

Keywords: Proximate composition, Pre-treatment Samed mushroom, Samed mushrooms crackers

INTRODUCTION

Crackers are a type of snack made primarily from flour, such as cassava flour, rice flour, or wheat flour. They consist of various ingredients including fish, shrimp, pumpkin, taro, black sesame, white sesame, mushrooms, salt, garlic, pepper, sugar, and water. These ingredients are mixed with water and seasonings to form a dough, which is then shaped, steamed until cooked, cut into thin sheets, and dried in the sun. The process of making fish crackers begins by thoroughly mixing all the ingredients with a mixer for 20 minutes. The mixture is then shaped into lumps with a diameter of 2.5 cm and a length of 15 cm, placed inside a container lined with banana leaves, and steamed for about 40-60 minutes. Afterward, it is left to reach room temperature for 30 minutes, followed by refrigerating at 4 degrees Celsius for 24 hours. Then, it is sliced to a thickness of 2 mm and dried using a hot air dryer at 60 °C for 3 hours [7].

The Samed mushroom, scientifically known as *Boletus griseipurpureus* Corner, is a type of mushroom that naturally grows in the sandy soil area of the Samed forest. Samed mushrooms typically emerge after a prolonged drought followed by heavy rainfall lasting 3-4 days, in other words, during the transition between the end of summer to the beginning of the rainy season. They are frequently found in regions where Samed trees or Acacia Thep trees grow. Due to their bitter taste, the primary method of processing involves boiling the mushrooms with tamarind leaves and applying salt. People relish them by either dipping them in chili paste or incorporating them into coconut milk curries. As there is a limited time for collecting fresh mushrooms, typically during April and May, processing is necessary to extend their shelf life and enhance their taste for variety.

Previous research revealed that Samed mushrooms had a lower carbohydrate content compared to other

edible mushrooms, typically ranging from 6-11%. They are also low in fat, which is a common characteristic of edible mushrooms. Furthermore, Samed mushrooms have a relatively high protein and fiber content [9, 10], making them a suitable choice for individuals who are controlling their weight. The high fiber content aids in reducing constipation, improving the excretory system, and helping lower cholesterol and blood sugar levels [4, 6]. The development of Samed mushroom crackers involves studying and refining the cracker formula. The preparation of Samed mushrooms as a raw material aims to tackle the issue of mushroom bitterness through boiling, brining, and soaking in herbal water. Mixing Samet mushrooms into the process of making fish crackers serves to increase the proximate composition of the products and is accepted by consumers. This study focuses on cracker products, which are categorized as ready-to-eat food items but necessitate frying prior to sale. These products encounter specific challenges, notably rancidity, and a decrease in crispness when stored over extended periods. To mitigate these issues, extensive research has been conducted on appropriate packaging and storage conditions, aimed at extending the shelf life of these crackers. A significant advancement in this area is the implementation of a gas-flushing technique within the filling process, employing a modified atmosphere rich in nitrogen gas. This method has been proven to effectively prolong the shelf life of the products, thereby enabling extended storage durations without compromising quality prior to consumption. Additionally, the study encompasses a thorough quality analysis of various products, including an in-depth assessment of the proximate composition of Samed mushrooms and the final cracker products. Such analysis is crucial in ensuring the proximate composition and overall quality of the end products. The implications of this research extend to local community engagement. The findings and methodologies can be shared with local community groups, fostering the creation of new employment opportunities and aiding in the development of a unique product that is specific to the region. This approach not only utilizes local natural resources to their fullest potential but also aims at minimizing waste.

MATERIALS AND METHODS

The study was conducted in the laboratories of the Department of Aquaculture and Fishery Product at the Faculty of Science and Fisheries Technology, Rajamangala University of Technology Srivijaya, located in Trang province, southern Thailand. Fresh Samed Mushrooms (*Boletus griseipurpureus* Cor.) were procured from villagers who gathered them in the Samed forest area. Tapioca flour, fish meat, garlic, salt, and other ingredients were sourced from the local market.

1. Comparison of the proximate composition of fresh Samed mushrooms and three pre-treatment conditions for Samed mushrooms

The proximate composition of fresh Samed mushrooms and Samed mushrooms pre-treated in boiling water, brine, and herbal water was analyzed. The analysis examined the content of energy, protein, fat, carbohydrates, moisture, and crude fiber in 100 g, following AOAC (2016) standards. It includes moisture (methods 925.45 and TE-CH-357), protein (923.03), crude fiber (925.45 and TE-CH-122), crude fat (948.15), and ash (923.03). Total energy was calculated according to the following equations: (1) and (2).

Energy (kcal) = 4 × (g protein + g carbohydrate) + 9 × (g lipid)   (1)

Carbohydrate content = 100 – {moisture (g) + crude protein (g) + total fat (g) + crude fiber (g) + total ash (g)}; where (g) = grams per 100 grams   (2)

2. Pre-treatment methods for Samed mushrooms

Selecting Samed mushrooms as raw materials for making Samed mushroom crackers involved three types of processed mushrooms including boiling water, brining, and soaking in herbal water as follows:

2.1 Samed mushrooms in boiling water

Samed mushrooms were prepared by trimming the roots, removing soil and any spoiled parts. Samed mushrooms were put into the boiling water with 2% salt. Boil them for 2 rounds to reduce the bitterness and mucilage from the mushrooms. The mushrooms were removed from boiled water using a strainer and placed in cold water immediately.

2.2 Samed mushrooms soaked in brine

Brine water was prepared by mixing 2% of salt into clean water. This brine was boiled and then poured into the bottle with mushrooms. Let its temperature drop to ambient before closing the lid. Submerge the Samed mushrooms in a brine solution for two hours before their utilization.

2.3 Samed mushrooms in herbal water

Prepare galangal (3%), lemongrass (3%), acetic acid (0.4%), salt (2%) and clean water (91.6%). Boil these ingredients for 5 minutes, then filtered. Take the mushrooms that have been boiled in water and place them in a glass bottle. Add the herbal water until the mushrooms are fully submerged. Wait for it to cool, and then close the lid. Submerge the Samed mushrooms in herbal water for two hours before utilization.

3. Ingredients and method for Samed Mushroom Crackers

Due to the bitterness of Samed mushroom, the fish cracker recipe was selected as a prototype for mixing with the mushroom. The previous formula of fish cracker was used as a fundamental recipe for the development of mushroom cracker [10], with tapioca

flour (52%), clean water (21%) fish meat (8%), wheat flour (7%), garlic (4%), pepper (4%), salt (1%), sugar (3%), and fish sauce (3%) weighed according to the levels of flour required per treatment and the formulation. Procedures for making crackers begin by weighing the ingredients for the crackers according to the specified proportions and various seasonings. Divide the dough into two parts. The 1st part was kneaded with boiling water until homogeneous. Part 2: Combine the ingredients in item 1 and massage together with part 1 and various ingredients until homogeneous. Take the dough and shape it into cylindrical pieces with a diameter of about 1.5 inches. Steam the dough until it fully cooked. This process usually takes approximately 1 hour and 30 minutes. Let the cooked dough cool at room temperature, then refrigerate it at a temperature between 4 to 10°C overnight. Cut the dough into thin slices, approximately 2 mm thick and proceed with drying the sliced dough, either through natural air drying or by using an oven.

Pre-treatment mushrooms in boiling water, brining, and soaking in herbal water. These mushrooms were chosen based on sensory testing to determine consumer acceptance regarding color, odor, flavor, texture, and overall liking.

4. Sensory evaluation of value-added products

Sensory analysis was conducted on three variants of fish crackers, including those treated with pre-treated Samed mushrooms, by 30 panelists. The gender distribution was 34.28% male and 65.72% female, with ages ranging from 18 to 55 years. Of these, 33.33% were aged between 18-22, and 66.67% were between 30-55 years old. Twenty panelists resided within the university, while ten lived outside, all with prior experience in tasting crackers. The panelists independently evaluated the crackers, which were prepared in three distinct formulations, for various sensory parameters such as color, odor, flavor, texture, and overall liking. During the sensory evaluation, panelists were instructed to drink water or rinse their mouths after each assessment to cleanse their palates. The panelists were provided with a hedonic scale questionnaire to assess the value-added products, using a 9-point hedonic scale, from 1 (Extremely dislike) to 9 (Extremely like), ensuring comprehensive feedback on the sensory attributes of each cracker type.

4.1 Investigated the formula for fish cracker production

Fish crackers were prepared by mixing predetermined portions as required by the different formulations (Table 1). For selecting fish cracker recipes based on sensory tests, the study evaluated acceptance in terms of color, odor, flavor, texture, and overall liking. Using a 9-point hedonic scaling test. A minimum of 30 panels were selected from Table 1 to determine the accepted recipes based on the liking scores.

Table 1 Formulation of fish cracker with different ingredients.

Ingredient	Amount (g)		
	Formula 1	Formula 2	Formula 3
Tapioca flour	1000	1000	1000
Fish meat	300	300	300
Salt	10	5	30
Garlic	65	55	65
Pepper	20	30	20
Sugar	35	35	35
Fish sauce	20	25	0
Baking powder	10	10	10
Boiling water	40	40	40

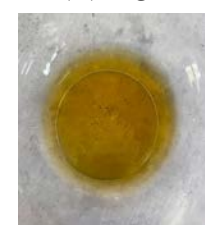(a) Samed mushroom   (b) Tapioca flour

(c) Wheat flour   (d) Sugar

(e) Garlic   (f) Fish sauce

(g) Salt   (h) Baking powder

(i) Ground pepper   (j) Fish meat

Figure 1 Ingredient of Samed mushroom crackers.

4.2 Study of the appropriate amount of Selected Samed mushrooms for cracker properties

Investigate the appropriate proportion of Selected Samed mushrooms (10%, 15%, 20%) to fish meat content in the production for cracker was used to study the suitable quantity of Samed mushrooms in three different sets of formulas:

Formula 1: Samed mushroom content of 10%, fish meat content of 90%.

Formula 2: Samed mushroom content of 15%, fish meat content of 85%.

Formula 3: Samed mushroom content of 20%, fish meat content of 80%.

The most widely accepted recipes for Samed mushroom crackers were chosen through sensory testing. Consumer acceptance of each formula of Samed mushroom crackers was evaluated, considering factors such as color, odor, flavor, texture, and overall liking, using a 9-point hedonic scaling test. A minimum of 30 panels were utilized for this assessment.

Figure 2 Samed mushroom crackers.

4.3 Proximate Composition Analysis of developed Samed mushroom cracker product of appropriate mushroom cracker

The proximate composition analysis includes energy (kcal), crude fat (g), protein (g), carbohydrates (g), cholesterol (mg), ash (g), moisture (g), sugar (g), sodium (mg) content per 100 g. Carbohydrate and energy percentages were calculated following the method in (1). Crude fat, protein, cholesterol, ash, moisture, sugar, and sodium content were determined using AOAC (2016) methods.

5. Product and qualities during storage for 30 days

5.1 Samples of Samed mushrooms with suitable pre-treatment for crackers prepared from recipes accepted by consumers were subjected to the frying process. These samples were then packed using the following three conditions: 1) Nitrogen gas filling condition (gas flushing), 2) Normal atmosphere (control), and 3) Oxygen absorber and desiccant to preserve and study changes in quality in various aspects, namely: 1) Study of chemical quality: Peroxide value (PV) was determined using the method given by AOAC (1969). To prepare the reagents, first mix three volumes of acetic acid (CH_3COOH) with two volumes of chloroform

($CHCl_3$) to create the acetic acid-chloroform solution. Next, make a saturated potassium iodide solution by dissolving excess KI in freshly boiled water, ensuring excess solid remains, and store this in a dark place, testing it daily. Additionally, prepare 0.1 M and 0.01 M sodium thiosulfate solutions according to the procedure in (AOAC 942.27) diluting the 0.1 M solution with freshly boiled and cooled water for the 0.01 M concentration. For the determination process in fats and oils, begin by weighing a 5 g sample and dissolving it in the acetic acid-chloroform solution. Add the saturated potassium iodide solution, followed by water, and titrate with 0.1 M sodium thiosulfate until the color change is observed. Record the volume of sodium thiosulfate used. PV was calculated using the formula given below:

PV (Meq/kg) = S x M x 1000/g test portion, where S = mL $Na_2S_2O_3$ (blank corrected) and M = molarity $Na_2S_2O_3$ solution [1], 2) Study of microbiological quality: Analysis of total viable count, yeast-mold quantity, *Staphylococcus aureus*, *Clostridium perfringen*, *Bacillus cereus*, and *Escherichia coli* in the microbiology laboratory according to the method [1], and 3) Study of chemical changes: Analysis for the value of a_w (Water activity).

5.2 Study the appropriate storage conditions and qualities during storage for 30 days of the product by storing it at room temperature (23-25°C). Random sampling was performed to analyze various aspects according to item (1) at random intervals of 0, 10, 20, and 30 days.

6. Statistical analysis

The research design also incorporated a Completely Randomized Design (CRD). One-way ANOVA tests were used to assess the differences in proximate composition between fresh Samed mushrooms and pre-treatment Samed mushrooms of three types. The data were presented as the mean ± standard deviation (SD). All significance tests were set at $p \leq 0.05$.

RESULTS AND DISCUSSIONS

1. Proximate composition of fresh Samed mushrooms and three pre-treatment conditions for Samed mushrooms

The proximate composition of fresh Samed mushrooms, along with mushrooms subjected to three different pre-treatments, is presented in Table 2. Significant differences ($p \leq 0.05$) were observed in the proximate composition of the samples studied. Pre-treating Samed mushrooms in brine increased their carbohydrate and crude fiber content. However, all three pre-treatment conditions led to a decrease in crude fat and protein content. Among these, pre-treating with boiling water resulted in the highest moisture content. Pre-treatments with brining and soaking in herbal water increased the ash content of the mushrooms, while pre-treatment with boiling water and soaking in herbal

water reduced their energy content. Previous research has revealed that pre-treating Samed mushrooms with boiling water decreases their moisture content. While the ash and protein content increased, the crude fat content was not significantly different from that of fresh sed mushrooms [13]. Pre-treating Samed mushrooms in brine decreases their moisture, ash, crude fat, and protein content [14]. Samed mushrooms are known for their high protein and low-fat content, enriched with various health-promoting bioactive compounds such as phenols, flavonoids, and polysaccharides. Furthermore, processes like drying, storage, and cooking can significantly affect their physical, chemical, sensory, and biological characteristics [10].

Table 2 Proximate composition of fresh Samed mushrooms and pre-treatment Samed mushrooms.

Analysis results	Fresh Samed mush rooms	Pre-treatment Samed mushrooms		
		Boiling water	Brining	Soaking in herbal water
Carbohydrate (g)	2.60 ± 0.02^d	1.98 ± 0.03^c	3.78 ± 0.04^a	3.25 ± 0.03^b
Crude Fibre (g)	0.91 ± 0.03^c	1.08 ± 0.03^a	1.11 ± 0.21^a	1.01 ± 0.12^b
Crude Fat (g)	0.23 ± 0.02^a	0.16 ± 0.15^b	0.15 ± 0.02^{bc}	0.13 ± 0.31^{bd}
Moisture (g)	92.08 ± 0.23^b	92.95 ± 0.16^a	91.72 ± 0.15^c	91.57 ± 0.13^d
Protein (g)	3.37 ± 0.30^a	2.92 ± 0.30^b	2.16 ± 0.15^d	2.77 ± 0.12^c
Ash (g)	0.81 ± 0.02^c	0.19 ± 0.03^d	1.08 ± 0.04^b	1.27 ± 0.03^a
Energy (kcal)	29.59 ± 0.01^a	28.24 ± 0.03^c	29.55 ± 0.01^a	29.29 ± 0.02^b

Note: The different letters in each row indicate that there was a significant difference ($p \leq 0.05$)

2. Developing a suitable fish cracker product formula and studying consumer acceptance based on sensory perception

During the fish cracker production experiment, all three formulas were examined, and consumer acceptance of each cracker formula was evaluated through sensory testing to assess sensory perception quality. The outcomes of this evaluation are presented in Table 3.

Table 3 Sensory test results of the three formulas of fish crackers product.

Attribute	Average liking score		
	Formula 1	Formula 2	Formula 3
Color	8.83 ± 0.38^a	7.07 ± 0.25^c	7.90 ± 0.31^b
Odor	8.47 ± 0.51^a	7.70 ± 0.56^b	7.50 ± 0.50^b
Flavor	8.70 ± 0.47^a	7.30 ± 0.47^b	7.20 ± 0.41^b
Texture	8.73 ± 0.43^a	7.33 ± 0.49^c	7.77 ± 0.43^b
Overall liking	8.87 ± 0.35^a	7.10 ± 0.31^c	7.73 ± 0.45^b

Note: The different letters in each row indicate that there was a significant difference ($p \leq 0.05$)

Therefore, when considering the liking scores in all aspects, it was observed that Formula 1 received the highest score. It consisted of 20.0% fish meat, 66.7% tapioca starch, 0.7% salt, 1.3% pepper, 4.3% garlic, 2.3% sugar, 0.6% baking powder, 1.3% fish sauce, and 2.7% boiling water. The ingredients used in each formula of rice cracker production vary, leading to differences in appearance, color, odor, flavor, texture, and overall liking. Specifically, the quantity of pepper has an impact on the smell, enhancing the product's aroma and helping to eliminate the fishy odor associated with the fish mixed in the rice crackers. In Formula 1, 20 g of pepper are added, as this amount provides the most acceptable level of aroma and taste to consumers.

Fish sauce and salt are combined to enhance the taste and add saltiness. Additionally, the inclusion of 4.3 percent garlic in Formula 1 contributes to a pungent smell and a distinct spicy flavor. Garlic is known for its ability to deodorize the fishy smell of meat, enhance flavor, and add taste to food [7].

Table 4 Sensory test scores of various types of pre-treatment mushrooms utilized in Samed mushroom cracker production.

Attribute	Average Likability Score of Samed mushroom		
	Boiling water	Brining	Soaking in herbal water
Color	7.27 ± 0.83^c	7.63 ± 0.61^b	8.60 ± 0.50^a
Odor	7.30 ± 0.53^c	7.67 ± 0.48^b	8.57 ± 0.50^a
Flavor	7.43 ± 0.57^b	7.70 ± 0.53^b	8.53 ± 0.57^a
Texture	7.27 ± 0.52^c	7.83 ± 0.46^b	8.73 ± 0.52^a
overall liking	7.13 ± 0.51^c	7.80 ± 0.41^b	8.97 ± 0.18^a

Note: The different letters in each row indicate that there was a significant difference ($p \leq 0.05$)

3. Acceptance of different pre-treatment mushrooms for Samed mushroom cracker production

Based on Table 4, the evaluation of sensory quality for Samed mushroom crackers made with different types of pre-treatments Samed mushrooms, namely those pre-treatments in boiling water, brining, and soaking in herbal water, revealed that formula 3 exhibited a statistically significant highest score ($p \leq 0.05$) for all attributes compared to formula 1 and formula 2. Furthermore, the use of herbal water; including galangal, and lemongrass for pre-treatment Samed mushrooms demonstrated that boiling the herbs in water resulted in an appealing aroma. Additionally, the mixture of acetic acid from fermented vinegar helped

reduce the bitterness of the mushrooms when combined with salt. Folk wisdom also suggests the use of sour tamarind leaves during blanching can mitigate the bitterness [8]. Furthermore, boiling Samed mushrooms in a solution of salt and citric acid helps reduce their bitterness. Using a 4% NaCl solution and a 0.3% (w/v) citric acid solution, boiling for 10 minutes affects the taste and texture of the Samed mushrooms, making them more palatable [11].

4. Optimal proportion of Samed mushroom to fish meat in cracker production

The experiment aimed to determine the suitable percentage of pre-treated Samed mushroom in herbal water for the production of Samed mushroom crackers. Consumers participated in a sensory test to evaluate sensory acceptance based on criteria such as color, odor, flavour, texture, and overall liking. The results of the selection process to determine the ideal percentage of Samed mushrooms used in the production of Samed mushroom crackers are presented in Table 5.

Table 5 Results of sensory test scores for Samed mushrooms in the proper amount of fish meat in Samed mushroom cracker production.

Attribute	Average liking score		
	Formula 1 (10 %)	Formula 2 (15 %)	Formula 3 (20 %)
Color	7.17±1.09[b]	7.87±0.63[a]	7.43±0.82[ab]
Odor	7.53±0.90[a]	7.82±0.97[a]	7.53±1.04[a]
Flavor	7.33±0.96[b]	8.10±0.76[a]	8.00±1.02[a]
Texture	7.23±0.97[b]	7.90±0.92[a]	7.97±0.97[a]
Overall liking	7.43±0.86[b]	8.28±0.74[a]	8.13±0.87[a]

Note: The different letters in each row indicate that there was a significant difference ($p \leq 0.05$)

Based on the evaluation results of sensory quality from Table 5, Formula 2 with 15 percent of Samed mushroom received higher consumer acceptance compared to Formula 1 and 3. As a result, 15 percent of Samed mushroom content was selected for further study. Based on the findings regarding the inclusion of Samed mushrooms in cracker products, it was observed that Samed mushrooms possessed a bitter taste. To use them as an ingredient, it is necessary to boil them in hot water and add salt to mitigate the bitterness. Therefore, when merging bitter Samed mushrooms into the product, it is crucial to determine the appropriate quantity. The results of mixing blanched Samed mushrooms with herbs indicated that 15% was the preferred amount among consumers.

Furthermore, Samed mushrooms are highly regarded and widely consumed by villagers. These bitter mushrooms are believed to possess medicinal properties that can aid in reducing blood sugar levels and preventing diabetes [9, 10]. They are also considered delicious food items in both the Northeast and South regions [8].

5. Proximate composition of Samed mushrooms cracker

The analysis results of the proximate composition in Samed mushroom crackers revealed the following values per 100 g of samples: a total energy value of 511.16 kcal; crude fat of 24.08 g; cholesterol of 6.42 mg; protein of 4.36 g; carbohydrates of 69.25 g; sugar of 2.67 g; sodium of 552.308 mg; ash of 1.82 g; and moisture of 0.49 g. Mushrooms are known for their medicinal properties and their ability to support the functioning of vital organs such as the brain, heart, lungs, liver, and blood circulation system. In Chinese medicine, mushrooms are classified as cold medicine due to their properties that aid in reducing fever, enhancing vitality, cooling the body, healing bruises, nourishing the body, and regulating blood sugar levels. Additionally, mushrooms have been found to lower cholesterol levels, reduce blood pressure, act as diuretics, aid in alleviating irritability, nourish nerve cells, and even help inhibit the growth of cancer cells. Regular consumption of mushrooms has shown benefits for lowering blood sugar and reducing cholesterol levels in diabetic patients.

Table 6 Proximate composition of 100 g of Samed mushrooms in herbal water for cracker production.

Proximate composition	Amount	Unit
Energy	511.16	kcal
Crude Fat	24.08	g
Protein	4.36	g
Carbohydrate	69.25	g
Cholesterol	6.42	mg
Ash	1.82	g
Moisture	0.49	g
Sugar	2.67	g
Sodium	552.308	mg

Table 7 Results of the study on the quality of basic chemical and physical components of Samed mushroom crackers.

Type	Basic elements in various fields		
	Moisture (%)	a_w	Peroxide value (meq/kg)
Samed mushroom crackers	0.49	0.35	0.50

Note: Peroxide value unit = meq/kg. = milligram oxygen peroxide equivalent/kg.

6. Product quality changes in Samed mushroom crackers during storage

6.1 The results of various quality studies of Samed mushroom crackers

From the investigation of the basic components of ready-to-eat crackers, the experimental results are presented in Table 7. It was observed that Samed mushroom crackers had a moisture content of 0.49%, a peroxide content of 0.50 mg of peroxide oxygen equivalent/kg, and an a_w value of 0.35 (Community product standard, 1987). The report on the fundamental

constituents of ready-to-eat crackers indicated that the moisture content should not exceed 4.0%, and the peroxide content should not exceed 30 mg peroxide oxygen equivalent/kg. These basic components meet the criteria set by the Office of Community Product Standards for Crispy Crackers (CPS. 107/2011) [11].

6.2 Results of the initial study on the microbiological quality of Samed mushroom crackers

Result of microbiological quality: analysis of total viable count, yeast-mold quantity, *Staphylococcus aureus*, *Clostridium perfringen*, *Bacillus cereus*, and *Escherichia coli* in the microbiology laboratory according to the method [1] is presented in Table 8.

Based on the study of the microbiological quality of ready-to-eat Samed mushroom crackers, the experimental results are presented in Table 8. However, it was observed that microbial analysis values did not exceed the standards set by the Thai Industrial Standards Institute, 2530 (TIS 701-2530), or exceeded the community product standard (107/2011: Crispy Rice), as all analysis values were within the defined limits. Therefore, consumers can safely consume the product. The total variable count value was not more than 1×10^6 CFU/g, yeast was not more than 100 CFU/g, *Bacillus cereus* was not more than 1×10^3 CFU/g, *Staphylococcus aureus* was less than 10 CFU/g, *Clostridium perfringens* was less than 1×10^3 CFU/g, and *Escherichia coli* was less than 3 CFU/g.

Table 8 Results of the microbiological analysis of Samed mushroom crackers.

Microbial analysis	Amount (CFU/g)	Community Product Standards (CFU/g)
Total variable count	<10	Not exceeding $<1\times10^6$
Yeast and Mold	7.0	Not exceeding 100
Bacillus cereus	<100	Not exceeding 1×10^3
Staphylococcus aureus	<10	<10
Clostridium perfringen	<100	Not exceeding 1×10^3
Escherichia coli	<3 MPN/g	<3 per 1 gram of each sample

Note: *Bacillus cereus* <100 = No Bacillus cereus colonies were found on the Petri dish.
Clostridium perfringen <100 = No *Clostridium perfringen* colonies were found on the petri dish.
Total variable count <10 = No total variable count colonies were found on the petri dish.
Staphylococcus aureus <10 = No colonies of *Staphylococcus aureus* on the petri dish

6.3 Proper packaging and packing conditions

From Table 9, the analysis results of the total microbial content of the Samed mushroom crackers in different packing and storage conditions are shown. It was observed that the microorganisms in the nitrogen gas filling condition had the lowest count at 1.2×10^2 CFU/g, at the end of storage. The oxygen absorber and desiccant conditions had counts of 1.8×10^2 CFU/g and the normal atmosphere had a count of 2.1×10^2 CFU/g, respectively. Throughout the 30-day period, the microbial quality remained within the standard for community products (107/2011: Crispy Rice), where the total microbial content should not exceed 1×10^6 CFU/g [11].

Table 9 Results of analysis of total microorganisms of Samed mushroom crackers in different packing and storage conditions.

	Total microbial content (CFU/g)		
Duration (days)	Normal atmosphere (Control)	Add an oxygen absorber and a desiccant	Adjust the atmosphere with nitrogen gas
0	ND	ND	ND
10	ND	1×10	ND
20	1.2×10^2	1.2×10^2	7×10
30	2.1×10^2	1.8×10^2	1.2×10^2

Note: ND= Non Detected = no microbial content found

Table 10 Results of analysis of yeast-mold content in Samed mushroom crackers stored under various conditions.

	Yeast and mold content (CFU/g)		
Duration (days)	Normal atmosphere (Control)	Add oxygen absorber and desiccant	Adjust the atmosphere with nitrogen gas filling
0	ND	ND	ND
10	<10	<10	<10
20	<10	<10	<10
30	<10	<10	<10

Note: ND = Non Detected = no microbial content found

From Table 10, the analysis results of yeast and mold content in Samed mushroom crackers under different packing and storage conditions were obtained. It was observed that there was no difference in the yeast and mold counts among the various packing conditions. The count remained consistently below 10 to 30 days, in accordance with the standards set by the Thai Industrial Standards Institute in 2011. This was achieved by packaging the cracker products in aluminum foil bags during the shelf-life study.

CONCLUSION

The results of this study showed that using pre-treated Samed mushrooms with herbal water affected the physical properties of the Samed mushroom cracker product. However, Samed mushroom crackers could be produced with an optimal Samed mushroom to fish meat ratio, which was found to be 15:85. This ratio has been accepted by consumers. The nitrogen gas filling condition resulted in a decrease in microbial counts

compared to the normal atmosphere and oxygen absorbent filling conditions. This effect was strengthened by including oxygen absorbers and desiccants, ensuring sustained quality for up to 30 days. The findings from this research can be shared with local community groups to foster new employment opportunities and create a distinctive regional product. The study aims to optimize the utilization of local natural resources for maximum benefit while minimizing losses. However, the researcher did not consistently analyze peroxide values throughout the 30-day storage period in the study. It is crucial to monitor these values continuously until the end of the storage period for a thorough assessment of product stability and quality.

ACKNOWLEDGEMENT

REFERENCES

1. Official Method of Analysis of AOAC International. 17th ed. Virginia: AOAC international; 2000.

2. Tanner JT, Barnett SA, Mountford MK, Angyal G, Beare-Rogers JL, Boyer KW, et al. Analysis of milk-based infant formula. Phase V. Vitamins A and E, folic acid, and pantothenic acid: Food and Drug Administration-Infant Formula Council: Collaborative study. J AOAC Int. 1993;76(2):399-413.

3. Official Methods of Analysis of AOAC International. 20th eds. Gaithersburg: AOAC international; 2016.

4. Anderson JW, Baird P, Davis RH Jr, Ferreri S, Knudtson M, Koraym A, et al. Health benefits of dietary fiber. Nutr Rev. 2009;67(4):188-205.

5. Chanthep S. Study on factors affecting the fruiting of wild mushrooms and their utilization [dissertation]. Faculty of Science and Technology: Songkhla Nakarin University; 1993.

6. Chawla R, Patil GR. Characterization and potential application of blend of passion fruit peel with rice flour in an extruded product for fiber enhancement. Compr Rev Food Sci Food Saf. 2010;9(2):178-96.

7. Garlic: Nutritional Benefits and Medicinal Properties [Internet]. Honestdocs. 2019 [cited 2023 Sep 16]. Available From: https://www.honestdocs.co/herbal-garlic-help-disease

8. Khatun K, Mahtab H, Khanam P A, Sayeed MA, Khan KA. Oyster mushroom reduced blood glucose and cholesterol in diabetes subjects. Mymensigh Med J. 2007;16:94-9.

9. Khemthong C, Chamchan R, Suttisansanee U, Charoenkiatkul S, Chupeerach C, Nattira ON. Development of healthy snack from sa-med mushroom (*Boletus griseipurpureus* Corner). Walailak J Sci & Tech. 2020;17(11):1157-67.

10. Liu Q, Sun L, Ding Y, Zhuang Y. Chemical composition, health benefits, food processing effects and applications of Boletus: a review. Crit Rev Food Sci Nutr. 2023;1-23.

11. Miracle: "Bitter Mushroom" Found in Yucalipus Forest Reduces Diabetes [Internet]. Mgronline. 2019. [cited 2023 Sep 16]. Available From: https://mgronline.com/local/detail/9600000054978.

12. Community Product Standard for Crispy Crackers: M. Por. Chor.107-2554 [Internet]. Bangkok: Ministry of Agriculture and Cooperatives. 2011. [cited 2023 Sep 16]. Available From: https://www.xn--12ca9cdcza1fboh6b4ca0evmxcuh.com/certificate/view?product_id=509&code_certificate_id=18.

13. Phugan P, Pramai P, Inket S, Singsom S. Product development of TOM YUM PUMPKIN Cracker. PSRU Journal of Science and Technology. 2019;4(3):15-26.

14. Rana V, Bachheti RK, Chand T, Barman A. Dietary fibre and human health. Int j food saf nutr. 2011;4(2-4):101-18.

Development of an innovative wireless power transmission model for marine applications

Umar Farooq[1], Hajira Masood[1], Jiropast Suakaew[2], Kruawan Wongpanya[3] and Wanchai Pijitrojana[1*]

[1]Department of Electrical and Computer Engineering, Thammasat School of Engineering, Thammasat University, Pathum Thani 12120, THAILAND
[2]Department of Integrated Engineering, Faculty of Engineering, Pathumwan Institute of Technology, Bangkok 10330, THAILAND
[3]Spectroscopic and Sensing Devices Research Group, National Electronics and Computer Technology Center (NECTEC), Thailand Science Park, Pathum Thani 12120, THAILAND
*Corresponding author: pwanchai@engr.tu.ac.th

ABSTRACT

The conventional wired charging system for ship-to-shore charging of underwater vehicles is prone to specific problems related to unreliable connection mechanisms and safety. The wireless charging system overcomes the danger of electrocution, as the power is transferred from the shore to the ship via electromagnetic induction instead of traditional ways of transferring AC power in the marine environment. This paper presents a novel system-level modeling and designing of wireless power transmission for marine applications. The proposed system comprises three main components: (a) a shore-side mobile transmitter (Shore-SMT), (b) an onboard static receiver, and (c) another ship-side mobile transmitter (Ship-SMT). The Shore-SMT and Ship-SMT, each consisting of a circular array of magnets, rotate in the vicinity of the receiver with a fixed circular variety of coils, resulting in voltage induction in the receiver coil. Consequently, the induced voltage in the receiver coil charges the onboard batteries. COMSOL® MULTIPHYSICS environment is used for the modeling and simulation of the proposed system using finite element method (FEM). The test cases simulate the individual and mutual rotation of the transmitters at several distances from the receiver coil. A prototype of the model is also developed. Experimental results from the developed prototype show promising performance as the percentage of transferred voltage increases from a single layer of x9 coil and x9 magnet bars to 70-75% and 80% in a double layer of x9 Ferro bars with x9 winding coils and double-sided x12 magnets and x9 winding coils respectively. It proves to be a better alternative to the conventional methods used for Ships and Vessel charging.

Keywords: WPT, Underwater vehicles, Wireless charging, FEM analysis

INTRODUCTION

With the increasing development in wireless technology, power cords will soon become obsolete and past memory. The advancement in wireless power transmission (WPT) makes it a promising technology to implement in unsafe applications if exposed to electric power, such as coastal transportation systems (charging ferries). In marine applications, WPT has replaced conventional approaches to overcome existential problems such as dependence upon mechanical contacts or plugs and exposure to mechanical wear and tear. Furthermore, coastal ferries operate in a harsh and saline environment that can post challenging for electrical safety. Reliable mechanisms for the quick and automatic disconnection of the charging system are also necessary to ensure safety if the ferry urgently needs to leave the dock.

To avoid this hassle and other issues regarding the reliability of the charging system, wired charging setups are being replaced by wireless charging technology. Ferries are equipped with a series of batteries with high storage capacity. Ferries start receiving the wireless power to charge the onboard batteries as soon as they are docked, saving time while conventional connection setup is eliminated. However, safety is still a concern as a massive amount of AC power is transmitted from the transmitter toward the receiver in the presence of highly conductive fluid, water. In the last decade, many breakthroughs have been made in underwater WPT technology, such as model analysis, optimization design, impedance matching, etc. [1-3]. Several vital parts and control mechanisms, including power electronics converters, transformers, passive elements, plugs, interconnectors, and a charging energy management system, are used in the battery charging path from the shore to the onboard battery (EMS).

Several charging mechanisms have been introduced, including AC, DC, and wireless options. Additionally, the most recent commercial shore-to-ship charging interfaces have also been introduced [4]. However, all these methods have drawbacks and issues regarding performance efficiency, reliability, and damage control. To overcome problems mentioned above associated with conventional methods. Wartsila [5] is the world's first commercial ferry operating with batteries capable of high-power wireless charging, and the successful project represents an inevitable breakthrough in the evolution of plug-in electrically operated vessels. Using a wireless charger, power transfer can start instantly as soon as the ship is docked rather than waiting until the cables are connected; hence, 20% of the time is saved, which can be utilized for charging purposes. Moreover, they overcome the safety issues regarding the connections, and the maintenance needs are reduced since wear and tear to connection lines is eliminated.

In Norway, the government has promoted the accurate zero-emission operation of short-distance coastal transportation [5]. Thus, governmental development contracts have challenged the marine industry to develop technology for battery-based, double-ended ferries for short fjord crossings along state highways. As a result of successful technology demonstrations, many ferry routes in Norway are expected to be converted into fully battery-based or plug-in hybrid operations during the coming years. Industrial development enabling this transition toward zero-emission operations will likely find widespread applications worldwide. The significant advantage is 20 percent more utilization of the available charging time, improved operational safety, and increased system reliability.

In [6], the authors proposed an elaborate analysis of the underwater Wireless Power Transmission system (inductive power transfer) and figured out an effective method for tracking the maximum power efficiency. In [7], the authors designed a WPT system for Autonomous Underwater Vehicles (AUVs) and transmitted a charging power of 300W, attaining an efficiency of 75% to 91%. In [8], the researchers contributed to reducing the receiver size and maintaining a constant current by studying the inductor-capacitor-capacitor and parallel (LCC-P) compensated WPT system. A unique, three-phase WPT structure having acceptable eccentricity resistance was developed and analyzed in [9], transferred 1.0 kW with an efficiency of 92.41%. Nonetheless, the Inductive Power Transfer (IPT) technology has some restrictions on being directly applied in the water due to the large amount of eddy-current loss induced by the high-frequency magnetic fields [10].

This paper uses a novel and safe method to transmit the voltage in the marine environment to charge the electric vessels. The proposed model is designed and simulated in the COMSOL MULTIPHYSICS software, and transmitters and receiver coils are created and performed as a complete system. The model can be tested for real-time function by simulating different scenarios. It is tested for three significant cases to achieve the best possible efficiency. Then, a prototype is built, experiments are performed in real-time, and the experiments and simulation results are compared. The rest of the paper is organized as follows. In Section 2, related work is discussed. In Section 3, the overview of the proposed method is discussed. In Section 4, a performance analysis of the proposed system is conducted, and various simulations performed are discussed. In Section 5, experimental results are examined, and the paper ends with a conclusion and discussion of results, acknowledgment, and references in the last sections.

MATERIALS AND METHODS

Optimization frequency in the IPT system can be attained by analyzing and considering the Eddy Current Loss (ECL) in an underwater WPT system [10]. To reduce the ECL of the underwater WPT system, an A1 × 1 × 1 structure was proposed, which also improved AC-AC power transfer efficiency by nearly 10% compared to the conventional [11]. In [12, 13], researchers optimized the wireless power transmission coils and the operating frequency by analyzing the EMF around the underwater WPT system. Besides, using ferrite cores can enhance mutual inductance, and thus, ECL can be decreased. However, the IPT system usually requires a relatively complicated coupler structure [14], including coils, ferrites, and shielding, which is difficult to seal in the water environment. Therefore, it is challenging to apply IPT technology to charge underwater devices.

On the contrary, Capacitive Power Transfer (CPT) technology is a better technique to charge the devices in the underwater environment and on the water's surface [15-16]. All three main limitations of the IPT system could be countered by the CPT technique [17]. Instead of magnetic fields, high-frequency electric fields are used for power transmission, so eddy current loss (ECL) will be eliminated. The capacitive coupler only needs metal plates, which can be easily sealed and are immune to the high pressure in the underwater environment. The CPT underwater shore-to-ship charging systems can be categorized into three categories: (1) Conductive, (2) Wireless, and (3) battery swapping. The conductive connection to the charging station of the electric vehicle is made via charging plugs classified

as AC and DC types and robot arms. The AC connector type 1 category has only single-phase functionality, and this type of connector is mainly used in home-charging Electric Cars. A different kind of AC connector, also known as Mennekes, after the manufacturer of this design, supports both single-and three-phase connections and is mainly used in the EU. This type of charging falls into the slow or semi-fast category. Thus, the electrocution process through a cable management system is less reliable and safe but more complex. Battery swapping is another solution for the CPT underwater shore-to-ship battery charging system.

The entire process takes much less time than fast or ultra-fast charging methods. In the case of EC, the current situation is that it is challenging to introduce it because the capacity and shape of the battery and how to incorporate it into EC differ for each EC brand. It will only be possible and advantageous if the way batteries are attached to the EC is standardized and companies can follow standards based on it. On the other hand, in the case of Electric Ships (ESs), especially ferries, battery replacement is very convenient and profitable. The ferry's waiting duration is short. Hence, spare battery packs can be stored at either or both ends depending on whether the ferry route is short or long for the journey. Also, ferry operations are limited to one specific route, which is a plus for using this technology. This way, ferry and inland freighter operating hours and trips can be extended. However, with the battery swapping system, there are effectively more batteries for the same number of EVs and ESs, putting more strain on a limited pool of resources. Removable batteries also suffer from short operating distances due to their disposable nature. The wireless charging system is a reliable alternative to conductive and battery swapping in the CPT system. EV charging can be categorized into slow, semi-fast, fast, and ultra-fast types, but the main challenge is the charging time to charge the onboard battery, which typically takes minutes to hours. Several optimized approaches are being pursued to minimize charging time comparable to gasoline refueling times.

A better and more advanced approach, Floating Charging Stations (FCS), has also been introduced. Electric charging stations, a novel idea, along the marine routes. Due to its complete isolation from the traditional electric grid and its built-over, especially floating platforms, the offshore FCS should be self-sufficient with storage options [18]. However, direct access to the charging station may compromise the integrity of the floating platform structure that the charging station is built over in the event of massive vessels. Additionally, ships approaching the station may only

sometimes be able to veer from their voyage route to access the FCS directly if the charging stations are slightly distant from the sea route [20]. The super-capacitors push a lot of current to the load during early charging, making that process faster. As time passes, the batteries will support the charging at average speed.

Proposed system

As mentioned in Figure 1(a), the constant current (CC) method is pursued in conventional methods. A constant current is maintained throughout the charging process based on the State of Charge (SoC) with an onboard battery pack. The advantage of this technique is that the current supplied throughout the process is limited, and the charging current can be easily determined. The main drawback is that the battery pack may overcharge every time the SoC estimation algorithm fails, ultimately shortening battery life. Battery charging rate is defined by the C rate, which indicates the rate at which the battery is charged or discharged. Here, a 1 C charge is a battery charging in 1 hour. An increase in the C-rate, essential for ultra-fast charging, leads to increased heat generation, which ultimately impacts lifespan if adequate cooling is not guaranteed. Also, coupling capacitance drops significantly when the distance is increased. Moreover, in the conventional approach, when the ship is docked on the shore, it keeps moving up and down in the water, leading to a misalignment between the transmitter and receiver. Besides, high-frequency excitation voltage is transferred by the transmitter (Tx) to the receiver, which is merged into the water. There is a high risk of electrocution during the transfer of power. The conventional and proposed methods used for charging purposes are depicted in Figure 1(a) and (b).

This paper proposed an innovative approach to overcome all the problems regarding reliability, time, safety, and complex structures. The proposed research also provides a solution for charging the batteries during the journey without the hazard of electrocution. To overcome the problems related to the current conventional CPT shore-to-ship charging system, it is replaced with a wireless charging system, as illustrated in Figure 1(b). There are two transmitters in the proposed system: the shoreside mobile transmitter (SMT) and the ship-side mobile transmitter rotating in the vicinity of the receiver. These are an array of magnets that result in the induction of voltage in the receiver coil. Consequently, voltage is induced in the receiver coil, which is utilized to charge the onboard batteries. Since there is no high AC voltage transmitted by the transmitters, unlike traditional transmitters, there is no risk of high input voltage in the marine environment. The rotation of the transmitters, one on

top and one on the bottom, results in voltage induction in the coil, which is then further processed (stepped up or down) and used to charge the onboard batteries.

The system is insulated with insulation, blocking the hazard of electrocution on the vessels.
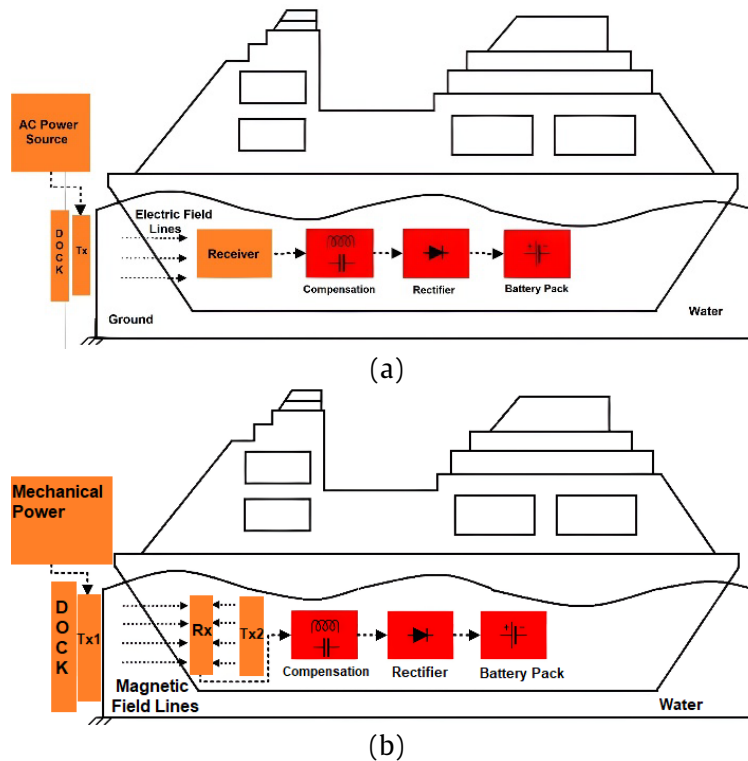

(a)

(b)

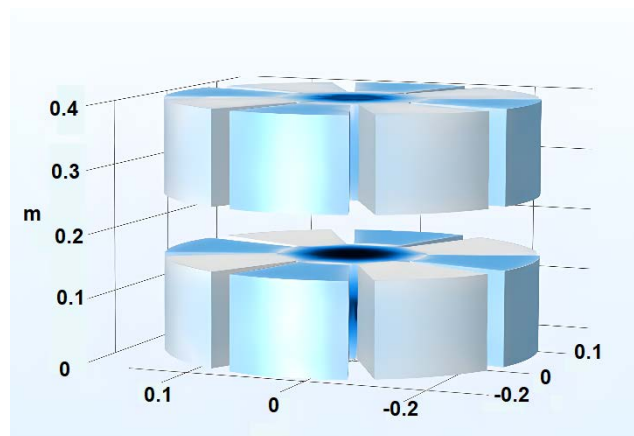**Figure 1** (a) Conventional charging system (b) Proposed system in marine environment.

Figure 2 Representation of segmented geometry of transmitters.

For the modeling of the proposed system and simulation in a finite element environment, the COMSOL® MULTIPHYSICS environment is chosen. The proposed model involves simulating the flux density distribution employing rotating transmitters. The overview of the proposed model is shown in Figure 2. The system is insulated with insulation, blocking the hazard of electrocution on the vessels. The simulation domain is the rotating domain that makes transmitters' magnets rotate. Consequently, the coil generates and receives the changing magnetic flux, and the voltage is induced inside the coil. For this purpose, built-in operation Rotatory Machines and magnetic physics are utilized.

The magnetic field of a magnetic dipole moment vector (m_1) can be written as [19].

$$\overrightarrow{B_{dip}}\left(\overrightarrow{V}\right) = \frac{\mu_\circ}{4\pi}\frac{1}{V^3}\left[3\left(\overrightarrow{m_1}.v\right)\overrightarrow{v} - \overrightarrow{m_1}\right] \qquad (1)$$

The magnitude of the field is directly proportional to the magnitude of its dipole moment, inversely proportional to the cube of distance (r), where ($\mu_\circ$) is the permeability of free space. The magnetic dipole moment is proportional to the volume of a magnet (V), and the residual magnetic file (B_r) of the magnet is expressed as:

$$\left|\overrightarrow{m_1}\right| = \frac{VB_r}{\mu_\circ} \qquad (2)$$

Due to the field (B_{dip}) created by each rotor, there is a torque described as the twisting effect that tends to align the dipole in the direction of that field, as shown.

$$\overrightarrow{T} = \overrightarrow{m_2} \times \overrightarrow{B_{dip}} \qquad (3)$$

where m_2 is the magnetic dipole moment vector of the magnet of the receiver side. The mechanical power transferred (P_m) is the product of the torque (T) and the angular frequency of rotation (ω) and is written as:

$$P = \omega T \qquad (4)$$

Equation (4) shows the power transferred between the transmitter and receiver through the air gap. Another essential factor to consider is that the magnetic insulation boundary must be set so that no flux is leaked. Another crucial factor to consider is that the magnetic insulation boundary must be fixed so that no flux is leaked. Modeling and analyzing are performed in three steps; firstly, the rotating transmitter with a central coil is modeled, and the results are interpreted. Secondly, one rotating transmitter is halted, and simulation is computed. Finally, rotating transmitters are moved away from the coil, and simulation is carried out for different distance proximities. The design of each component of the system is explained in detail below.

Figure 3 Overview of the Proposed Model.

Shore and ship-side mobile transmitters (array of magnets) design

A circular array of magnets is constructed using the physics of rotating machinery, magnetic (mm), to model the transmitters. Both landside and shipside transmitters are the same size and have the exact dimensions. Manufactured with permanent magnets called N50 (Sintered NdFeB), a rare-earth magnet, the dual rotary transmitter is designed for maximum torque-to-weight ratio. A circular array of eight magnets is created by constructing each magnet into a sector using the following sector angles: 45 degrees for each, making it 1/8th of the total geometry containing the magnets, coil, and soft iron in each sector. In the traditional approach, the distributed coils are only partially active as they overhang the magnets. The sector model approach avoids this because overhangs add weight, cost, resistance, and heat. This model has a fan-shaped arrangement of the transmitter magnets and coils, resulting in a fully active winding design with much less coil overhang. The design is, therefore, compact and small, and the reduced weight increases the magnetic flux area to generate more power. For each sector, a base geometry sketch is created using SOLIDWORKS. It is imported in COMSOL, and an intersection operation is performed to retain a magnet and rotor iron sector. This geometry is then rotated at an angle of -22.5 to reorient it in the domain and extruded to form a sector that contains the rotator iron core, as shown in Figure 2 and 3. The rotor is enclosed in air by extruding a fluid domain below. A fluid domain above is formed, which contains the coil and soft iron core, and then the rotor below is mirrored up to obtain the two rotating magnet sectors. Also, a soft iron core is extruded for the coil. This forms our complete rotating domain sector, along with two magnets enclosed in air and iron.

Each sector is combined to form an entire solution for the complete geometry, as shown in Figure 4. Ampere's law is applied to each industry of magnets where the magnetic strength is defined for the magnets as 1.4T. The geometric parameters of the proposed system are illustrated in Table 1. The relation between field variable magnetic field intensity and electric current density, magnetic flux density and area, and electric field and electric current density are shown in equations (5), (6), and (7).

$$\nabla \times H = J \qquad (5)$$

$$B = \nabla \times A \qquad (6)$$
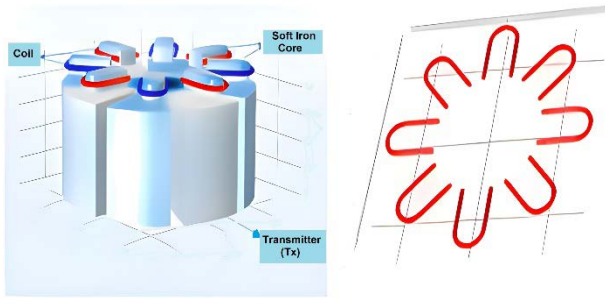
$$J = \sigma E \qquad (7)$$

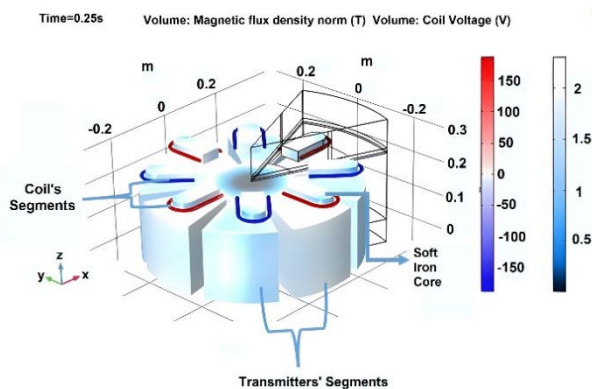**Figure 4** Representation of the entire receiver coil geometry.

Figure 5 Segmented geometry of Coil and a Transmitter.

Table 1 Geometric parameters of the simulated system in COMSOL.

Parameters	Values
Radius	1 m
Sector angle	45
Main construction plane	XK
Space dimensions	3
Number of domains	11
Number of boundaries	72
Number of edges	142
Number of Vertices	82
Transmitter 1 domain Thickness	0.165
Transmitter 2 domain Thickness	0.01

With the sector model approach, computing time is optimized not only for the shape of the magnets and their proximity and relative motion to the coil, which are optimized to get a better value of sinusoidal voltage. Before using the sector model approach, a crude design to start the problem consisted of 2 rotating disks surrounding a large circular single coil in between. The magnet size and alignment with the coil were not optimized; a soft iron core was needed to help the coil strengthen the magnetic field. After the simulations, the voltage was achieved at the end, but the curve was not smooth and had many voltage fluctuations. Many conditions were overlapping, leading to an incorrect solution, which is why the voltage induced initially resolved to zero over time, and convergence was moving towards singularity. Moreover, results were inconsistent as the Magnetic field was unevenly distributed in the domain due to a large circular copper disk, and the voltage curve was unevenly distributed over time and was staggering. Resultantly, the compute time is more than 12 min per single run, even with simplified Solver settings and low-resolution mesh. Hence, sectors were made for all the components with a sector angle of 45, making it 1/8th of the total geometry containing each sector's magnets, coil, and soft iron. The solution solved for each industry is combined in the result field to form an entire solution for the complete geometry, significantly decreasing the computing cost. With the new sector model, not only was compute time optimized, but in the new model, the shape of the magnets and their proximity and relative motion to the coil were optimized to get a suitable voltage sinusoidal profile and the most decisive factor in obtaining a significantly better voltage profile of magnets. The new computing time per several iterations and method of termination shown in Table 2 for the sector model was just over 2 minutes, even though the model domain, Entities involved, and conditions were complex compared to our previous model. The results of our new improvised model are given below.

Table 2 Method and termination.

Description	Value
Termination technique	Iterations or tolerance
Number of iterations	15
Tolerance factor	100
T	range (0,1/50,1)*1/60[rpm]/4
Timestamp	2.5E-4[s]

Receiver coil design

The receiver coil is also designed using the sector model approach to achieve concentrated voltage with low losses, less weight, and no coil overhangs. To design the receiver coil, a circular surface with a diameter of 5 mm is defined in the yz plane, and then a path is created along the x-y plane as a homogenized multi-turn conductor.

The single coil has a U-shape, and multiple turns with coil conductivity 6×10^7 [S/m] are selected by clicking on it and choosing from the settings box. The rest of the properties specified for the coil segments can be seen in Table 3 below. The circular coil is then swept across that path using the sweep feature of COMSOL. Like transmitter construction, a single coil section is modeled, and its alignment with the magnet size is optimized. A soft iron core around which the coil is wounded strengthens the magnetic field. The individual coils are designed on an xy plane with a z-coordinate of 0.197 and placed 45 degrees apart, as

shown in Figures 4 and 5. These coil sections between the transmitter sections are joined to form a complete geometry and make it work properly. Each coil section is placed between the transmitters so that the magnetic flux variation influences it.

Table 3 Parameter and Values of Coil.

Parameters	Values
Number of turns (N)	100
The diameter of the wire in the winding	0.001 m
Area (A)	$7.9e - 5\ m^2$
Coil wire conductivity	6×10^7 [S/m]
Coil current	30 [mA]
Coil length multiplication factor	17
Coil area multiplication factor	1

Equations for coils on top of moving magnets are as follows: (1) Ampere's law

$$B = \nabla \times A$$
$$\nabla \times H = J$$
$$J = \sigma E$$

1) Magnetic insulation 1

$$n.B = 0 \qquad (8)$$

2) Magnetic flux conservation: Air domain lowe

$$\nabla \cdot B = 0$$
$$B = \mu_\circ r H \qquad (9)$$
$$H = -\nabla V_m$$

3) Magnetic flux conservation: Rotor iron

$$H = -\nabla Vm \qquad (10)$$

4) Periodic condition for coils

Vector potential formulation (Ampere's law)

$$Asrc = -Adst \qquad (11)$$

Scalar potential formulation (Magnetic flux conservation)

$$Vm.src = -Vm.dst \qquad (12)$$

Performance analysis

The finite Element Method is adopted for geometry with more than one dimension because the results are then a grid of a basis function. In the proposed system, the physics-controlled mesh is applied for the overall model, while a separate "Moving Mesh" is defined for the rotating parts of the system, i.e., Transmitters. The accuracy of the solution in FEM depends on the density of the mesh, which is interrelated to the computational cost. An accurate solution may

result in a very high computation cost. The software allows the user to pick the order of element discretization for each dependent variable. However, the degree of freedom increases with the increment in element discretization. Consequently, the computational time is increased, and it takes longer to solve, especially for time-dependent problems. In the proposed system, since the transmitters and receiver have some structured geometry, the structured mesh is preferred, as shown in Figure 6. Additionally, the physics of the model is known; therefore, its physics-controlled meshing option is selected. The Sectional geometry of a single coil loop can be seen in Figure 7.
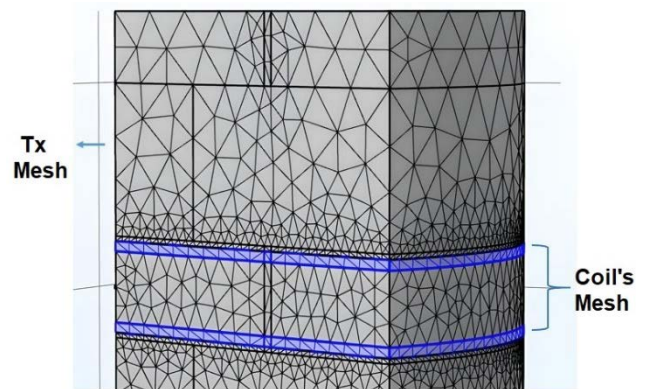

Figure 6 Complete Mesh Structure of a Coil and a Transmitter's Segment.
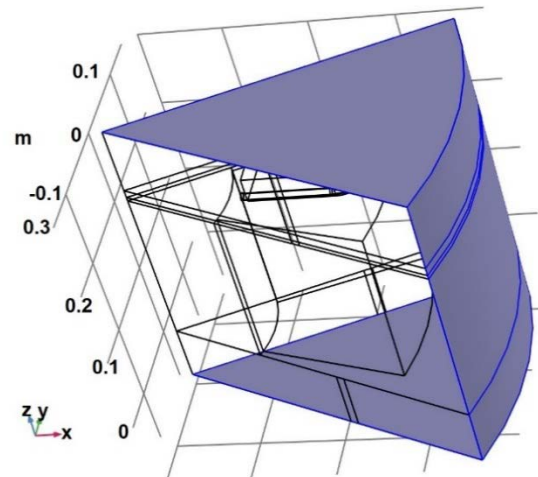

Figure 7 Representation of coil sectional geometry.

After completing mesh analysis, various simulations are carried out to evaluate the model's performance and determine the value of voltage induction and transmitted power in the receiver coil under multiple circumstances. All the cases are explained in detail below.

Case 1: Simulation with both transmitters rotating

To analyze the work performance of the model, three different simulations were carried out with other parts of the model in operation. In the first case,

both transmitters are kept 5 cm from the receiver coil and rotated with an rpm of 100. The number of turns of the receiver coil is considered 100 throughout the simulation. Each coil sector is aligned with the sectors of the magnets (as shown in Figure 8a) so that the maximum flux passes through the air domain with the rotation of both transmitters. In this case, the wire resistance is not ignored, and even though the rpm value still needs to be high, it gives promising results. The magnetic flux lines generated by the rotation of transmitters are highlighted and shown in Figure 9.

As shown in Figure 10, the total voltage induced in the receiver coil is around 270 V. As expected, the flux density is higher when both transmitters rotate simultaneously near the receiver coil wire, thus causing more voltage.

Case 2: Simulation with one transmitter rotating

In this case, the top transmitter is fixed, and only the lower transmitter rotates. The rpm of the rotating transmitter, its distance from the coil, and the number of coil turns are about their previous values. The magnetic flux density is now weak, as depicted by flux lines in Figure 11, and the induced voltage is reduced to half of the original with both transmitters rotating, as shown in Figure 12.

However, as there is a direct relation between the induced current and rpm, increasing the rpm will increase the induced current; similarly, increasing the number of turns in the winding can improve the voltage value.
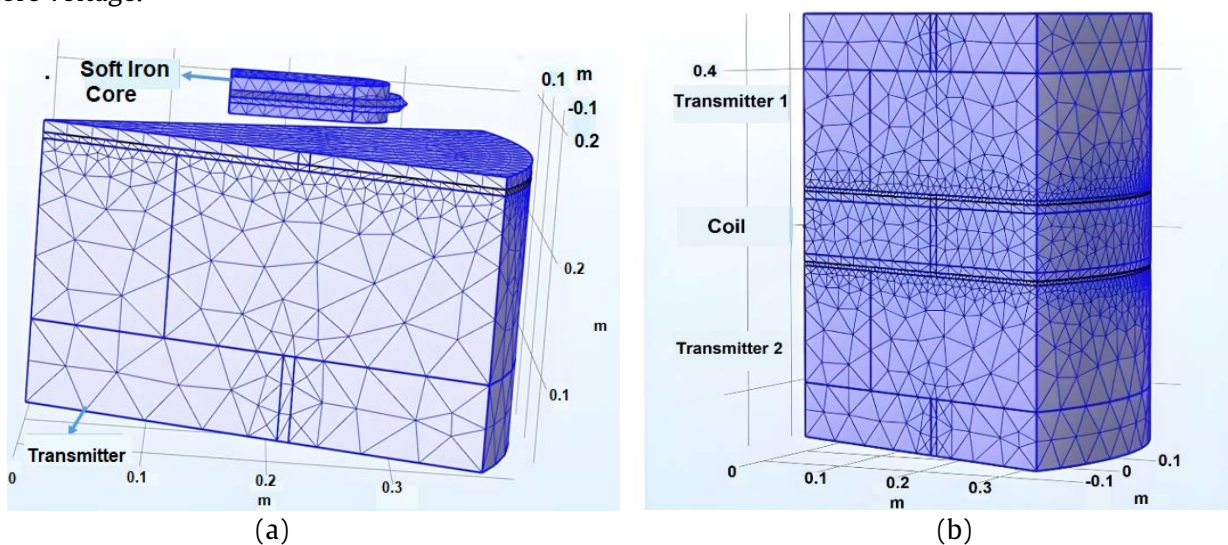

Figure 8 (a) shows the shore-SMT and Receiver Coil Winding, and (b) shows the Receiver coil between the Shore and ship-SMTs.
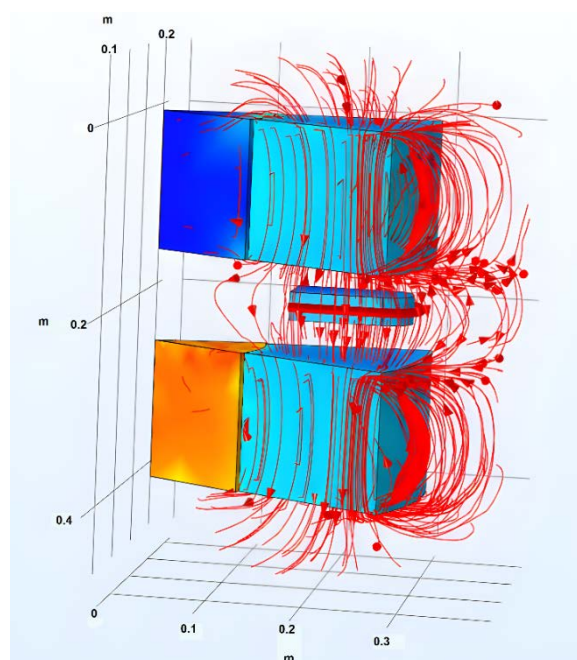

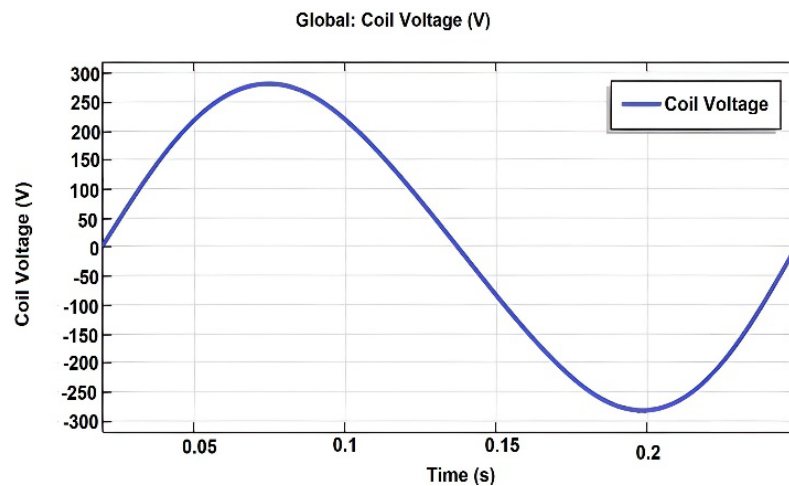**Figure 9** Magnetic flux lines and field generated by the rotation of both transmitters.

Global: Coil Voltage (V)

Figure 10 Voltage induced in the receiver coil (Case 1).
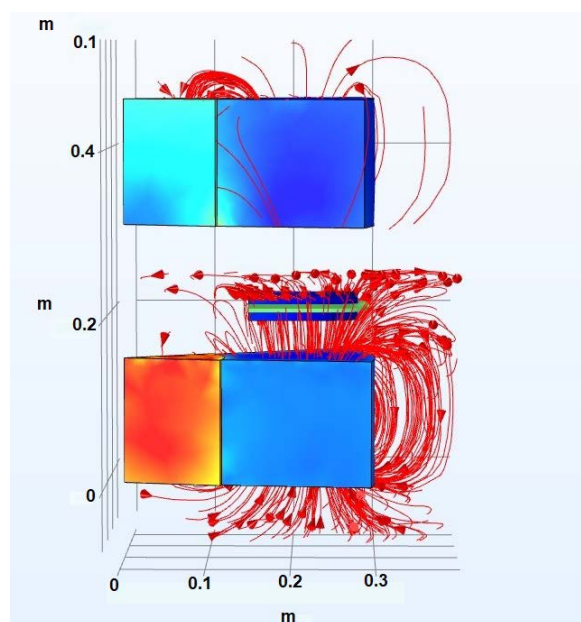
Figure 11 The rotation of a single transmitter generates magnetic flux lines and fields.
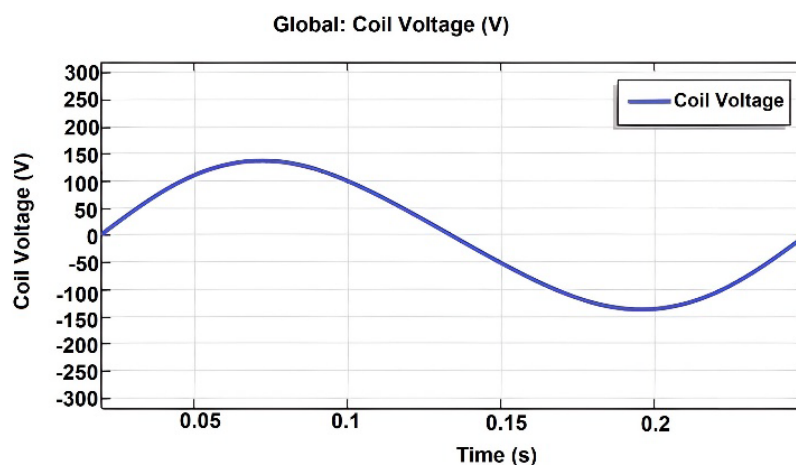
Global: Coil Voltage (V)

Figure 12 Voltage induced in the receiver coil (Case 2).

Case 3: Simulation with changing transmitter position

In this case, the position of the rotating transmitters varies from 5 cm to 7 cm, as shown in Table 5. Since the value of induced voltage is proportional to the magnetic flux passing through the receiver coil from the rotating transmitters. The higher the flux value, the more voltage is generated in the coil. The relative distance of transmitters from the receiver coil

is essential in determining the value of induced voltage. From Table 4, the induced voltage in the coil decreases when the distance between the transmitter and receiver coil is increased. However, the voltage value is improved if the transmitters are moved away but rotated simultaneously.

The maximum voltage of 140 V is obtained at the transmitter's distance of 5 cm from the coil when one transmitter is kept static, and the other is rotated. Similarly, as the rotating transmitter is moved further apart at distances of 6, 6.25, 6.5, and 7 cm, the induced voltage decreases to 108.99, 103.33, 98, and 89 volts, respectively.
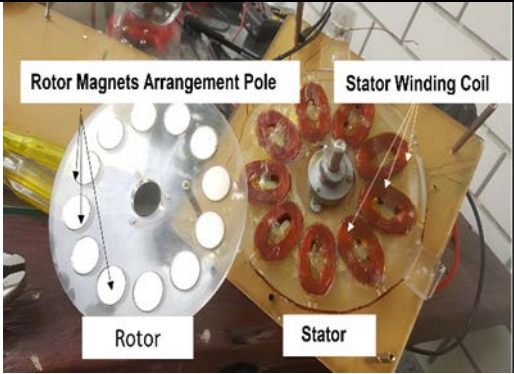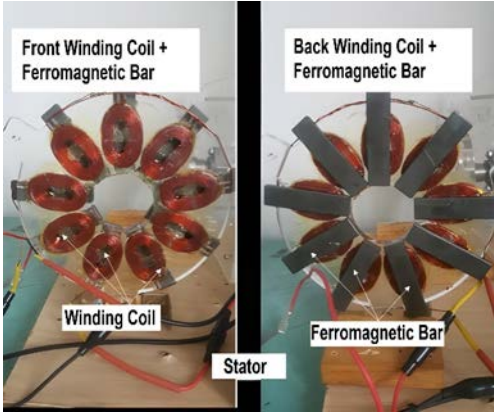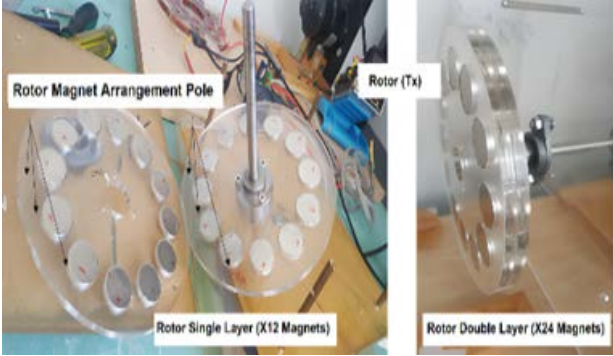
In the other case, when both transmitters are rotated, the maximum voltage of 280 V is induced with 5 cm between the coil and transmitters. Increasing the distance to 6, 6.25, 6.5, and 7 cm reduces the voltage

to 227.9, 208.34, 198.07, and 179.83 V, respectively. The distance of both transmitters affects the voltage value; however, if both are rotated simultaneously, the voltage rises.

Table 4 Table of simulation with changing transmitter position.

Transmitter 1	Transmitter 2	Distance of T1 from coil (cm)	Distance of T2 from the coil
Static	Rotating	5	5
Static	Rotating	5	6
Static	Rotating	5	6.25
Static	Rotating	5	6.5
Static	Rotating	5	7
Rotating	Rotating	5	5
Rotating	Rotating	6	6
Rotating	Rotating	6.25	6.25
Rotating	Rotating	6.5	6.5

Table 5 Experimental Setup.

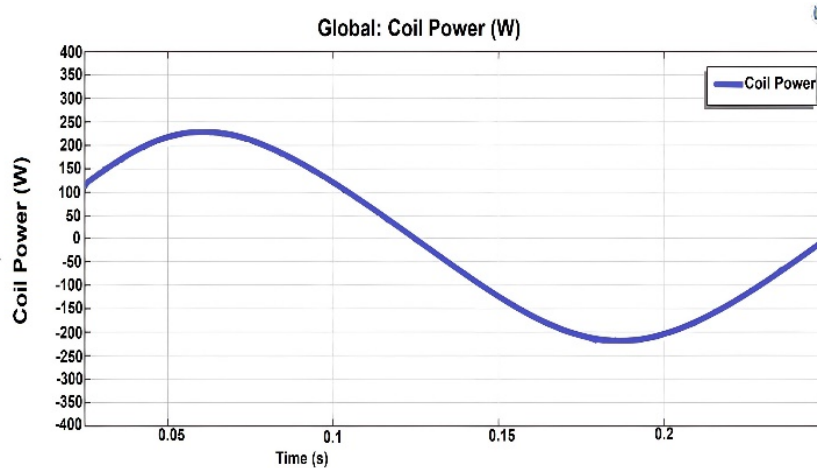| Module	Illustration	Description
Rotor and Stator		Rotor: Single layer (x12 magnets) Stator: Single layer (x9 winding coils)
Stator		Stator: x9 winding coils + x9 Ferro-bars
Rotor		Rotor: single layer (x12 magnets) double layer (x24 magnets)

Figure 13 Power generated in the coil.

Transmitted power

The instantaneous power values can be accessed by the environment variable Coil, which is the coil power. Mathematically, simple power is obtained by taking the product of the instantaneous voltage of the coil and the instantaneous current through the coil. As the voltage is produced as a function of time during the rotation of the transmitter, the instantaneous voltage and resulting current are utilized to calculate the power, as shown in equation (13) below. The power when both transmitters are rotating at an rpm of 100, at 5 cm from the receiver coil, is described in Figure 13.

$$P(coil) = V_{inst} \times I_{inst} \qquad (13)$$

RESULTS AND DISCUSSION

Experimental set-up

An axial flux permanent magnet topology, as shown in Figure 14 (a) single-side, (b) double-side, is used in the experimental setup. The magnets are designed and arranged so that the magnetic field of the individual magnets adds up to give the total field. Similarly, the coils are designed in such a way that maximum power is transferred, and magnetic flux leakage is reduced. Various simulations are carried out, and the amount of magnetic flux passing through the receiver coil for each simulation varies, resulting in different values of induced voltage. The experimental setup of hardware used for conducting the experiments according to simulation is shown in tabular form in Table 5. Many possible patterns exist between single-side and double-side topologies with the Tx rotor and the Rx stator. Still, this research studies the TX surface-mounted permanent magnet rotor patterns with the Rx surface-mounted winding coil stator. The single-side topology consists of one rotor and one stator. Two rotors and one stator or vice versa illustrate the double-side topology.
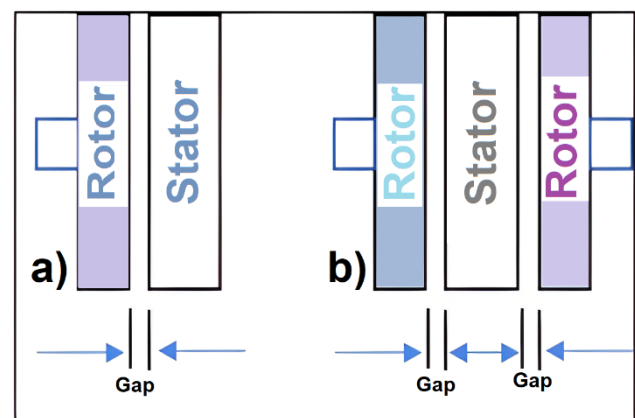

Figure 14 a) Single-side permanent magnet topology. b) Double-sided Axial flux permanent magnet topology.
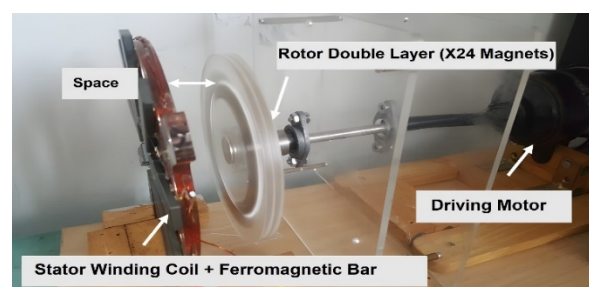

Figure 15 Rotating magnetic transmitter and static coil experimental setup.

Experimental results

This section presents the experimental analysis of the proposed, designed prototypes. Three prototypes of the proposed design have been developed using various coil sets with multiple turns in the stator plate and varying numbers of magnets in the rotor plates with different spacings. The prototypes are tested for multiple cases, and the resulting voltage, power, and current variations generated with the varying rpm are noted. The experimental setup is shown in Figure 15,

which includes a driving motor and an oscilloscope with a 2-channel probe for AC power measurement. The magnetic rotors (transmitters) were driven with the help of a driving motor so that both layers were rotated together on the same side in proximity to the static winding coil. The driving motor rated at 75 W and operating at 700 rpm was designed using the same procedures, while the study patterns with Tx sur-face-mounted permanent magnet rotor and Rx surface-mounted winding coil stator are in Table 6.

Table 6 Measurement results of Tx and Rx topology.

Topology	Rotor Module	Stator Module	Gap (cm)	System efficiency (%)
Single side	Single layer (x12 magnets)	Single layer (x9 winding coils)	0.5 cm.	50%
			1 cm.	40%
			1.5 cm.	30%
			2 cm.	10%
		Single layer with Ferro bar (x9 windingcoils + x9 Ferro-bars)	0.5 cm.	55%
			1 cm.	45%
			1.5 cm.	35%
			2 cm.	15%
	Double layer (x24 magnet)	Single layer (x9 winding coils)	0.5 cm.	70%
			1 cm.	65%
			1.5 cm.	60%
			2 cm.	55%
		Single layer with Ferro bar (x9 windingcoils + x9 Ferro-bars)	0.5 cm.	75%
			1 cm.	70%
			1.5 cm.	65%
			2 cm.	60%
Double side	Single layer (x12 magnets)	Single layer (x9 windingcoils)	0.5 cm.	80%
			1 cm.	76%
			1.5 cm.	65%
			2 cm.	55%

System efficiency

The system efficiency was measured and resulted in Table 6, which was the efficiency of the receiver in electrical power. The generator, coupled to the DC motor, was tested at a speed of 700 rpm. The input power is the electrical power supplied to the motor driver. The output power is a difference in the air gaps, the ratio of output power against input power by voltage and current.

Discussion

This article presents an innovative wireless power transmission system for marine applications. The system ensures safe power transmission from the transmitter to the receiver for charging purposes. The simulation results coincide with the experimental results. The proposed system differs from Conventional WPT systems because AC voltage is not required to be fed into the transmitter. The system can induce a voltage in the receiver coil by rotating transmitters of a circular array of magnets.

CONCLUSION

However, there is a difference in efficiencies obtained through simulation and experiments, as distance in real-time should be less to achieve better results than in a simulation environment. In the simulated environment, the air gap between the transmitters and receiver windings is selected in the 5-7 cm range, while in experiments, it varies from 0.5-2 cm. During simulation, the model was tested for three case scenarios: rotating only a single transmitter first, then rotating both transmitters simultaneously, and lastly varying the distance of each transmitter from the windings to determine the highest efficiency level. The highest voltage of 280 V was induced when both transmitters rotated, having an air gap of 5 cm from the receiver coil windings. Moreover, all the high

voltage ratings are achieved when both transmitters rotate regardless of the air gap. The induced voltage ratings in the receiver coil, while one of the transmitters is static, were comparatively low, with 89 V being the lowest. The experiments were then performed to test the results of the simulations. All three cases were repeated, and the highest possible efficiency (80%) was achieved in experiments when both transmitters moved. The proposed system is modeled and simulated in COMSOL and then tested by designing a prototype that shows promising results.

REFERENCES

1. Vincent D, Sang PH, Williamson SS. Feasibility study of hybrid inductive and capacitive wireless power transfer for future transportation. 2017 IEEE Transportation Electrification Conference and Expo (ITEC), 2017 Jun 22-24; Chicago, IL, USA: IEEE; 2017.

2. Guo Y, Wang L, Zhang Y, Li S, Liao C. Rectifier load analysis for electric vehicle wireless charging system. IEEE Transactions on Industrial Electronics. 2018;65(9):6970-82.

3. Lu M. Synergetic Attenuation of Stray Magnetic Field in Inductive Power Transfer [dissertation]. Virginia: Virginia Polytechnic Institute; 2017.

4. Karimi S, Zadeh M, Suul JA. Shore charging for plug-in battery-powered ships: Power system architecture, infrastructure, and control. IEEE Electrification Magazine. 2020;8(3):47-61.

5. Wärtsilä's wireless charging: ahead of the game [Internet]. New York: 2017 - [updated 2017 Dec 4; cited 2020 Jun 9]. Available From: https://www.shiptechnology.com/features/wartsilas-wireless-charging-ahead-game/

6. Le K, Yuli HU, Wei Z. Maximum power efficiency tracking on underwater magnetic resonant wireless power transfer system. Journal of Harbin Engineering University. 2017;38:829-35.

7. Lin M, Li D, Yang C. Design of an ICPT system for battery charging applied to underwater docking systems. Ocean Engineering. 2017;145:373-81.

8. Yan Z, Zhang Y, Song B, Zhang K, Kan T, Mi C. An LCC-P compensated wireless power transfer system with a constant current output and reduced receiver size. Energies. 2019;12(1):172.

9. Kan T, Mai R, Mercier PP, Mi CC. Design and analysis of a three-phase wireless charging system for lightweight autonomous underwater vehicles. IEEE Transactions on Power Electronics. 2018;33(8):6622-32.

10. Yan Z, Zhang Y, Kan T, Lu F, Zhang K, Song B, et al. Frequency optimization of a loosely coupled underwater wireless power transfer system considering eddy current loss. IEEE Transactions on Industrial Electronics. 2019;66(5):3468-76.

11. Zhang K, Zhang X, Zhu Z, Yan Z, Member S, Song B, et al. A new coil structure to reduce eddy current loss of WPT systems for underwater vehicles. IEEE Transactions on Vehicular Technology. 2019; 68:245-53.

12. Lee IG, Kim N, Cho IK, Hong IP. Design of a patterned soft magnetic structure to reduce magnetic flux leakage of magnetic induction wireless power transfer systems. IEEE Transactions on Electromagnetic Compatibility. 2017;59:1856-63.

13. Yan Z, Song B, Zhang K, Wen H, Mao Z, Hu Y. Eddy current loss analysis of underwater wireless power transfer systems with misalignments. AIP Advances. 2018;8:101421.

14. Kan T, Zhang Y, Yan Z, Mercier PP, Mi CC. A rotation-resilient wireless charging system for lightweight autonomous underwater vehicles. IEEE Transactions on Vehicular Technology. 2018; 67(8):6935-42.

15. Tamura M, Naka Y, Murai K, Nakata T. Design of a capacitive wireless power transfer system for operation in fresh water. IEEE Transactions on Microwave Theory and Techniques. 2018;66(12): 5873-84.

16. Tamura M, Naka Y, Murai K. The design of a capacitive coupler for wireless power transfer under fresh water focuses on the kQ product. 2018 IEEE/MTT-S International Microwave Symposium-IMS; 2018 Jun 10-15; Philadelphia, PA, USA: IEEE; 2018.

17. Urano M, Takahashi A. Study on underwater wireless power transfer via electric coupling. 2016 IEEE International Meeting for Future of Electron Devices, Kansai (IMFEDK); 2016 Jun 23-24; Kyoto, Japan: IEEE; 2016.

18. Sruthy V, Raj B, Preetha PK, Ilango K. SPV based Floating Charging Station with Hybrid Energy Storage. 2019 IEEE International Conference on Intelligent Techniques in Control, Optimization and Signal Processing (INCOS); 2019 Apr 11-13; Tamilnadu, India: IEEE; 2020.

19. Griffiths DJ. Introduction to electrodynamics. 3rd Ed. Upper Saddle River NJ: Prentice-Hall; 1999.

20. Sruthy V, Raj B, Preetha PK. An offshore floating charging station for electric ships: accessibility enhancement schemes for recharging. Ships and Offshore Structures. 2020;16(10):1143-50.